UNIVERSITY OF Southampton

University of Southampton Research Repository
ePrints Soton

Copyright © and Moral Rights for this thesis are retained by the author and/or other copyright owners. A copy can be downloaded for personal non-commercial research or study, without prior permission or charge. This thesis cannot be reproduced or quoted extensively from without first obtaining permission in writing from the copyright holder/s. The content must not be changed in any way or sold commercially in any format or medium without the formal permission of the copyright holders.

When referring to this work, full bibliographic details including the author, title, awarding institution and date of the thesis must be given e.g.

AUTHOR (year of submission) "Full thesis title", University of Southampton, name of the University School or Department, PhD Thesis, pagination

http://eprints.soton.ac.uk

UNIVERSITY OF SOUTHAMPTON

FACULTY OF PHYSICAL SCIENCES AND ENGINEERING

Electronics and Computer Science

IRRADIATION-BASED DEFECT ENGINEERING OF GRAPHENE DEVICES

By

Shuojin Hang

Thesis for the degree of Doctor of Philosophy

October 2015

UNIVERSITY OF SOUTHAMPTON

ABSTRACT

FACULTY OF PHYSICAL SCIENCES AND ENGINEERING

Electronics and Computer Science

Doctor of Philosophy

IRRADIATION-BASED DEFECT ENGINEERING OF GRAPHENE DEVICES

Shuojin Hang

The addition of structural defects modifies the intrinsic properties of graphene – the two-dimensional allotrope of carbon. The controlled introduction of such defects is therefore desired to realise specific functions. For instance, the grain boundaries formed between epitaxial grown graphene domains has been observed to mimic a metallic wire. By contrast, the presence of point defects in a graphene channel affects the carrier transport significantly in a manner such as the Fermi-level pinning, transport-gap widening and Anderson localization. Incorporating these defects into conventional device structures can open up a new horizon for device engineering.

In this work, I propose and explore the defect engineering of graphene devices via ion bombardment using a helium ion microscope (HIM). The lithographic advantage of HIM is demonstrated for various graphene nanostructures such as fully gated 20nm double quantum dots and 10nm nanoribbons, upon which a hybrid EBL-HIM fabrication technique is developed for device integration. Graphene irradiated with HIM up to 5×10^{14} cm^{-2} shows a transition from Stage 1 to Stage 2 disorder as probed by confocal Raman spectroscopy. For the first time, the damage of ion-beam-milling on a graphene-on-substrate sample is visualised. The spatially resolved Raman map shows that the beam damage can extend to a few hundred nm around the 30nm cut, which is attributed to the damage due to backscattered helium ions and recoils from the substrate.

Furthermore, the electrical properties of irradiated graphene nanoribbons (iGNR) is characterised. As irradiation dose increases, the iGNR devices shows an abrupt decrease in mobility and interestingly an asymmetric decrease of conductance in the

electron and hole conduction branches. This is then related to the pinning of Fermi level in iGNR, a unique property caused by irradiation. This is believed to be associated with additional dangling bonds (scattering centres) created by irradiation, as supported by XPS analysis. Based on these properties, a new graphene device structure is explored, in which irradiated regions are used as energy barriers. The temperature-dependent conductance shows the signature of thermal-activated variable range hopping (VRH) at intermediate temperature. The localisation lengths extracted from hopping temperature showed good agreement with that from length-dependent conductance. Furthermore, the activationless VRH is observed for relatively high electric field.

CONTENTS

DECLARATION OF AUTHORSHIP

I, Shuojin Hang, declare that this thesis entitled “Irradiation-based defect engineering of graphene devices” and the work presented in it are my own, and have been generated by me as the result of my own original research. I confirm that:

1. This work was done wholly or mainly while in candidature for a research degree at this University;

2. Where any part of this thesis has previously been submitted for a degree or any other qualification at this University or any other institution, this has been clearly stated;

3. Where I have consulted the published work of others, this is always clearly attributed;

4. Where I have quoted from the work of others, the source is always given. With the exception of such quotations, this thesis is entirely my own work;

5. I have acknowledged all main sources of help;

6. Where the thesis is based on work done by myself jointly with others, I have made clear exactly what was done by others and what I have contributed myself;

7. Parts of this work have been published as indicated in the “List of Publications” section provided with this manuscript.

Signed: _____

Date: _____

LIST OF PUBLICATIONS

Journals:

1. **S. Hang**, Z. Moktadir, and H. Mizuta, Raman study of damage extent in graphene nanostructures carved by high energy helium ion beam, **Carbon**, vol. 72, pp. 233–241, Feb, 2014;

2. Z. Moktadir, **S. Hang**, and H. Mizuta, Defect-induced Fermi level pinning and suppression of ambipolar behaviour in graphene, **Carbon**, vol. 93, pp. 325-334, Nov, 2015;

3. H. Mizuta, Z. Moktadir, S. a. Boden, N. Kalhor, **S. Hang**, M. E. Schmidt, N. T. Cuong, D. H. Chi, N. Otsuka, M. Muruganathan, Y. Tsuchiya, H. Chong, H. N. Rutt, and D. M. Bagnall, Fabrication and ab initio study of downscaled graphene nanoelectronic devices, **Proc. SPIE**, vol. 8462, p. 846206, Sep. 2012;

4. I. J. Umoh, Z. Moktadir, **S. Hang**, T. J. Kazmierski and H. Mizuta, A circuit model for defective bilayer graphene transistors, 2015, submitted;

Conferences/workshops:

1. **S. Hang**, Z. Moktadir, and H. Mizuta, Irradiation induced tunnel barrier in graphene, 8th International Conference on the Fundamental Science of Graphene and Applications of Graphene-Based Devices (Graphene Week), Gothenburg, Sweden, June, 2014;

2. **S. Hang**, Z. Moktadir, and H. Mizuta, Irradiation induced tunnel barrier in side-gated graphene nanoribbon, 2014 IEEE Silicon Nanoelectronics Workshop, Honolulu, USA, June, 2014

3. **S. Hang**, Z. Moktadir, and H. Mizuta, Ultra-fine graphene nanoelectronic devices carved with tightly focused helium ion beam, 7th International Conference on the Fundamental Science of Graphene and Applications of Graphene-Based Devices (Graphene Week), Chemnitz, Germany, 02 - 07 June 2013.

4. **S. Hang**, Z. Moktadir, Shinichi Saito and H. Mizuta, Direct helium ion milling technology: towards the fabrication of extremely down-scaled graphene nanodevices, 2013 IEEE Silicon Nanoelectronics Workshop, Kyoto, Japan, June, 2013 (Oral);

5. Z. Moktadir, **S. Hang**, and H. Mizuta, Unipolar conduction induced by defects in graphene nanowire transistors, 2014 IEEE Silicon Nanoelectronics Workshop, Honolulu, USA, June, 2014

6. Z. Moktadir, **S. Hang**, J. Reynolds, K. Higashimine, and H. Mizuta, Metal-Insulating transition in disordered graphene nanoribbons controlled by helium ion irradiation, 45th International Conference on Solid State Devices and Materials (SSDM), Fukuka, Japan, September, 2013

7. N. Kalhor, **S. Hang**, T. Iwasaki, Z. Moktadir, S. Boden, M. Manoharan and H. Mizuta，Sharp edged sub-20 nm graphene single-electron devices by helium ion beam milling technique，2013 JSAP-MRS Joint Symposia, Symposium C: Advanced Nano Carbon Devices and Materials，Kyoto，September 2013

8. Z. Moktadir, **S. Hang**, Shinichi Saito and H. Mizuta, Role of the edge states and the point defects on electronic transport in bilayer graphene field effect transistors, 5th International Conference on Recent Progress in Graphene Research，Tokyo，Japan, September 2013

9. H. Mizuta, **S. Hang**, N. Kalhor, S. A. Boden and Manoharan M., Z. Moktadir, 'He$^+$ ion beam based nanofabrication and characterization of downscaled graphene nanodevices (Invited Talk)', II Bilateral Italy-Japan Seminar Silicon nanoelectronics for advanced application, Lago Garda, 29-30 April 2013

10. Z. Motadir, **S. Hang**, S. Saito and H. Mizuta, 'Role of the edge states and the point defects on electronic transport in bilayer graphene field effect transistors', 2013 JSAP-MRS Joint Symposia, Symposium C: Advanced Nano Carbon Devices and Materials, Kyoto, 16 – 20 September 2013.

11. N. Kalhor, S. A. Boden, **S. Hang**, Z. Moktadir and H. Mizuta，Fabrication of Graphene Double Quantum Dot Devices by He-ion Beam Milling, ImagineNano Graphene 2013，Bilbao, Spain, April 2013

12. H. Mizuta, Z. Motadir, **S. Hang**, N. Kalhor, J. Reynolds, K. Higashimine, M. Manoharan.，Study of carrier transport for graphene nanoribbons with helium ion induced point defects and edge irregularities，15th International Symposium on "Ultrafast Phenomena in Semiconductors" (15-UFPS)，Vilnius，August 2013

13. H. Mizuta, Z. Motadir, **S. Hang**, N. Kalhor, J. Reynolds, T. Iwasaki, M. Schmidt and Manoharan M., 'Helium ion beam based novel fabrication of downscaled graphene nanodevices (Invited Talk)', The 15th Takayanagi Kenjiro Memorial Symposium – Towards Advanced Imaging Science Creation , Hamamatsu, 12 – 13 November 2013.

14. H. Mizuta, Z. Moktadir, Boden, S. A., N. Kalhor, **Hang. S**, M. E. Schmidt, C. T. Nguyen, C. H. Dam, N. Otsuka, M. Manoharan, Y. Tsuchiya, H. Chong, H. N. Rutt, D. M. Bagnall, Downscaled graphene nanodevices: Fabrication and ab initio study, 2012 IEEE 11th International Conference on Solid-State and Integrated Circuit Technology (ICSICT), November, 2012;

15. H. Mizuta, Z. Moktadir, S. A. Boden, **S. Hang**, N. Kalhor, K. Kitagawa and M. Manoharan.，Electronic states and transport in graphene nanostructures with point defects，EMN West Meeting: Energy Materials Nanotechnology，Houston，January, 2013

16. H. Mizuta, T. Iwasaki, N. Kalhor, **S. Hang**, Z. Moktadir, J. Sun and M. Muruganathan, 'Fabrication and characterization of downscaled graphene nanoelectronic devices and NEMS (Invited Talk)', The 1st Malaysia-Japan Joint Symposium on Nanotechnology, Kuala Lumpur, 10 December 2014.

Seminar:

1. **S. Hang**, Z. Moktadir, and H. Mizuta, Graphene quantum dots and spin qubits, JAIST International Seminar on Emerging Nanotechnologies for ‘ More-than-Moore’ and ‘Beyond CMOS’ era, Kanazawa, March, 2012

2. **S. Hang**, Z. Moktadir, and H. Mizuta, Irradiation induced tunnel barrier in side-gated graphene nanoribbons, Nano Group Event 2014, Southampton, UK, July, 2014

3. **S. Hang**, Z. Moktadir, J. Reynolds and H. Mizuta, Electrical properties of graphene devices modified by helium ion irradiation, Helium/Neon Ion Microscopy Workshop, Dublin, Ireland, July 2015

Acknowledgements

There is a long but incomplete list of names that I would like to acknowledge my gratitude to.

Above all, I would like to thank my wife, Mrs Xing Huang for her great patience, understanding and invaluable support all through these years. I would then like to express my thanks to my parents for everything.

I want to thank the primary supervisor of this project, Prof. Hiroshi Mizuta for giving me this unique opportunity to pursue with my curiosity in nanotechnology. This work would not have been possible without his guidance and support. I see in him a successful researcher, a wise mentor and a lifelong friend. I would also like to thank my second supervisor Dr Zakaria Moktadir for sharing with me his brilliant ideas and being always available for an inspiring chat.

I would like to thank the colleagues at the Southampton University Nano Research Group for their unparalleled support during my PhD. I express my sincere gratitude to Dr Harold Chong, Prof Shinichi Saito, Dr Yoshishige Tsuchia, Mr Jingxing Shi, Dr Nima Kalhor, Dr Stuart Boden, Mr Peter Ayliffe, Mr Paul Clark, Dr Yunpeng Lin, Dr Yudong Wang and all technicians at SNC who have shared me with their technical expertise. I thank Mrs Glenys C Howe, Mr Sheng Ye, Dr. Liam Boodhoo, Dr Feras Alkhalil, Dr Kian S Kiang, Dr Kai Sun, Dr Ruiqi Chen and Mr Jamie Reynolds for their assistance in the office and labs. Special thanks to Dr Katrina Morgan, Ms Nur Zatil Hashim and Ms Maria-Eleni Rizou for bringing very lovely plants to the bay.

I thank the researchers at Mizuta Lab in JAIST for their very warm reception during my visit in the 2014 winter: Dr Manoharan Muruganathan, Dr Jian Sun, Dr Marek E. Schmidt, Mr Wenzhen Wang, Mrs Reiko Seki, Dr Le The Anh, Mr Takuya Iwasaki, Mr Nozomu Kanetake, Mr Keisuke Inoue and many more.

In addition, I thank all the players of the Southampton Common United Football Club for hosting regular games all year around which is an important part of my life during the past three years: Mr Chun Zhao, Dr Jin Yao, Mr Graham Wood, Mr Wei Wang and many more.

LIST OF ACRONYMS

0D/1D/2D/3D/4D	Zero/one/two/three/four dimensional
AFM	Atomic force microscopy
BI	Backscattered ions
BIV	Best image voltage
BLG	Bilayer graphene
ci	Charged impurity
CNP	Charge neutrality point
CVD	Chemical vapour deposition
DFT	Density function theory
DNA	Deoxyribonucleic acid
DQD	Double quantum dot
DV	Double vacancy
EBL	Electron beam lithography
ES-VRH	Efros and Shklovskii variable range hopping
FIB	Focus ion beam
FIM	Field ion microscope
FOV	Field of view
FWHM	Full width at half maximum
GFIS	Gas field ionization source
GNR	graphene nanoribbon
hBN	Hexagonal boron nitride
HIM	Helium ion microscope
HOPG	Highly oriented pyrolytic graphite
HRTEM	High resolution transmission microscope
iGNR	irradiated graphene nanoribbon
IPA	Isopropyl alcohol
ITO	Indium tin oxide
JAIST	Japan Advanced Institute of Science and Technology
LDOS	Local density of states
LOR	Lift-off resist
MCP	Microchannel plate
mg	Midgap states
MIBK	Methyl isobutyl ketone
MIT	Metal-Insulator-transition
MLG	Multilayer graphene
MMA	Methyl methacrylate
NMP	N-Methyl-2-pyrrolidone
PG	Plunger gate
PKA	Primary knock-on atoms
PMMA	Poly(methyl methacrylate)
PVD	Physical vapour deposition

QD	Quantum dot
Qubit	Quantum bit
RCDA	Resistance curve derivative analysis
rGO	Reduced graphene oxide
RIE	Reactive ion etching
SE	Secondary electrons
SEM	Scanning electron microscope
SET	Single electron transistor
SG	Side gate
SKA	Secondary knock-on atoms
SLG	Single layer graphene
SNC	Southampton Nanofabrication Centre
sr	Short-range disorder
STEM	Scanning transmission electron microscope
STM	Scan tunnelling microscope
SV	Single vacancy
SW	Stone-Wales (defect)
TG	Top-gate
TKA	Tertiary knock-on atoms
TLG	Trilayer graphene
UEM	Ultrafast electron microscopy
UHV	Ultrahigh vacuum
VRH	Variable range hopping
WD	Working distance
XPS	X-ray photoelectron spectroscope

LIST OF ABBRIVIATIONS

Al	Alumnium
AlO_x/Al_2O_3	Aluminium oxide
Ar	Argon
Au	Gold
C	Carbon
GaAs	Gallium arsenide
H_2	Hydrogen
He	Helium
LHS	Left hand side
MoS_2	Molybdenum disulfide
N_2	Nitrogen
Ne	Neon
Ni	Nickel
O_2	Oxygen
Pb	Plumbum
RHS	Right hand side
Si	Silicon
SiO_2	Silicon dioxide
Sn	Tin
Ti	Titanium

LIST OF SYMBOLS

A	Area of the pattern
$a1, a2$	Lattice vectors of graphene
A_{ci}	Constant for charged impurity scattering
A_{mg}	Constant for mid-gap scattering
$b1, b2$	Reciprocal lattice vectors of graphene
$C(\lambda)$	Constant in the Tuinstra-Koenig relation
C_A	Weighing factor of the activated region
C_{BG}	Back-gate capacitance
C_{dot}	Quantum dot capacitance
C_{PG}	Plunger gate capacitance
C_S	Weighing factor of the structually disordered region
C_{SG}	Side-gate capacitance
e	Elementary charge
E_0	Characteristic field
E_A	Activation energy
E_{bulk}	Total energy of perfect grahpene
E_C	Charging energy
$E_{C.O.}$	Cross-over field
E_{CG}	Coulomb gap
E_d	Total energy of grahpene containing defects
E_{form}	Formation energy of defcts
f_A	Fraction of activated region
f_S	Fraction of structurally disordered region
G	Conductance
G_0	Prefactor in Mott VRH
$G1$	Prefactor in the field assisted VRH
g_F	Constant density of states near Fermi level
I	Beam current
$I(D)$	Intensity of Raman 'D' peak
$I(D')$	Intensity of D' peak
$I(G)$	Intensity of Raman 'G' peak
I_d	Drain current
K, K'	Dirac points of graphene's reciprocal lattice
k_B	Boltzmann constant
L	Length
L_a	Crystallite size in disordered graphite
L_D	Average distance between point defects
L_{irr}	Irradiation length
l_{mfp}	Mean free path

L_{sep}	Separation length
N	Number of removed/added carbon atoms
n	Carrier density
n^*	Intrinsic carrier density
n_D	Density of defects
n_{imp}	Density of charged impurity
n_p	Hole concentration
N_{rep}	Number of repetitions (for helium ion exposure)
p	Exponent
q	Momentum vector
R_0	Effective radius of vacancy
R_A	Surface roughness
r_A	Radius of the activated region in defective graphene
R_{dot}	Quantum dot radius
r_S	Radius of the structurally disordered region in defective graphene
s	Exponent in the field assisted VRH
T	Temperature
$T0$	Mott coefficient
T_d	Displacement threshold
t_{metal}	Metal thickness
t_{ox}	Oxide thickness
T_R	Scan delay time
t_{resist}	Resist thickness
V_{BG}	Back-gate voltage
V_{CNP}	Gate voltage at charge neutrality point
V_d	Drain voltage
v_F	Fermi velocity
V_g	Gate voltage
$V_{g,min}$	Gate voltage at minimum conductivity
V_{SG}	Side-gate voltage
V_{TG}	Top-gate voltage
W	Width
w	Reduced activation energy
W_{irr}	Irradiation width
$\Gamma(G)$	FWHM of G peak
Δd	Pixel spacing
ΔD	Total dose
ΔD_0	Dose for each repetition
ΔV_g	Plateau width of the conductivity minimum
ε	Permittivity
ε_0	Permittivity of vacuum

ε_r	Relative permittivity
λ	Excitation wavelength
μ	Carrier mobility
ξ	Localisation length
ρ_s	Resistivity due to short-range disorder
σ	Conductivity
σ_{ci}	Conductivity contributed by charged impurity scattering
σ_{mg}	Conductivity contributed by scattering through midgap states
σ_{min}	Minimum conductivity
σ_{res}	Residual conductivity
σ_{sr}	Conductivity contributed by short-range disorder
τ	Dwell time
φ_c	chemical potential of a carbon atom being removed or added
ω_D	Debye cut-off frequency

LIST OF FIGURES

LIST OF TABLES

Chapter 1 Introduction

1.1 Overview of research

Graphene, an allotrope of carbon with a unique two-dimension hexagonal structure, was first isolated in 2004[1,2] and is the first member of a new family of materials called 2D atomic crystal[3]. Many properties of graphene are record-breaking and could be exploited to solve many long-standing challenges. For instance, the room-temperature carrier mobility in graphene can reach ~2×10^5 $cm^2V^{-1}s^{-1}$[4], which not only is essential for high-speed electronics, but also a very important factor to make high band width photo-detectors. Graphene is a mechanically strong material with a Young's modulus (~1 TPa)[5] as good as that of carbon nanotube and diamond, a key property to achieve flexible electronics. In addition, graphene, which dissipates heat better than any other known material[6], along with the capability to bear large current density[7], is a leading contender for transparent electrode which now are dominated by expensive indium tin oxide (ITO). Last but not the least, graphene provides a natural platform for studying physics of 2D electron gas, an important structure for realizing spin-based quantum bit (qubit)[8]. Graphene is regarded as a promising candidate for spin qubit since owing to the long coherence time of carbon based materials. As a result, the last decade saw the flourishing of graphene research on almost every aspect from fundamental science to practical applications.

However, just like other solids, there are imperfections in graphene's lattice[9]. These imperfections manifest themselves as lattice distortions, point defects, extended line defects, impurities/dopants and grain boundaries[10]. They appear as a side effect of processing the material, that is, graphene is damaged to some extent after chemical treatment, lithography, etching, etc. The presence of these imperfections can affect the

intrinsic properties of graphene significantly. Previous experiments showed that defective graphene has a degraded electrical conductivity compared with its single-crystalline counterpart[11,12]. However, graphene subject to deliberate ion irradiation shows a transport gap which can be useful for logic applications [13]. More interestingly, theory [14] suggested that grain boundaries can either allow or completely reflect the transmission of charge carriers depending on the grain boundary structures. For unconventional device applications, theoretical work[15] proposed that a line defect can filter the charge carriers with specific valley polarisations. As a result, studying and engineering these defects to utilise their unique properties is a very important aspect of research on graphene and other 2D materials.

Depending on the type or scale, defects can be experimentally formed in different ways[10]. A 'top-down' approach is usually used to create lattice distortions and point defects in graphene. This may be done by irradiating the graphene sample with accelerated electrons as in a transmission microscope[16–18]. Under electron impact, the C-C bond can rotate if the formation energy of such rotation is supplied. A notable is a Stone-Wales defect where a C-C bond is rotated by 90^{o}, which has been experimentally observed[19]. Because the three-fold lattice structure is still valid, the Stone-Wales defect is a relatively stable one. In theory, once the incident particle's energy exceeds the threshold value for the displacement of one carbon atom in the hexagonal lattice, vacancies can be created[20]. Regardless of the vacancy type, the number of dangling bonds are remained minimum and non-hexagonal structures are formed to stabilize the sp^2 network[10]. On the other hand, extended line defects and grain boundaries can be introduced by a 'bottom-up' approach[21]. Graphene grown by chemical vapour deposition is polycrystalline. Single-crystalline domains first nucleate from multiple sites and continue to grow until they merge with one another. The grain boundaries that stitch these separate domains together are usually chains of non-hexagonal structures. A special type of grain boundary where the graphene domains on each side don't have a disorientation angle is called an extended line defect.

The presence of defects poses a great challenge to the fabrication of graphene nano-devices. Resolution of conventional electron-beam lithography (EBL) cannot go very further beyond 20nm feature size[22–28], far from atomic resolution required to realize some novel applications[13,29,30]. Several fabrication methods were researched to

address the issue including direct ion beam writing[31–35], transmission electron microscope lithography[36,37]. These methods are all based on the knock-on mechanism. Despite of the reasonably better resolution, the damage extent introduced into the graphene lattice is not well studied. The thoroughly understanding of the inter-play between ion/electron beam and graphene is an essential step towards more advanced fabrication technology of this kind.

1.2 Motivation and contribution

Because of the fascinating properties of defects in graphene, it is highly desirable to utilising the state-of-the-art nanofabrication tools to make artificial defects in a controllable manner. The recent development of the scanning helium ion microscopy (HIM) offers the flexibility to modify graphene's surface topology from point defects to larger area sputtering. In particular, the imaging capability and beam damage of HIM on graphene has been studied[38]. The HIM-based fabrication of graphene and two-dimension material have been demonstrated with very promising down-scaling potential[13,29,30,33]. Similar to a scanning electron microscope (SEM), in a HIM, the Helium ions are emitted from an atomically sharpened source under high electric field. The incident ions yield large number of secondary electrons inside the sample, thus forming an image. Compared with conventional SEM, HIM offers an enhanced imaging resolution (<1nm) owing to the shorter De Broglie wavelength of helium. In the meantime, helium has a more effective knock-on impact on graphene's hexagonal lattice meaning that it is possible to directly writing complex patterns on graphene by scanning the beam across the sample surface which can be achieved by adding a devoted pattern generator.

Since HIM is a newly-developed instrument, there has not yet been a systematic study on the HIM-irradiated graphene and its electrical behaviours, to our best knowledge. The variable range of beam energy and exposure dose could allow for the introduction of a wide range of defect levels at specific locations in a device. More specifically, the transition of graphene from semi-metal to insulator due to disorder can be used as an important component in device engineering.

In this work we aim to integrate helium ion exposure to current nanofabrication technique to realise a 'top-down' approach for precision defect-engineering on graphene. We start

by identifying the damage extent of helium ion bombardment on graphene using Raman spectroscopy. This also includes the optimisation of sub-10nm helium ion milling technique and its potential impact on graphene. The results can be applied to other 2D materials supported by substrate. We then carry out transport measurement to study the electrical properties of the above-mentioned disordered system by gradually varying the irradiation dose. We found a series of effects on electrical characteristics of graphene nanoribbon (GNR) caused by ion irradiation. Finally, we propose a lateral quantum tunnelling device that incorporates the 2D insulator created by HIM irradiation using the discoveries obtained in our work.

1.3 Document Organisation

This thesis explores an approach to develop defect-modified graphene devices via controlled ion bombardment to specific locations within a channel as a stepping stone towards future 'top-down' precision defect engineering of 2D materials devices.

Chapter 1 outlines an overview of our research field, highlighting the previous developments and challenges we face, thus the motivation behind this work and our intended contributions. Chapter 2 briefs the theory behind our research topic including transport in graphene, basic configurations of defects in a hexagonal lattice, the formation of several types of defects and mechanism of ion bombardment. After this, in Chapter 3 I summarise the most recent and important developments in graphene research related to our research through a literature review. In Chapter 4 and 5 I detail our original contributions to the field. I will explain the e-beam lithography (EBL) based fabrication process as an important constituent part of our EBL-HIM hybrid fabrication method. This is accomplished by sub-10 nm helium ion lithography. A detailed analysis of HIM milling's impact on graphene will be given leading to an improved fabrication method focusing on moderate irradiation. Last I will discuss the electrical measurement on the recent devices made with this method. I conclude this thesis in Chapter 6, summarising our findings, achievements and outlining potential directions for future work.

Chapter 2 Research background

2.1 Basics of electronic transport in graphene

The graphene lattice is a triangular one with two carbon atoms per unit cell (Figure 2.1). The carbon-carbon distance in graphene is a=0.14 nm. The lattice vectors are ***a1***, ***a2*** (|***a1***|=| ***a2***|=$\sqrt{3}a$) in real space and ***b1***, ***b2*** in reciprocal space. The first Brillouin zone is shown in Figure 2.1 (b). The two Dirac points are labelled K and K'.

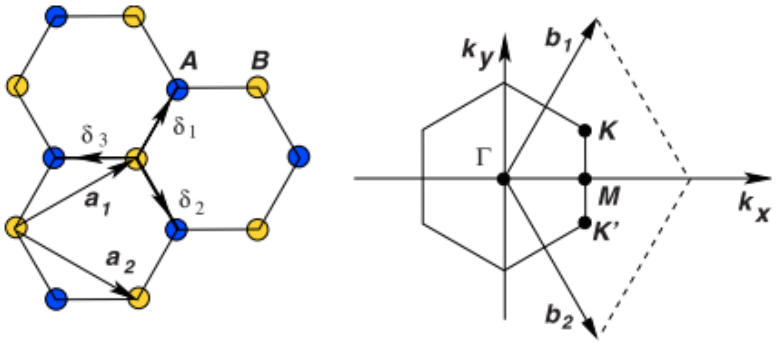

Figure 2.1 (a) lattice structure of graphene. (b) The first Brillouin zone of graphene [39].

The band structure of a single carbon layer is calculated in reference [40]. A tight-binding approach, which considers the hopping of electrons to the nearest-neighbour and next nearest-neighbour atom, is used. The band structure is shown in Figure 2.2. The energy dispersion near the Dirac point (i.e., ***k***=***K***+***q*** and |***q***|<<|***K***|) is almost linear, $E_{\pm(\boldsymbol{q})} \approx \pm v_F|\boldsymbol{q}| + O[(q/K)^2]$, where v_F is the Fermi velocity and is around 1×10^6 m/s[41]. As a result, graphene is a zero band-gap semiconductor that has a linear energy-momentum relationship with conduction band and valence band intersecting at the Dirac point. The

Fermi velocity is a parameter that is dependent on the hopping energy between nearest neighbor $t \approx 2.5$ eV and graphene's carbon-carbon distance a: $v_F = 3ta/(2\hbar)$.

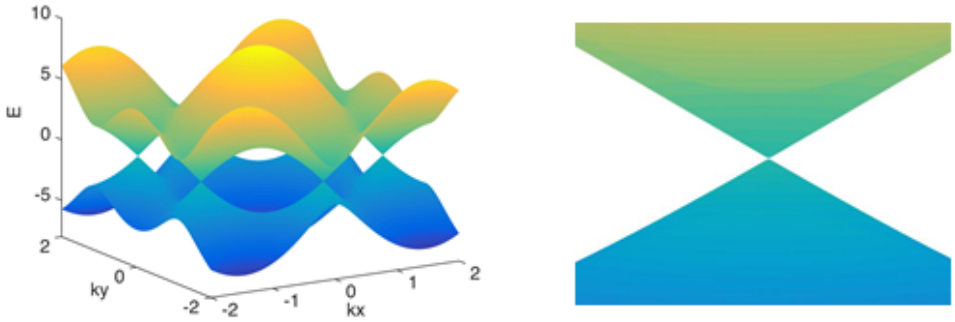

Figure 2.2 Left: band diagram derived from the tight-binding Hamiltonian. Right: the linear energy-momentum dispersion near the Dirac point.

The linear dispersion leads to a couple of interesting (peculiar) phenomena, such as a carrier density-independent interaction parameter and carrier density-independent Coulomb screening[42].

2.2 Transport in graphene devices

In clean graphene sample where the amount of disorder is so small that the mean-free path is comparable to the distance between contacts, i.e., ballistic transport. However, in most experimental work, graphene samples are 'dirty' and therefore are in the diffusive regime. The diffusive transport in graphene on substrate is due to various possible scattering sources which contribute to the conductivity σ as follows according to the Matthiessen's rule [43]:

$$\sigma^{-1} = \sigma_{ci}^{-1} + \sigma_{sr}^{-1} + \sigma_{mg}^{-1} + \cdots, \qquad \textbf{2.1}$$

where the subscriptions denote: charge impurities (ci), short-range scatterers (sr) and mid-gap states (mg). These three mechanisms are the dominant scattering mechanisms at room temperature and low temperature therefore are of our primary interest. Other less dominant scattering mechanisms include corrugations[44] and phonon scattering[45].

The scattering of charged impurities (which can reside in the SiO_2 substrate) is predicted to produce a conductivity σ with a linear dependence on the carrier density n as follows[42,46–49]:

$$\sigma_{ci}(n) = A_{ci} e \left| \frac{n}{n_{imp}} \right|, \qquad \textbf{2.2}$$

where n_{imp} is the density of impurity charges and A_{ci} is a constant which has a calculated value of ~5×10^{15} $V^{-1}S^{-1}$[42]. Charged impurity scattering in graphene has been experimentally investigated by means of potassium dosing[50,51] and is considered the dominant limiting factor of carrier mobility in a graphene-on-SiO_2 system[52].

Another major scattering source that can result in a roughly linear conductivity against n is the resonant scatterers producing mid-gap states. Theoretically predicted resonant scatterers are vacancies[53,54] or strongly bound monovalent adsorbates[55–57] and is predicted to have the following form[54]:

$$\sigma_{mg}(n) = A_{mg} e \left| \frac{n}{n_d} \right| [ln\,(\sqrt{\pi n} R_0)]^2, \qquad \textbf{2.3}$$

where A_{mg} is a constant, n_d is the defect (vacancy) density and R_0 is the effective radius of the vacancy.

The short-range scattering can be due to weak point-disorder defect such a noble-gas atom trapped by carbon vacancy[12], although the exact physical origin is still not clear. This type of scatterers is predicted to lead to *n*-independent conductivity, i.e. $\sigma_{sr}(n) \propto constant$[58]. Therefore $\sigma_{sr}(n)$ may introduce sub-linearity to the total conductivity $\sigma_{(n)}$ when in combined with other scattering sources as described in equation 2.1. Since the short-range scatterers are atomic-scale, they are hardly affected by the dielectric environment of the graphene[59].

If the three scattering mechanisms discussed above (i.e., charged impurity, short-range disorder and weak point-disorder) are considered. Equation 2.1 can be simplified by taking into account the (linear) *n*-dependent and *n*-independent conductivity:

$$\sigma^{-1} = (ne\mu)^{-1} + {\sigma_{sr}}^{-1}, \qquad \textbf{2.4}$$

where e is the elementary charge, n is carrier density, μ is carrier mobility and σ_{sr} is conductivity due to short-range disorder.

The carrier density in single layer graphene can be modulated electrically via gating. A standard configuration is a graphene and a back-gate with a dielectric of thickness t_{ox} in between. The induced carrier density n is given by:

$$n = CV_g/e, \qquad \textbf{2.5}$$

where C is the gate capacitance per unit area $C=\varepsilon/t_{ox}$ as in a parallel-plate capacitor, where t_{ox} is the oxide thickness.

The conductivity σ at intermediate carrier density where the sub-linearity caused by σ_{sr} is negligible can be fit as follows(as illustrated in Figure 2.3) [50]:

$$\sigma = ne\mu + \sigma_{res}, \qquad \textbf{2.6}$$

where e is electron elementary charge, n is carrier density and μ is carrier mobility. σ_{res} is the residual conductivity determined by fit and should not be confused with the minimum conductivity σ_{min}. Both values are defined at zero carrier density. The origin of σ_{min} is not clearly revealed yet, though the inhomogeneity due to charged impurities is suggested to cause σ_{min}[39,60]. In practice, at n=0, the electron branch and hole branch of conductivity do not intersect at $\sigma_{res.}$ Instead, σ curves gently and settles at σ_{min} giving rise to a plateau width ΔV_G.

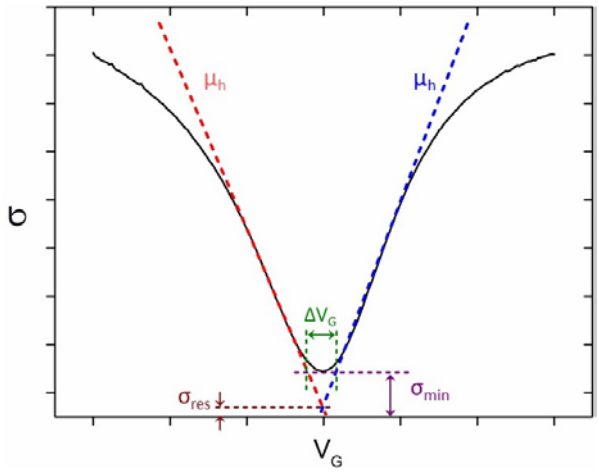

Figure 2.3 Ambipolar conductivity as a function of gate voltage.

2.3 Defect structures in graphene

As the centre of the present study, defects in graphene has significant influence on graphene's electrical, optical, mechanical and thermal properties. In this section, we discuss a few types of structural defects present in graphene's hexagonal lattice.

Compared to other material, graphene is very 'adaptive' in that it is capable of hosting defects by reconstructing its atomic arrangement[61], since sp^2 bonds occur not only in hexagon structures but also in other polygons. However, these non-polygon regions may introduce curvature[62].

Let us first recall the classification in convention bulk materials. Depending on the presence of foreign atoms, defects can be described as intrinsic (without foreign atoms, e.g. dopants and impurities) and extrinsic. In terms of dimensionality, point defects such as vacancies or interstitial atoms are zero-dimension (0D). Line defects are thus one-dimension (1D). Grain boundaries and stacking faults are two-dimension (2D). Finally, inclusions and voids are three-dimension (3D). On the other hand, the two-dimension nature of graphene dictates that there are virtually no 3D defects in graphene.

The first type of defects in graphene is 0D point defect including Stone-Wales defect, single/multiple vacancies and adatoms. One important quantity used in theoretical calculation to evaluate the stability of defects is the formation energy, which is calculated as $E_{form} = E_d - (E_{bulk} + N\varphi_C)$, where E_d is the total energy of graphene with defects, E_{bulk} is the total energy of perfect graphene and φ_C is the chemical potential of carbon atoms being removed (negative N) or added (positive N) [63]. The lower the E_{form}, the more stable the defects. The Stone-Wales (SW) defect manifests itself as a 90^o rotation of C-C bonds (see Figure 2.4 (a)), that is, four hexagons evolve into two heptagons and two pentagons (SW(55-77))[19,64]. Note this type of defect does not involve removal or addition of carbon atoms. The formation energy for SW defect is ~5 eV and a kinetic energy barrier of ~10 eV needs to be overcome for this transformation to take place (see Figure 2.4 (b)). Such a high kinetic energy barrier ensures the negligible density of SW defects in graphene at room temperature. For the same reason, SW defects can be very stable once formed. However, sometimes although the energy introduced by ion irradiation is less than what is required for the knock-on displacement of a C atom, it is still high enough to create a SW defect.

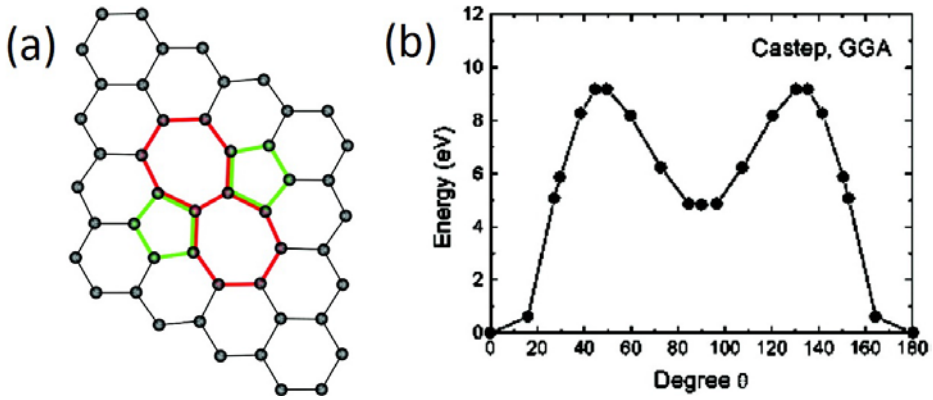

Figure 2.4 (a) a Stone-Wales defect. (b) the energy barrier for bond-rotation [10].

When the energy perturbation is greater than the displacement threshold (T_d), carbon atoms can be knocked out leaving behind vacancies. The formation energy for a single vacancy (SV) is ~7.5 eV. Three dangling bonds are initially created once a carbon atom is displaced[65]. The relaxation of the lattice forms a defective region with a five-atom and a nine-atom structure where two of the dangling bonds connect. The situation for double vacancy (DV)[61,66] becomes a bit more complex in that the vacancy can 'mutate' into many shapes. A simple DV can be formed by merging two SV or by removing two adjacent carbon atoms. As shown in Figure 2.5, the defect reconstructs itself to a two-pentagon and two-heptagon structure (5-8-5). However, the (5-8-5) structure is not the most energy-favorable type of DV. A bond in the octagon can rotate 90^o so that (5-8-5) evolves to a (555-777) structure. If such bond-rotation happens in one of the heptagons in a (555-777) structure, the defect further becomes a 5555-6-7777 defect. Note the (555-777) defect has the smallest E_{form} of the three. Vacancies can also move around in the lattice. The migration energy is about 1.3eV for a single vacancy and about 7eV for a double vacancy. Therefore, the DV is much more immobile compared to a SV.

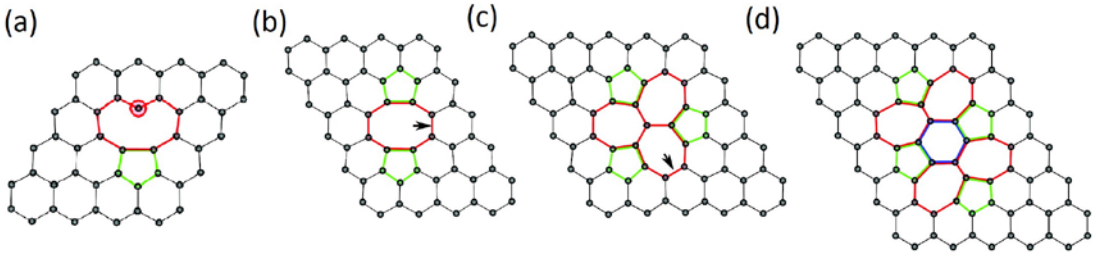

Figure 2.5 The evolution of a point defect: (a) single vacancy, (b) 5-8-5 (c) 555-777 and (d) 5555-6-7777 defect [10].

Instead of removing individual atoms to create single or double vacancies, an instant impact to the carbon network (e.g. bombarded by an ion) could lead to the loss of a large

number of atoms thus reducing the surface area significantly. Therefore, the rearrangement into non-hexagonal structures would have required the graphene sheet to warp where a high energy is needed. In such case, holes are usually formed where the surrounding atoms rearrange themselves accordingly to saturate the number of dangling bonds.

Adatom is another type of point defects that can exist in graphene[62]. When a carbon atom is brought close to the surface of graphene, the native atoms in graphene can form covalent bond with the additional carbon through sp3 hybridization. An energetically favorable position for the adatom to be is on top of one C-C bond (Figure 2.6(a,d)). The binding energy is around 2 eV. Also it is easy for such adatom to migrate around the graphene surface due to small migration energy ~0.4 eV. An atom sputtered out from graphene can immediately become an adatom on the surface. It is also favorable for two adatoms to form a dimer and bond with graphene by inducing local curvature. An example of such defect is the Inverse Stone-Wales defect (Figure 2.6(c,f)). Not only carbon, but also many foreign atoms can bond with graphene as adatom. Depending on the bonding strength, the adsorption can be either physisorption (weak, van der Waals bond) or chemisorption (strong, covalent bond). Previous experiment suggests weak bonding between perfect graphene and transition metal as they easily migrate on the surface (activation energy ~ 0.28 eV). However, defects can become a suitable site to trap foreign atoms. Also the strain near the defect causes attraction to the metal atom on the surface enhancing the adsorption (Figure 2.7). A part from adsorption, foreign atoms can also replace carbon in graphene as substitutional defect. Atoms with similar atomic size to carbon such as nitrogen and boron are natural dopants. Transition metal atoms can also be incorporated into the graphene network substitutionally with off-layer topology. Such substitutional defect is usually quite stable once formed.

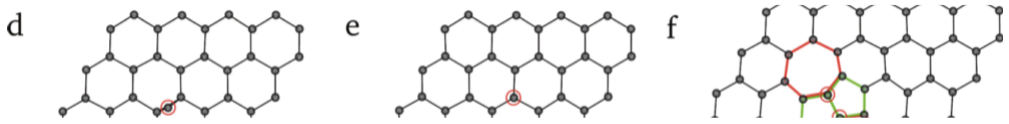

Figure 2.6 Carbon adatom (a) single adatom above the bond (b) dumbell configuration and (c) inverse-SW defect [10].

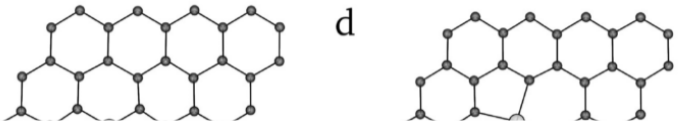

Figure 2.7 metal adatoms bonding on the vacancy sites [10].

A summary of formation and migration energies (calculated from theoretical work) of 0D point defects in graphene is given in below in Table 2-1:

Table 2-1 Summary of calculated formation and migration energies of point defects in graphene

Defect type	**Atomic structure**	**Formation energy (eV)**	**Migration energy (eV)**	**References**
Stone-Wales	55-77	4.3-5.3	10	[63,64]
Single vacancy	5-9	7.3-7.5	1.2-1.4	[65]
Double vacancy	5-8-5 555-777 555-6-777	7.2-7.9 6.4-7.5 7	7 6 6	[65,66] [18,61]
Adatom		6-7	0.4	[67]
Inverse SW	57-57	5.8		[62]

The last type of defects we discuss is the 1D line defects, sometimes called extended line defects. The line defects usually appear as grain boundaries of two merging domains with different lattice orientation. This is very common in CVD graphene grown on metal due to inevitable lattice mismatch. The atomic structures of the boundaries and size of the grains dictate the electronic properties of the grown graphene. One example studied

experimentally is the grain boundary of graphene grown on Ni[21] surface, where periodic alternations of pentagon pairs and octagons form the boundary due to mismatch of two graphene domains (Figure 2.8).

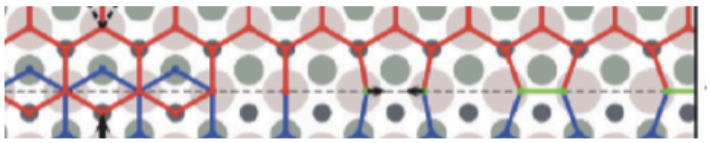

Figure 2.8 The formation of grain boundary between two graphene domains grown on Ni [21].

2.4 Basics of ion irradiation

Although graphene is only one atomic thick, particle irradiation on graphene can be highly affected by its underlying substrate. Therefore, revisiting the basics of ion irradiation in bulk material would be beneficial for our present study.

When a particle, being an electron or an ion, penetrates a solid, it loses energy through collisions with nuclei and electrons in the target. In the case of ion, capturing the electrons in the target soon neutralizes its charge. If the recoil atom has enough energy to leave its lattice position, a point defect such as a vacancy-interstitial pair is left in the target.

The stopping of particle in the solid can be attributed to two mechanisms: nuclear stopping and electronic stopping[68]. The nuclear stopping is due to the ballistic collision between the incident ion and nuclei and the kinetic energy of the ion is transferred to the translational movement of the target atom. As a result, it is the Coulomb interactions and the momentum transfer that determine the energy loss. The nuclear stopping is the main stopping mechanism when the energy of the incident particle is relatively low (<100 keV/amu). For high energy ions, a more suitable scenario called 'binary collision approximation' is used. In this situation, the incoming ion is assumed to travel in straight line between independent nuclei collisions and the power loss is predominantly due to

electronic stopping, i.e., the inelastic collision with electrons. The term 'binary' means that only two particles are involved in each collision.

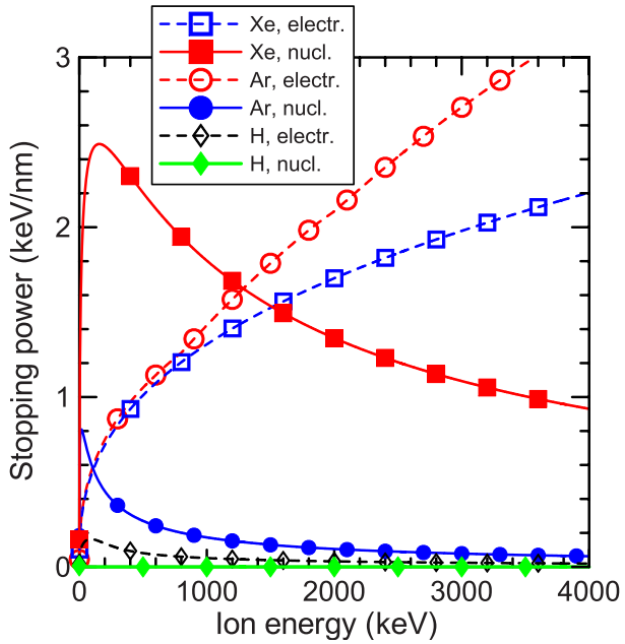

Figure 2.9 Calculated nuclear stopping power in C target for different ion species as a function of ion energy [68].

Figure 2.9 shows the nuclear and electronic stopping powers of different ions as a function of ion energy. The crossover of two stopping mechanisms depends on the ion mass. Note that electronic stopping is dominant at all energies for light ions such as H^+ and He^+ (not shown here in Figure 2.9).

Damages can form during the cascade development after ion irradiation. Depending on the ion energy and mass, several collision cascades are responsible for the defects formation process. In the case of low mass ions hitting a target with low density, a simplest case called 'linear cascades' best predicts the damage extent where the energetic ion penetrates the target while generating a sequence of independent recoils. Depending on the colliding sequence, the recoil atoms are ranked as follows: primary knock-on atoms (i.e., the ion initiating the collision, PKA), secondary knock-on atoms (SKA), tertiary knock-on atoms (TKA), etc. Once the knock-on atom energy is lower than T_d, no further damage can be made. When the ion is heavy and the target is relatively dense, the collisions occur near each other and therefore cannot be considered as independent ones

since they overlap. Therefore the interaction in this case cannot be simplified as in the binary case, instead it is treated by 'heat spike' generated by pressure waves due to ion impact (for instance, Au target hit by 20keV/atom Au cluster [69]). In many cases, linear cascade and heat spike both contributes to the collision event. In the early stage of the collision, the linear cascade prevails since the ion has not lost much energy. However, the much-slowed ion or its recoils are more easily to collide with nuclei and therefore the heat spike regime becomes dominant. When the ion energy is heavy and very energetic (MeV or GeV), they are called swift heavy ions. Swift heavy ions normally generate an amorphous region along therefore track due to both electron stopping and heating.

Several experimental methods exist for studying defects in graphene. A transmission electron microscope (TEM) forms images by collecting the accelerated electrons that transmits through the sample. Modern aberration-corrected high resolution TEM (HRTEM) has a much-improved imaging resolution compared to conventional TEM allowing for real-time observation of defects with atomic accuracy[9,16,70,71]tm. The scan tunnelling microscope (STM) provides similar resolution as that of a TEM but with a different working principle where image is formed by measuring tunnel current between the scanning tip and sample surface[60,72,73]. One should note that neither TEM nor STM is capable of observing the defect creating process as none of them can resolve events occurred in picosecond timescale[68]. The recent development of four-dimensional ultra-fast electron microscopy (4D UEM) which employs a precisely pulsed laser is able to generate single-electron packets for imaging with high resolution in both space(sub-nm) and time (femtosecond) and is a promising candidate for achieving real-time observation of structural changes in graphene[74,75]. In addition, irradiation with ions is another method to create defects in graphene. A handy tool would be a focused ion beam (FIB) system which has the ability to send <100 keV accelerated ions since it offers controllable creation of defects in graphene. An advantage of FIB is it does not need the graphene to be suspended as in a HRTEM. Direct milling is also possible with a FIB system due to large momentum transfer from accelerated ions. Fabrication of <10nm wide graphene nanoribbon has been demonstrated by using a focused helium ion beam[30,33,35].

Chapter 3 A review on defect engineering and characterisation of graphene

3.1 Generation and evolution of defects: TEM study

Thanks to the atomic resolution, the aberration-corrected transmission electron microscopy (TEM) has been used extensively to study the creation and evolution of defects in graphene *in situ*. Kotakoski *et al*[76] explored the transformation of point defects in graphene under controlled TEM irradiation and showed that these vacancies tend to reorganize and grow to more complex amorphous structures with rotated hexagon domain surrounded by other polygons.

The acceleration voltages were carefully selected to serve different purposes. For instance, a suspended graphene was first irradiated at 300 keV, which is value high enough to knock out carbon atoms from the sp2 network. The sample was imaged at 80 keV to prevent further knock-on damage but to allow for some bond rotation. Lastly 100 keV was used to allow for a full re-bonding to observe the most energetically-favourable defect structures in graphene. Note that the TEM voltage threshold for the displacement of sp2 carbon atoms in graphene is 86 keV[77].

The authors first found that the graphene remains a coherent membrane after irradiation at 100 keV with a dose of 10^{24} cm^{-2} where many polygons are formed with only very few holes. This is contrary to the expectation that irradiated membrane will become largely porous or curve into the third dimension. The author then used the 300 keV beam to create

initial defects and then observed them at 80 keV in order to better illustrate evolution of these defects.

It was found that initial 300 keV irradiation primarily created single vacancies, which in turn, tend to collapse to divacancies due to the ejection of the under-coordinated atom (Figure 3.1(b-d)). This formation process from single vacancy to double vacancy does not necessarily require additional energy input (e.g. from electron/ion irradiation) since the formation energy of two types of vacancies are comparable[10]. Ideally, since all carbon atoms are now connected by sp2 bonds, no more atoms should be sputtered at 80 keV. However divacancies can have a variety of configurations (such as 5-8-5, 555-777, 5555-6-7777, etc. [10]) and they change to one another via bond rotation due to energy perturbation (barrier ~ 5 eV)， as can be seen in Figure 3.1(c-f). Although 80 keV is lower than Td, it is higher enough to cause bond rotation and reorientation (Figure 3.1(a, e, f)).

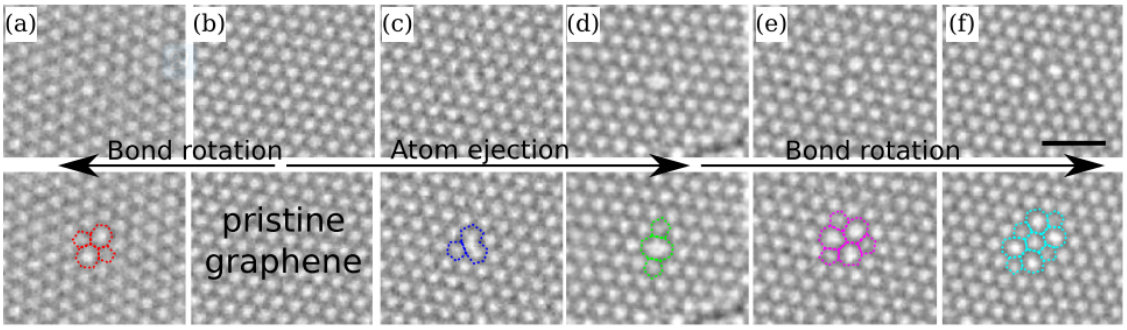

Figure 3.1 Defect creation and evolution in graphene under TEM imaging. From pristine graphene (b), a SW defect is formed by bond rotation (a), when beam energy is low. At high beam energy, atom is dislodged as in single vacancy (c) followed by double vacancy (d). Further bond rotation drive the initial double vacancy to more stable configurations (e,f). Scalebar = 1 nm [76].

More interestingly, defects located at different places were found to agglomerate and align along the zigzag direction of the graphene lattice. This is facilitated by the 80 keV irradiation where electrons carry energy less than T_d allowing for the re-bonding in the irradiated area. For instance, a 555-777 divacancy was found to gradually 'move' towards another defect with four missing atoms. The double vacancy transformed from 555-777 to 5-8-5, to a dislocation dipole ((Figure 3.2(c)), and finally merged with the other defect forming an aligned divacancies (Figure 3.2(a-d)). Among the three configurations of divacancy, the dislocation dipole has the highest energy while the 555-777 has the lowest. The divacancy structure hops between different configurations as a result of moving between local energy minimums driven by the electron beam. Note that no atom is

knocked out in this process. Figure 3.2 (e) shows two routes of the migration of a 5-8-5 defect. In the first route, the initial 5-8-5 defect first transformed into a 2×(5-7) defect by rotating bond A and further changed to the final 5-8-5 by rotating bond C. In the second possible route, the initial 5-8-5 first transformed into a 555-777 defect by rotating bond B and into the final 5-8-5 shape by rotating bond D.

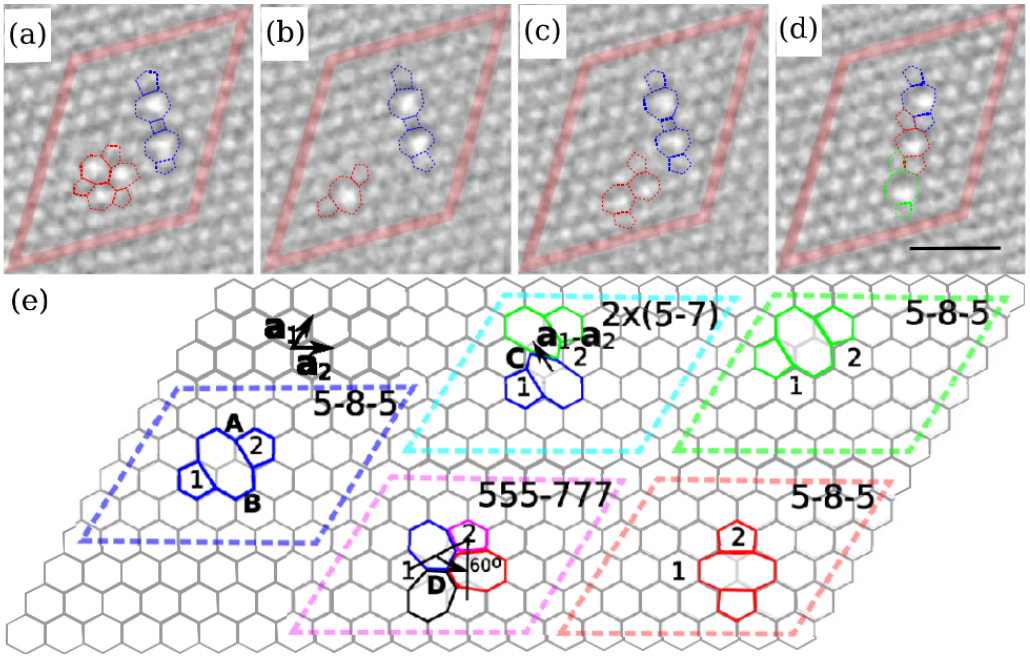

Figure 3.2 (a-d)Beam-driven migration of divacancies. (e) migration of a 5-8-5 defect due to two possible bond rotatoins. Scalebar = 1 nm [76].

Lastly the authors studied a special type of defect structure which can be thought as three 5-8-5 divacancies lined up with the overlapping area replaced by tetragons (Figure 3.3(a)). The edge of this defect is aligned with the armchair edge of surround graphene lattice, therefore is a relatively stable configuration. Under the exposure of 100 keV electron beam, the defect started to change structure until 24 atoms were sputtered (Figure 3.3(b-h)). The initial three-divacancy was replaced by Stone-Wales type defects, dislocation dipoles and 5-8-5 structures. Finally, the missing atoms were accommodated by the formation of a clustered hexagons rotated 30^{o} with respect to the graphene lattice. The miss-oriented patch of hexagons was surrounded by a chain of alternating pentagons and heptagons. This type of defects consisting of rotated hexagons were found to have the lowest energy among all the multivacancies as calculated by DFT method.

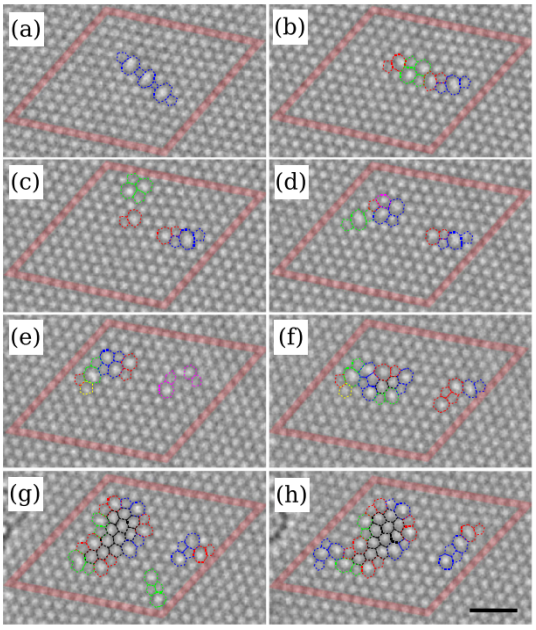

Figure 3.3 Formaiton of defect clusters under 100 kV beam irradiation. Scalebar = 1 nm [76].

In conclusion, this study illustrated, step by step, how some of the simplest defects in graphene develop under energetic particle irradiation and revealed a generally stable configuration of multivacancies, that is, rotated polygons bounded by polygons.

3.2 Raman Spectroscopy on graphene

Raman spectroscopy has been widely used to probe defects in covalent bonded nanomaterial such as graphene, hBN, MoS_2, etc. It's an important method because it is non-invasive and non-contact. In particular, the Raman spectrum can reflect the information about the defects in the lattice. Since the discovery of graphene, rapid development on Raman spectrum provides ways to evaluate sample quality and defects level, both qualitatively and quantitatively. A pioneering work from Lucchese and *et al* [72] studied the Raman scattering in defective graphene and proposed a model that relates the peak ratio to defect density. The reported method can give reasonable prediction on the defect length purely from the Raman data.

Raman spectroscopy is a well-established non-destructive method that monitors the structural and electronic properties of graphitic materials [72,78–82]. The Raman spectrum of pristine graphene consists of two distinctive features, known as G and 2D peaks which are located at around 1580 cm^{-1} and 2680 cm^{-1}, respectively. The G peak originates from the high frequency E_{2g} optical phonon while the 2D peak is associated

with the breathing mode of graphene hexagonal ring[79]. The presence of defects gives rise to another two features at around 1345 cm^{-1} (D peak) and 1600 cm^{-1} (D' peak), which initially are forbidden in non-defective graphene as a result of Raman selection rule. Being the undertone of 2D, D is also associated with the breathing mode of the honeycomb structure and is activated by the intervalley scattering of single phonon [79]. More importantly, the intensity ratio I(D)/I(G) can be used as a measure of defect density/length. A widely used model is the Tuinstra-Koenig relation $I(D)/I(G) \propto C(\lambda)/L_a$, where $C(\lambda)$ is the excitation energy (laser power) dependent constant, and La is the size of crystalline sp2 clusters. In this reviewed study, the authors proposed a more general model that describes the evolution of I(D)/I(G) over a large defect density range from Stage1 to Stage2.

An Ar^+ ion source in a UHV system was used to create defects in the sample. A low ion energy (90eV) that just above the T_d of surface C atoms was deliberately chosen to minimise the cascade effect. This is very important since point defects generated this way can be almost entirely attributed to the knock-on damage by the primary ions while the contribution from recoils can be ruled out. Also a 45^o incident angle was used to aid sputtering process.

The ion bombardment procedure was calibrated on highly oriented pyrolytic graphite (HOPG) (shown in Figure 3.4). STM images show that for irradiation dose of 10^{11} cm^{-2}, the defects are isolated from each other. As the dose goes above 10^{13} cm^{-2}, the defects start to coalesce. The hexagonal lattice structure becomes completely disordered for dose of 10^{14} cm^{-2}. The defect density was obtained by direct counting and is given by $L_D = 1/\sqrt{n_D}$, where L_D is the average distance between defects (i.e., defect length) and n_D is defect density. Raman data shows that the irradiation process was actually quite consistent since the *I(D)/I(G)* ratio shows same saturation trend as n_D increases for both HOPG and a graphite sample consisting of fifty graphene layers.

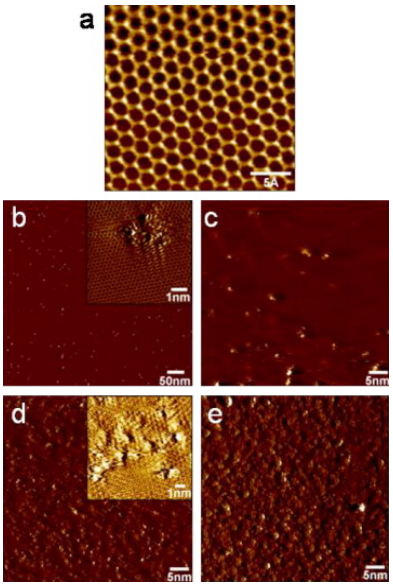

Figure 3.4 STM images of grahite surface bombarded with increasing 90 eV Ar^+ doses: (a-e) are 0, 10^{11}, 10^{12}, 10^{13}, 10^{14} cm^{-2}, respectively [72].

The Raman spectrum of irradiated graphene sample evolved at follows: 1) At low dose (10^{11} cm^{-2}), a very small D peak appears due to the presence of initial defects. 2) As irradiation dose increases (above 10^{13} cm^{-2}), all the peaks significantly broaden. 3) For further irradiation above 10^{15} cm^{-2}, the peak intensities decrease as a result of amorphisation and loss of carbon atoms.

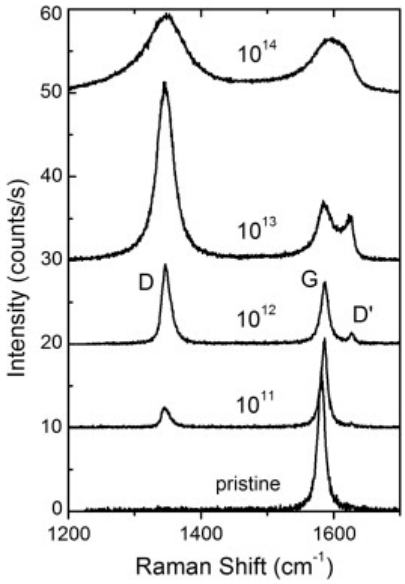

Figure 3.5 Raman spectra of graphene flake with different level of ion bombardment. *D* and *D'* peaks appear implying structural defects [72].

The I(D)/I(G) of irradiated graphene shows a non-monotonic change with defect length, which reaches maximum at L_D ~4 nm indicating a competing mechanism exists for the development of D band.

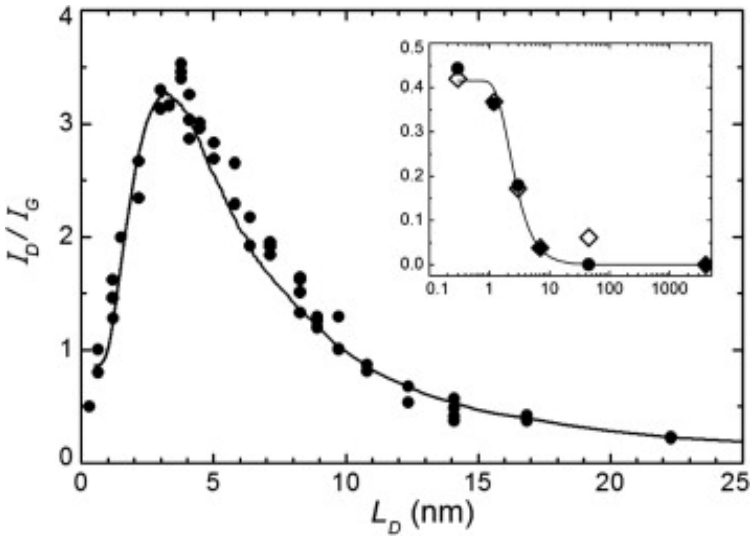

Figure 3.6 *I(D)/I(G)* v.s. L_D for three different graphene samples. The solid line shows the modelling from the equation discussed below. Inset shows the log scale *I(D)/I(G)* v.s. L_D data for two graphite samples with different thickness which showed almost identical trend suggesting the irradiation method was well calibrated [72].

The proposed model was based on a scenario where the probing of defects exetends to a so-called "Raman activated region" defined by two length scales r_S and r_A, which are the radii of the structurally disordered region (*S*-region) and the surrounding activated region (*A*-region), respectively. The phonon scattering contributes to *D* peak only if the electron-hole excitation is created in the *A*-region, otherwise it will either enhance *G* peak for e-h created outside *S*- and *A*- regions or suppress the *D* peak if it falls into *S*-region only (Figure 3.7 (a)). In Stage 1 when n_D is relatively low, the area of *A*-region expands with n_D causing *I(D)/I(G)* to increase. When n_D is sufficiently large that the whole area is covered by *S*- and *A*-regions, the fraction of *A*-region saturates marking the onset of Stage 2 (Figure 3.7(b-d)). In Stage 2, *A*-region converts to *S*-region as more defects are created giving rise to the decrease of *I(D)/I(G)* due to the loss of hexagonal rings (Figure 3.7(e)). Therefore, the non-monotonic change of *I(D)/I(G)* is a consequence of the balance of *S*- and *A*-regions, weighted by parameter C_A and C_S. The critical value of L_D at the transition of two stages is estimated by $L_D \approx v_F/\omega_D = 4$ nm, where v_F is the Fermi velocity and ω_D is the Debye cut-off frequency[83].

The model is hence describing the contribution from both parts:

$$\frac{I(D)}{I(G)}(L_D) = C_A f_A(L_D) + C_S f_S(L_D), \qquad \textbf{3.1}$$

where f_A and f_S are fractions of activated region and disorder region respectively.

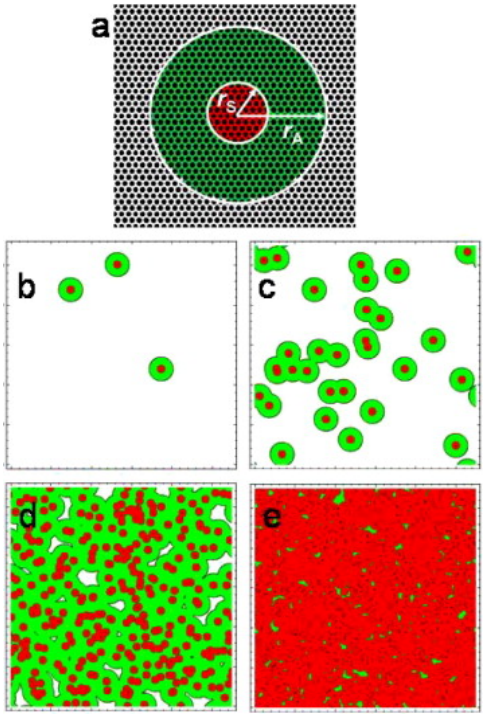

Figure 3.7 The activation model that simulates the defect generation in grahpene. (a) a point defect consisting of disordered region r_S and activation region r_A. (b-e) increasing bombardment causes r_A to overlap and finally be replaced by r_S [72].

The detailed relation between f_S and f_A were solved analytically by the following rate equation：

$$\frac{\mathrm{d}f_S}{\mathrm{d}\sigma} = \pi r_S^2 \left(1 - \frac{1}{f_S}\right), \qquad \textbf{3.2}$$

$$\frac{\mathrm{d}f_A}{\mathrm{d}\sigma} = \pi r_A^2 \left(1 - \frac{1}{f_S} - \frac{1}{f_A}\right), \qquad \textbf{3.3}$$

with the initial condition $f_S = f_A = 0$ when $\sigma = 0$.

Substituting the solved f_S and f_A into the original model gives:

$$\frac{I(D)}{I(G)}(L_D) = C_A \frac{r_A^2 - r_S^2}{r_A^2 - 2r_S^2}\left[e^{(-\pi r_S^2/L_D^2)} - e^{-\pi(r_A^2 - r_S^2)/L_D^2}\right] + C_S(1 - e^{(-\pi r_S^2/L_D^2)}) \qquad \textbf{3.4}$$

Fitting the above equation to the experimental data gives following reasonable values: C_A ~ 4.2, C_S ~ 0.87, r_S~1 nm and r_A = 3 nm. In particular, the r_S value of 1 nm is in excellent agreement with the STM observation. Before defects start to coalesce (L_D>6 nm), a simplified model can be used to used, i.e. $I_D/I_G \propto 1/L_D^2$ [84]. The model described by equation 3.4, however, is able to predict L_D for wider disorder level including the coalesce

case. It should be noted that the Tuinstra-Koenig relation, i.e. $I(D)/I(G) \propto C(\lambda)/L_a$, is still valid for estimating the one-dimensional crystallite size L_A, not point defect.

3.3 Defect scattering in graphene

Experimental work from Chen and *et al* [12] provided electrical characteristics of graphene devices with deliberately introduced vacancy-type defects complemented with Raman spectroscopy data. The graphene samples were irradiated using 500 eV Ne and He ions. The transport properties in such devices are dominated by scattering through mid-gap states, in which a point vacancy is modelled as a deep potential well of finite radius. The irradiation-induced defects give rise to a constant mobility but four times lower compared to charged impurities of same density. Irradiation also depressed minimum conductivity $\sigma_{(min)}$ significantly.

First they shown that ion irradiation induces a significant increase of the D peak in the Raman spectrum, which is also a direct result of inter-valley scattering, in which electron is scattered between two inequivalent Dirac cones due to the defect[85]. The authors first roughly estimated the defect spacing using empirical linear dependence of crystallite size L_a in disordered graphite by $L_a = 2.4{\times}10^{-10}\ \mathrm{nm}^{-3}\ \lambda^4 \left(\frac{I_D}{I_G}\right)^{-1}$ [84], where λ is the excitation wavelength. It indicates that L_a ~ 60 nm, which is larger than expected spacing of 10 nm, but close to the transport mean free path of ~50 nm.

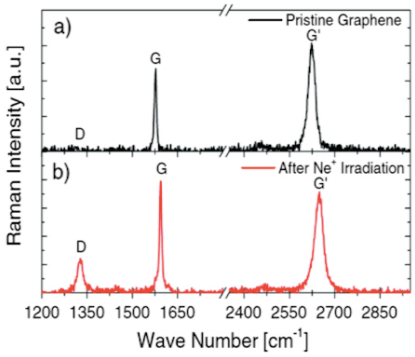

Figure 3.8 Raman spectrum showing the emergence of *D* peak after Ne^+ irradiation [12].

Transport-wise, three scattering sources were taken into account: charged impurities, lattice defects and weak point-disorder. The former two scattering types give rise to a constant mobility. Therefore the resistivity of irradiated graphene was modelled as a combination of two parts: a carrier density (n) dependent part and a density-independent

part: $\sigma^{-1} = [C_g (V_g - V_{g,min})\mu]^{-1} + \rho_s$, where μ is the mobility and ρ_s is the n-independent resistivity due to short-range weak point-disorder, both of which can be extracted from fitting the experimental results (Figure 3.9). Mobility μ is almost inversely proportional to irradiation dose while ρ_s does not vary much with irradiation, as can be seen from Figure 3.10. On the other hand, the independence of μ on n can be attributed to either charged impurities or midgap states. The authors claimed that midgap states are dominant based on the following observations. First, the transport mean free path l_{mfp} calculated for μ = 1300 $cm^2V^{-1}s^{-1}$ and $n \sim 10^{13} cm^{-2}$ is around 50nm, which corresponds well with La~60nm obtained from Raman spectroscopy, indicating a structural disorder. Second, if the reduced mobility were due to the creation of charged impurities, each incident helium or Ne^+ would have created 4 more charges. However the shift of $V_{g,min}$ indicates only <1 net charge per incident ion. Also accelerated helium and Ne^+ have very different momentum and should make a large discrepancy on added charges. Third, the observed $\sigma_{(min)}$ changes linearly with μ, indicating constant intrinsic carrier density n^*. Since n^* is a function of charge impurity density n_{imp}, n_{imp} is therefore nearly independent of irradiation.

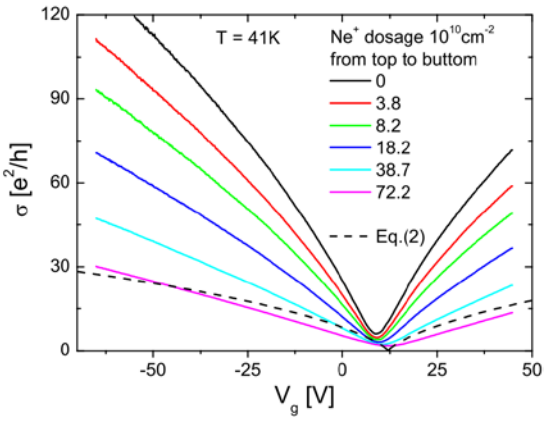

Figure 3.9 Conductivity as a function of V_g for different irradiation dose. The dashed line is calculated from an equation that only considers scattering by strong disorder [12].

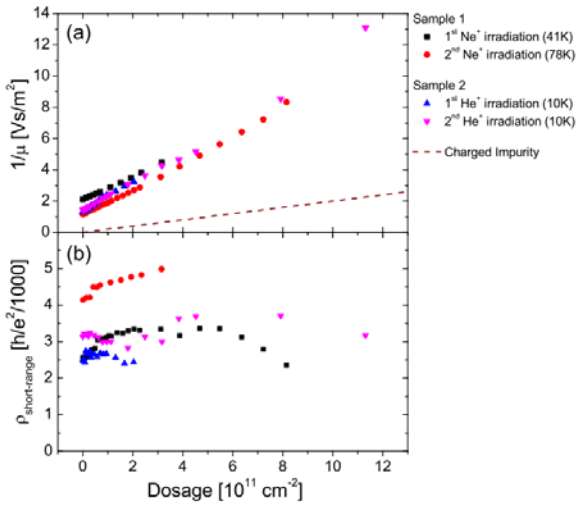

Figure 3.10 (a) Inverse of mobility versus irradiation dosage. Dashed line is the calcluated value for same concentration of charged impurities [12]. (b) ρ_s as a function of dosage.

Lastly the authors also discussed the effect of irradiation on the temperature (T) dependence of σ (Figure 3.11). In contrast to pristine graphene, in which σ is not sensitive to T in 4-100 K range, σ of irradiated graphene reduces towards insulating as $T \rightarrow 0$. However, the origin of this metal-insulator transition is not clearly understood. It is possibly due to weak localisation induced by intervalley scattering.

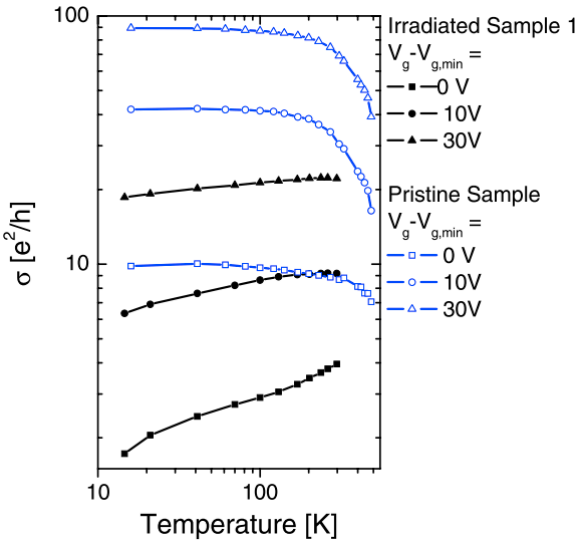

Figure 3.11 Conductivity as a function of temperature for pristine graphene (metallic) and irradiated graphene (semiconducting) [12].

3.4 Conduction tuning in defective graphene

The absence of a band-gap in pristine graphene hinders some applications from this wonder material such as logic electronics. Therefore it is highly desirable to achieve

electro-static conduction tuning via the modification methods such as irradiation or hydrogenation[86–95], chlorination[96,97], fluorination[98–102] and other surface chemistry[103–107]. Nakaharai *et al* [13] recently demonstrated an on-off ratio of two orders of magnitude by inducing carefully controlled defects into the graphene channel via ion irradiation. Although several modification methods exist, the embedded defects (i.e., point defects such as vacancies and Stone-Wales defect) are of great interest due to its stability both thermally and chemically. In this work, a suppression of current was observed by varying both V_g and V_d for samples with low density defects. The exponential length dependence of current indicates a transport regime governed by strong (Anderson) localisation.

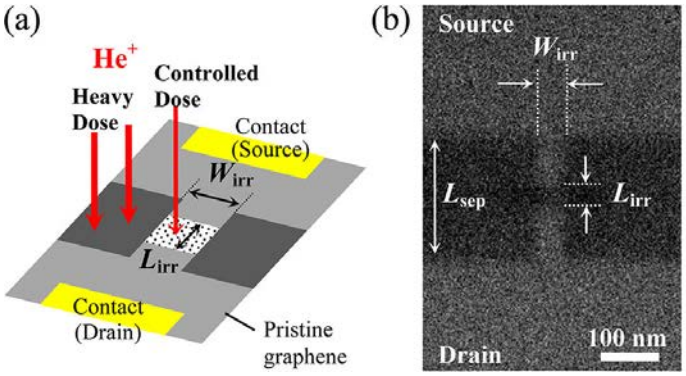

Figure 3.12 (a) device schematics showing the channel irradiated with controlled doses and the isolation area between contacts irradiated with heavy dose. (b) HIM image of the channel and its surrounding areas [13].

The device layout and fabrication process is shown in Figure 3.12. The graphene nanoribbon was first made using a standard e-beam based process. A rectangle with pre-defined length (L_{irr} = 30 nm) and width (W_{irr} = 50 nm) was then irradiated with varying doses from $1.3\times10^{15} cm^{-2}$ to $1.3\times10^{16} cm^{-2}$, which was referred to as 'channel'. The rest of the graphene within a separation length L_{sep} = 200 nm was irradiated with very high dose ($1.3\times10^{16}\ cm^{-2}$), which essentially make this part of the graphene amorphous and insulating.

The authors first studied the I_d-V_d trend as a function of defect density of a set of devices (Figure 3.13 (a-b)). It was found that at room temperature I_D decreases exponentially with defect density indicating a metal-insulator transition (Figure 3.13(c)). The Raman spectrum shown that although the hexagonal lattice structure of graphene is largely reserved after the irradiation (large G peak), the D peak does increase with irradiation indicating the existence of structural defects (Figure 3.13(d)).

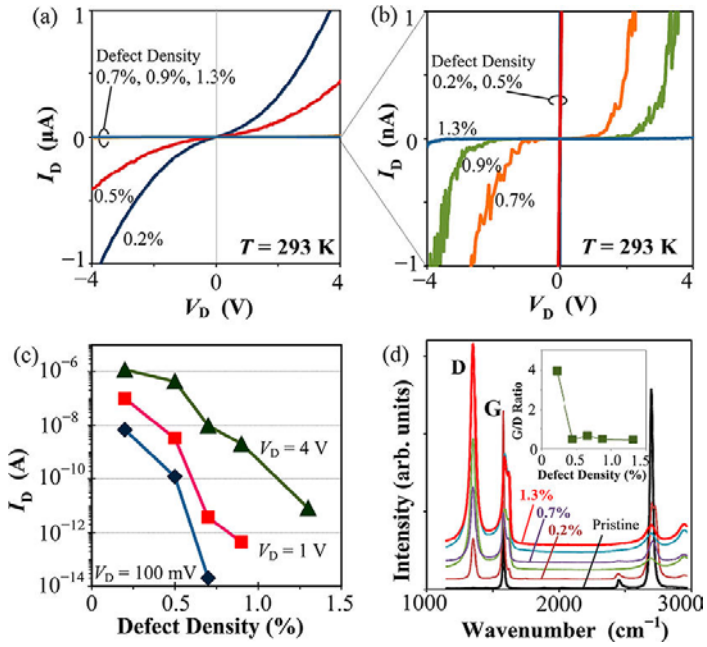

Figure 3.13 (a-b) I_d-V_d for devices with different defect densities (0.7%-1.3%) at 293 K. (c) Log-scale I_D as a function of defect density. (d) Raman spectra measured for different defect densities. Inset: *I(G)/I(D)* ratio v.s. defect density [13].

In addition to the defect-dependent current decay and non-linear I_d-V_d relation, a current suppression near the Dirac point was also observed showing a 2-orders-of-magnitude on-off ratio (Figure 3.14(a)). The logarithmic plot also shows large conductance drop at low bias voltage even at room temperature (Figure 3.14 (b)). This is in stark contrast to what is found in pristine graphene.

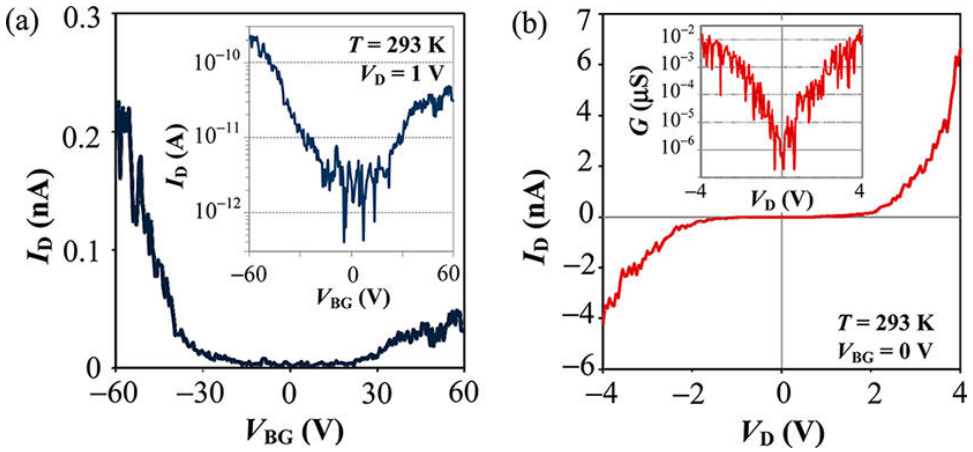

Figure 3.14 (a)I_D-V_{BG} measured at RT for 0.9% defect density. (b) I_d-V_d at RT for the same device [13].

The authors found that the carrier transport becomes more sensitive to temperature in devices with higher defect density. Furthermore, although the temperature dependence fits well with thermal activation model for defective samples, it starts to deviate to the

variable range hopping regime for more defective samples at lower temperature. This indicate a different mechanism is responsible for the transport in these samples, which was claimed to be strong localization by the authors.

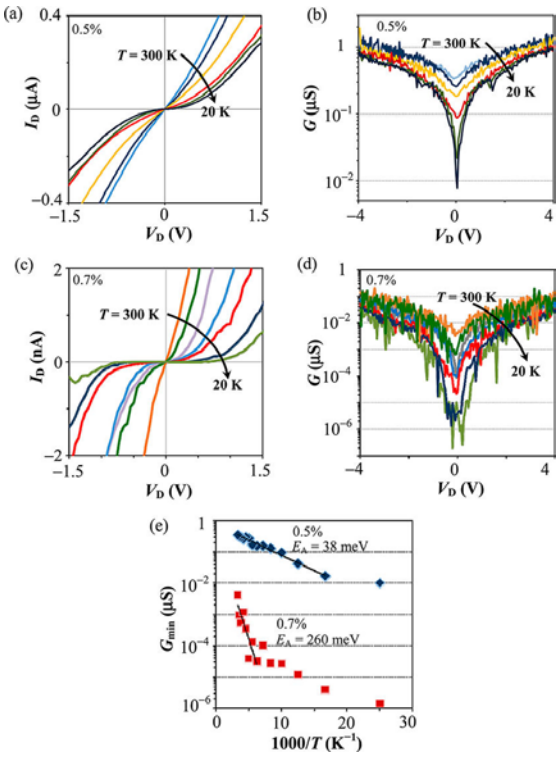

Figure 3.15(a,c)I_d-V_d from 300 K to 20 K for devices with defect density 0.5% and 0.7%, respectively. (b,d) differential conductance vs. V_d for devices with defect density 0.5% and 0.7%, respectively. (e) Minimum conductivity as a function of 1000/T for devices with defect density 0.5% (blue) and 0.7%(red) [13].

The argument was further proved by length dependent measurements (Figure 3.16). It was found that I_d decreases exponentially with L_{irr}, which is signature of strong localization. The current suppression can therefore be explained by the transport gap appearing near the Dirac point where localized states are isolated from each other due to low density of states. This fundamentally different from a previously suggested model [108] based on the band gap originated form the formation of Schottkey junctions between the irradiated region and pristine region.

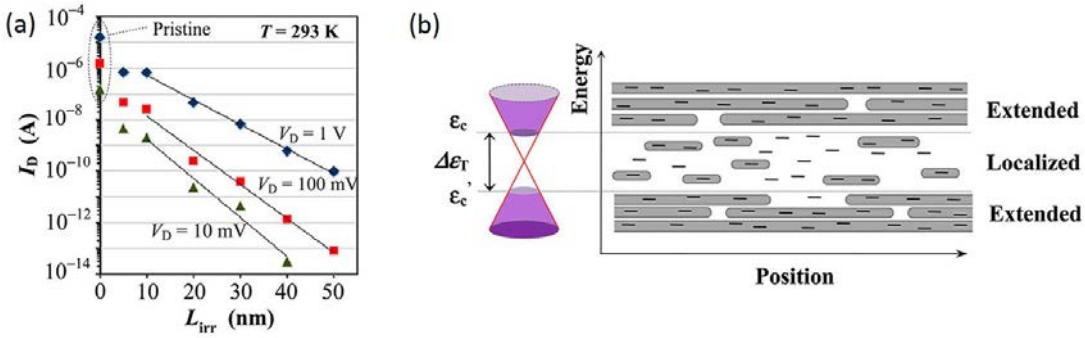

Figure 3.16 (a) log-scale I_D as a function of irradiation length. (b) the proposed scenario where an energy-gap is formed due to localized states [13].

3.5 Conclusions

In summary, four works related to defects in graphene are reviewed in this section including: formation and migration of point defects observed by HRTEM with atomic resolution[76], Raman spectroscopy of defective graphene where a phenomenological model was derived to determine defect density based on the non-monotonic change of I(D)/I(G)[72], scattering due to defects revealed by transport measurement (resistivity, mobility, etc.)indicating localization[12] and novel device facilitated by patterned irradiation showing metal-insulator-transition[13]. These works provide valuable information for the defect engineering of graphene, from fundamental physics to device fabrication. In particular, the experimental methodologies established in the reviewed works such as defect creation via ion irradiation, defect density determination via Raman spectrum and electrical measurement are adopted in this thesis to further study the beam damage caused by helium ion milling and led to the development of new devices with embedded defects created by helium ion beam technology, as presented in following chapters

.

Chapter 4 Device fabrication methods

4.1 Sample preparation

Most of the graphene flakes used in this thesis were produced by micro-mechanical exfoliation, i.e., peeling off from highly ordered pyrolytic graphite crystals using scotch tapes. Highly doped (resistivity of 0.001 Ω.cm – 0.01 Ω.cm) Si wafers (thickness ~ 525 μm) with 295 nm thermal oxide pre-patterned with chip marks and contact pads are selected substrates. The low resistivity Si layer serves as a back gate material for modulating the overall Fermi level of graphene.

In order to effectively locate the randomly positioned graphene flakes and for the integration of further lithography steps, metal chip marks are first deposited on the bare substrates. A two-level alignment scheme is required for e-beam lithography with accuracy of ~ ±10 nm (Figure 4.1). A pair of 'P' and 'Q' marks and four 'chip pal's are needed to write the pattern files in any one position on the chip, if high alignment accuracy is required. The use of only P, Q marks can still provide the accuracy of ~±200 nm. Both P, Q marks and chip pals are defined in one EBL step along with all the 'mini' contact pads for minimal misalignment. A thin layer of Au (~30 nm) is used for the alignment marks (in addition to adhesion layer ~10 nm Ti) because of its high contrast to the insulating SiO_2 under SEM, which is essential for the mark detection in EBL. A standard 'lift-off' process is used for the metallisation. Nine of the deposited alignment marks (chip-pals) are shown in Figure 4.2 (a).

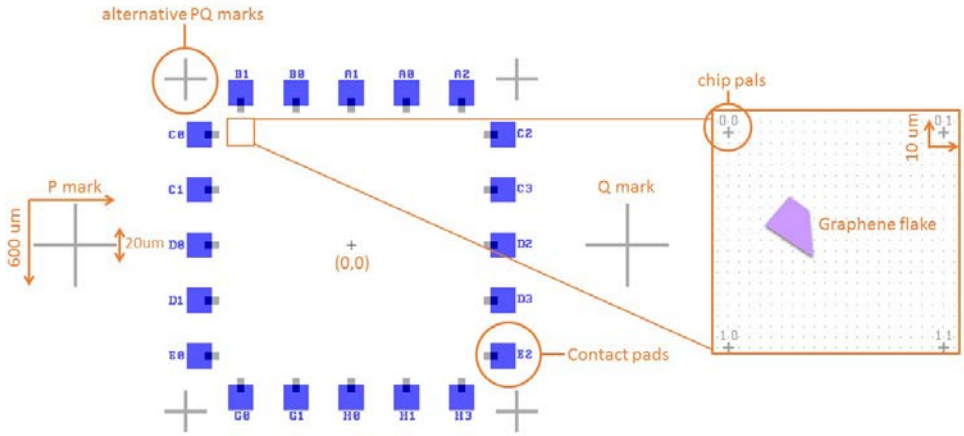

Figure 4.1 Our chip layout showing the two-level alignment regime. Major PQ and alternative PQ marks for coarse alignment are shown in grey colour. Twenty contact pads are shown in blue colour. The blow-up view of an area containing four chip-pals around a graphene flake is shown on the right hand side

Following the deposition of alignment marks, twenty major contact pads are written using a second EBL step and deposited by evaporation (Figure 4.2(b)). The thickness of the pads is much higher (300nm Au) compared to alignment marks to improve yield of wire-bonding. A layer of 'S1813' photo-resist was spun onto surface of the processed wafer before dicing it into 5×5 cm^2 chips from the back-side. Four grooves of 150 µm in depth were carved at the back-side for further clipping to smaller size that fits sample holders as in AFM and cryostats, etc. (Figure 4.2(c))

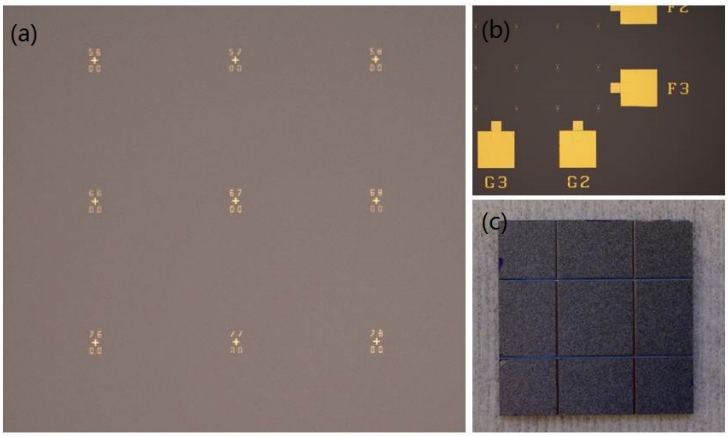

Figure 4.2 (a) Optial image of the chip showing the 'chip-pal's. The distance between the chip marks is 200 µm. (b) Deposited contact pads with the thickness of 315 nm/10 nm Au/Ti. (c) the backside of the chip showing the grooves for clipping.

Prior to the exfoliation, plain chips are immersed in Acetone and IPA each for 5 minutes, followed by 10 minutes' ozone-clean. The flakes are transferred from the tapes directly

onto the SiO_2 surface. The density of undesired graphite can be reduced substantially by 1 minute sonication in IPA. The number of graphene layers can be identified based on its optical contrast (shown in Figure 4.3 and Figure 4.4). The green channel grey scale image is extracted. An area that contains both graphene and substrate is used to obtain the histogram where the two major peaks can be found to represent single- or multi-layer graphene and substrate. If the peak position for the substrate is set at 100% (i.e., normalised), the peak position for single layer graphene, bilayer graphene and trilayer graphene are ~94%, ~88% and ~81%, respectively (see Table 4-1). This optical method can be used in combination with Raman spectroscopy to ensure the number of graphene layers. The latter is widely used as an non-invasive method for examining the thickness and quality of the graphene flakes [79] (Figure 4.5).

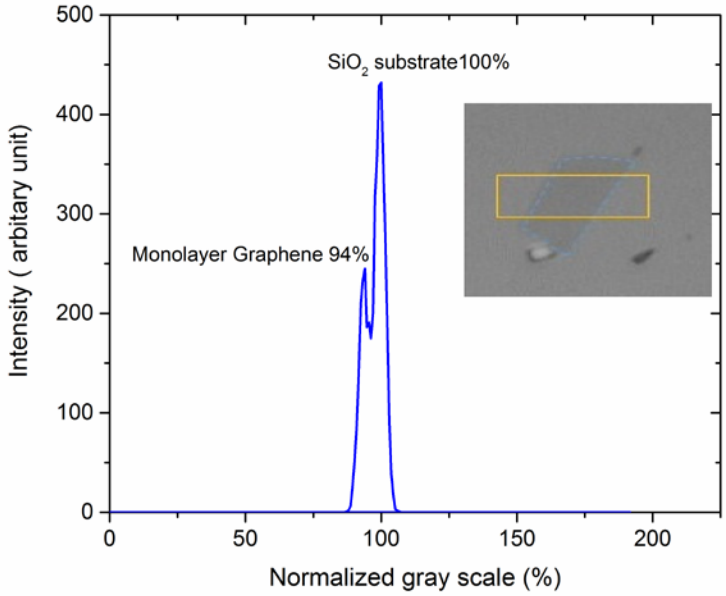

Figure 4.3 Normalised histogram of a grey scale image (green channel) of a graphene flake(outlined by blue dashed line in the inset). The grey scale of the SiO_2 is set at 100%. The 94% grey scale value indicates single layer graphene.

Table 4-1 Graphene-to-substrate optical intensity ratios for different number of layers

Number of layers	0 (SiO_2 substrate)	1	2	3	4
Intensity ratio (%)	100	~94	~88	~81	~75

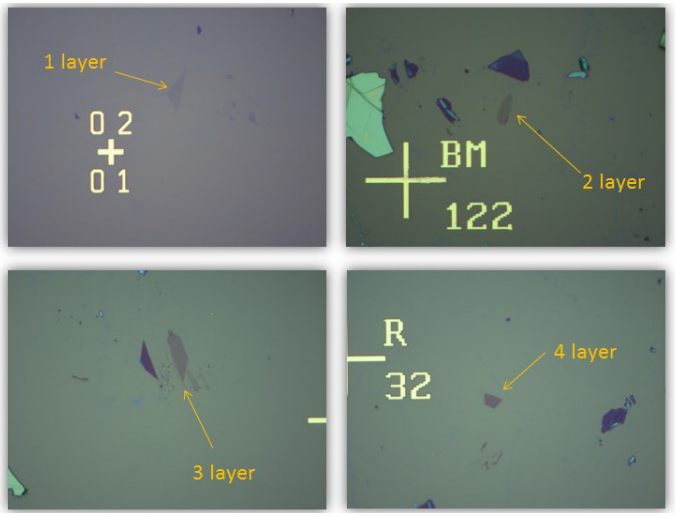

Figure 4.4 Optical images of 1, 2, 3 and 4 graphene layers

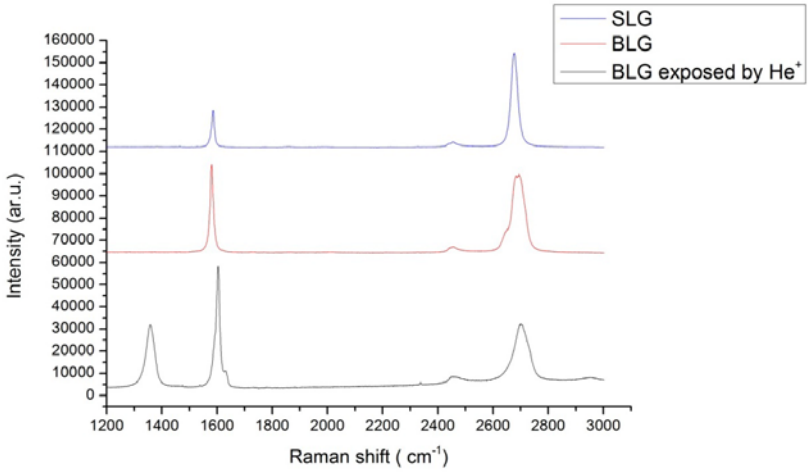

Figure 4.5 The Raman spectrum of three types of graphene shifted by constant level for clarity. The blue line is the spectrum of a single layer of graphene showing a very sharp peak at ~ 2700 cm^{-1}. The red line is the spectrum for bilayer graphene. The black line is the spectrum for a same bilayer graphene after irradiation of helium ions. The peak at the leftmost is the D peak which indicates the defects.

To locate target flakes for accurate alignment in lithographic tool, the optical images (1280×960 pixels) are imported in AutoCAD for translational and rotational adjustment. The coordinate information of the polygon that outlines the flake is converted into correct unit (micron) and thus can be used directly in layout software such as L-edit®. We developed a small Windows application that automates the generation of 'jdf' and 'sdf' files for the JEOL EBL system (Figure 4.6). The tool not only speeds up the design flow,

but also reduces the chance of error during the manual file conversion, given each randomly located graphene flake needs a completely different set of coordinates and chip marks.

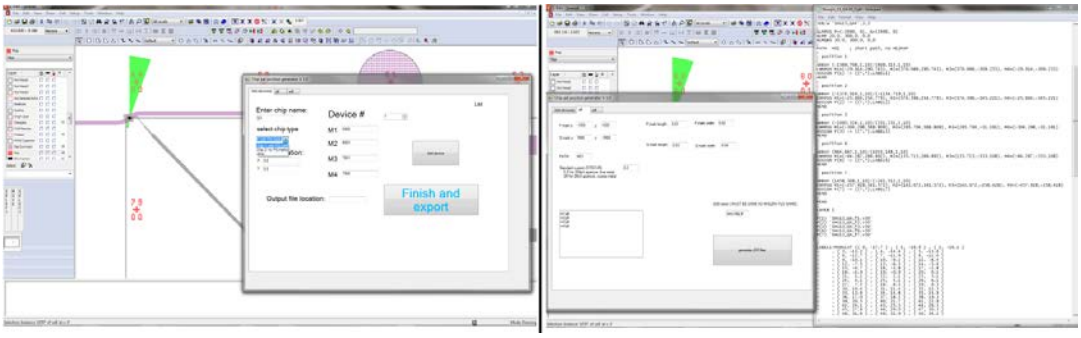

Figure 4.6 A home-brew Windows® application that takes pre-programmed chip information to calculate the chip mark positions and generates JDF files for JEOL E-beam system. Left: import of device position and chip mark numbers. Right: import of 'jdi' proximity correction files and generation of final jdf file.

4.2 E-beam based fabrication process of graphene devices

4.2.1 Introduction

Due to the tininess and randomness of graphene obtained from exfoliation, large-scale patterning with pre-designed photo-lithography mask is not a practical option for our devices. Neither can the optical photo-lithography provide the necessary resolution and feature size for our down-scaled graphene devices. As a result, the electron-beam-lithography is mainly used for defining all the layers including isolation, metallisation, top-gate and etc. The e-beam exposure was performed using a state-of-the-art JEOL 9300FS e-beam lithography system under the acceleration voltage of 100keV.

4.2.2 Lithography: mask design considerations

A set of combinations of aperture size, beam current and acceleration voltage (fixed at 100 kV) are used at the Southampton Nanofabrication centre to accommodate different feature requirements. It is the beam spot size (4 nm in our case) that dictates the resolution. One must ensure in his layout design that the minimum linewidth must be an integer multiple of the beam spot size to achieve the most accurate control on the exposure. For example, there is no difference between designing a 13 nm and 15 nm track since only

12nm wide area will be exposed if the spot size is 4 nm. One can always round up the number to prevent underexposure. The dose required for exposing a particular resist of certain thickness a more or less fixed, the exposure speed thus solely depends on the beam current. It is usually a good practice to maximise the beam current when only little comprise is introduced to the resolution to minimise the writing time.

Choosing the right thickness of resist is important to get the right feature size. A rule of thumb is resist thickness (t_{resist}) is less than or equal to the minimum feature size, although infinitely thinning the resist thickness is not practical due to the intrinsic spin curve of the resist. On the other hand, the bilayer lift-off for metallisation usually requires that $t_{resist} \geq 2\times$ metal thickness (t_{metal}) for the bottom layer.

4.2.3 Fabrication process: etching and metallisation

To pattern GNR structures on graphene flakes, a thin layer of diluted poly(methyl methacrylate) (PMMA) 495 K (i.e., molecular weight = 495) is used. Here, PMMA 495 K A4 is diluted with Anisole (1:1) in order to get sufficiently small thickness of around 42nm which is comparable with the minimum feature in our design (aspect ratio of ~ 1:1). The samples were then exposed using 200 pA-60 μm beam condition, that is, 200 pA beam current and 60 μm aperture size. The acceleration voltage in our e-beam system is always kept at 100 kV. The exposed samples were developed in a 50:50 methyl isobutyl ketone (MIBK): isopropyl alcohol (IPA) mixture. The masked graphene flake was then etched with O_2/Ar (4:1) plasma generated in a reactive ion etching tool (RIE). The resist was removed in NMP or Acetone. To place metal contacts on the patterned graphene flakes, a top layer of methyl methacrylate (MMA) is used. The MMA/PMMA (230 nm/117 nm) bilayer resist facilitates an undercut structure for lift-off. A second e-beam exposure using the beam condition of 25 nA-330 μm. Ti/Au (7 nm/73 nm) was deposited using a Leybold LAB700EB Evaporator, which was followed by a lift-off process in warm N-Methyl-2-pyrrolidone (NMP) at 70 ^{o}C.

4.2.4 Top-gate deposition

For bilayer graphene (BLG) and multilayer graphene (MLG), the use of a sole back-gate cannot efficiently open a band gap due to interlayer screening[109–113]. Therefore, a top-gate is usually desired to generate perpendicular electric field to open a wide band

gap in BLG and MLG. The main challenge for depositing AlO_x top-gate on graphene is the lack of dangling bonds on pristine graphene surface for ALD or CVD process. Several methods were developed to circumvent this issue based on the introduction of seed layers[114,115]. We employed relatively simple method developed by Tsukagoshi group [116,117]. Here the top gate is formed by PVD of 30 nm Al directly on graphene. The sample is exposed to air for 24 hours. A layer of natural oxidized AlO_x (~3 nm) is formed at the Al-graphene interface. An as fabricated device is shown in Figure 4.7 where the graphene channel is 1μm wide and 5μm long, while the top-gate (TG) is 3.6 μm wide (see Figure 4.8).

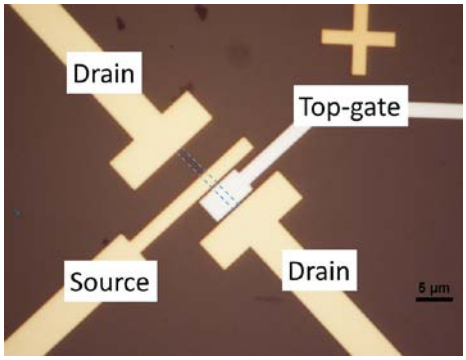

Figure 4.7 A pair of GNR devices, one of which is covered by a AlO_x top-gate. The blue dashed lines outline the graphene channel

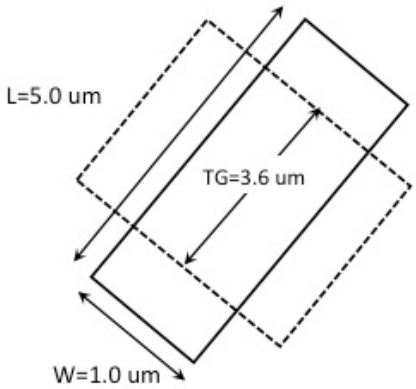

Figure 4.8 Dimension of device 3. Dashed rectangle outlines the GNR and solid rectangle is the top-gate.

The top-gate leakage current is very small (tens of fA) which is one order of magnitude less than the measured back-gate leakage current, indicating formation of high-quality AlO_x. Figure 4.9 shows such the conductance (G) measured as a function of top-gate voltage (V_{TG}) at different temperature from 5-198 k. The asymmetric electron and hole conductance was not found for the range of V_{TG} applied, as opposed to back-gate case. In addition, the neutrality point is close to 0 V. This is attributed to the fact that the top-gate

serves as a passivation layer that protects the graphene from ambient doping and improves the stability of the device.

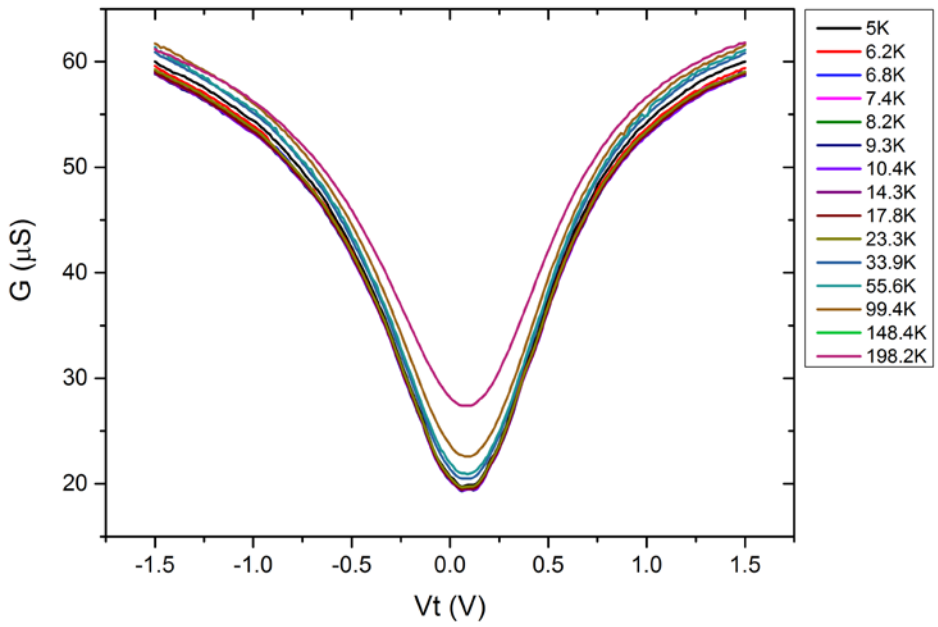

Figure 4.9 Conductance as a function of top-gate voltage from 5 K-198 K

Although the top-gate configuration has not been employed in the main works discussed in following chapters, the successful fabrication of top-gated graphene device not only offered electrical comparisons with the back-gate configuration, but also provided alternative ideas for further device integration.

4.2.5 Electrostatic control via side-gates

In addition to back-gate and top-gate, side-gates in close proximity of the channel (several tens of nanometres) can also provide good electrostatic control on the electron flows. For instance, Molitor *et al* [118] demonstrated the tuning of conductance by both side-gate and back-gate on a graphene constriction structure (width = 65 nm) and showed that increasing side-gate voltage can reduce the transport gap of the device. Moreover, the side-gate configuration has been extensively used in graphene quantum dots devices to access single electron regime [25,26,119]. We fabricated graphene nanoribbon devices with two-side gates and slightly irradiated 'barriers'.

Figure 4.10 shows the schematic of our device. The GNR was fabricated by etching the EBL-defined pattern into exfoliated graphene. Both channel width and gate-to-channel distance are 50 nm. The main ribbon is 400 nm wide. Tunnel barriers were formed by irradiating 5 nm strips on the GNR by helium ions with an equivalent defect density of ~8×10^{12} cm^{-2} as estimated from Raman spectrum. By patterning two barriers with close proximity, a quantum dot structure can be effectively created. Two side gates (SG) are responsible for controlling the potential in the barriers one plunger gate (PG) tunes the central island. It should be noted that when zooming at high magnification in a HIM (~80,000), imaging dose is comparable with patterning dose. Therefore, it is crucial to mask the GNR to avoid any undesired exposure. The masking can be done by using ebeam resist such as PMMA (see section 6.6) or by reducing the imaging/patterning window so that the graphene channel is not exposed. This latter method is illustrated in Figure 4.11: the graphene channel is located by tracking the metal electrodes; a strip pattern is inserted to the target position (horizontally in between two top electrodes and vertically aligned with two side electrodes) for patterning.

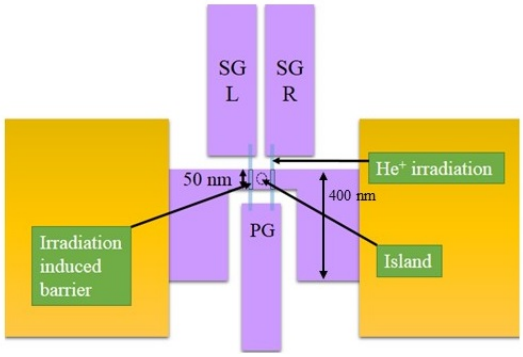

Figure 4.10 Schematics of our device. Single quantum dot is confined by two strips (blue) of insulating area made by ion irradiation.

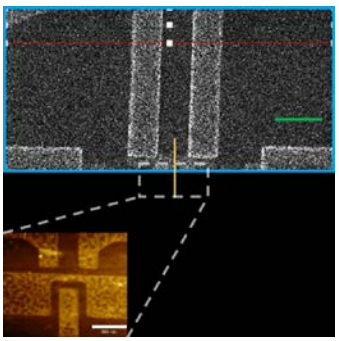

Figure 4.11 HIM irradiation of 5 nm strip in the channel (yellow vertical line). The graphene channel is masked by the imaging window outlined by the blue frame. The green scale bar in the HIM image (upper) is 1 μm. The inset shows

the AFM image of the device channel that corresponds to the dashed rectangle in the HIM image. The white scale bar is 300 nm.

We measured room temperature conductance after one 5nm strip was irradiated in the GNR channel (see Figure 4.11). The contour plot of conductance as a function of V_{BG} and V_{SG} is shown in Figure 4.12. The contour plot of conductance as a function of V_{BG} and V_{PG} is shown in Figure 4.14. In the former case, two side gates are electrically connected, i.e. $V_{SG\,(L)} = V_{SG(R)}$. Two distinct slopes (the trajectory of charge neutrality point (CNP)) can be observed, from which the gate capacitance can be observed outlining four different potential configurations: *p-n, p-p, n-n and n-p*. The side gate capacitances can be estimated from the diagonal slope (thick dashed line), $C_{SG} = C_{BG}(\frac{\Delta V_{SG}}{\Delta V_{BG}})^{-1} \approx 72nF$. Similarly, $C_{PG} \approx 60nF$. Another notable feature is the unipolar transport at *p-n* regime. The conductance versus V_{SG} and V_{PG} at different V_{BG} levels are plotted in Figure 4.13 and Figure 4.15, respectively. For each V_{BG} level, the data for five V_{BG} values near that level (±0.5 V) are plotted to enhance the visibility of the originally noisy data. At high $V_{BG,}$ the bipolar conductance behavior is dominant (green data lines in Figure 4.13 and Figure 4.15). As V_{BG} reduces, the conductance due to electrons decreases and eventually a unipolar behaviour appears (black data lines in Figure 4.13 and Figure 4.15). This attributed to that when V_{BG} and $V_{SG,}$ V_{PG} are of different polarity, p-n and n-p regions form and increased the width of conductance minimum. However, the role of irradiation played here is yet clear at this point. Higher dose may be needed for more observable change.

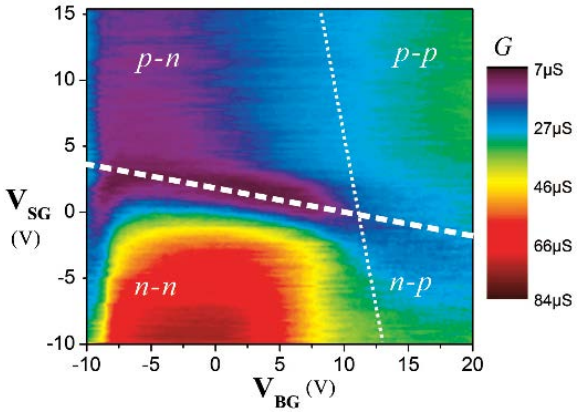

Figure 4.12 Contour plot of the source-drain conductance as a function of V_{SG} and V_{BG}. White dashed lines indicate CNPs for the bare (thin) and SG-controlled (thick) region

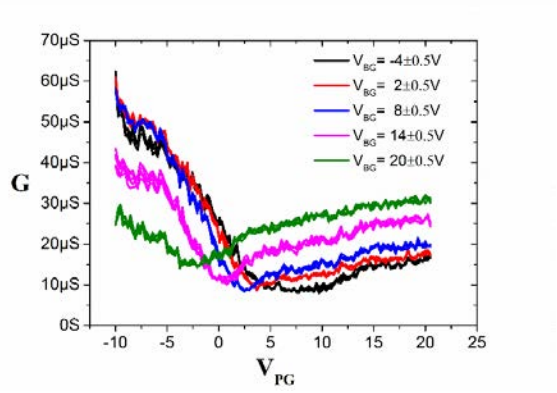

Figure 4.13 Conductance as a function of V_{SG} for V_{BG} = -8, -4, 0, 4 and 8 V. Unipolar transport can be observed from the black line.

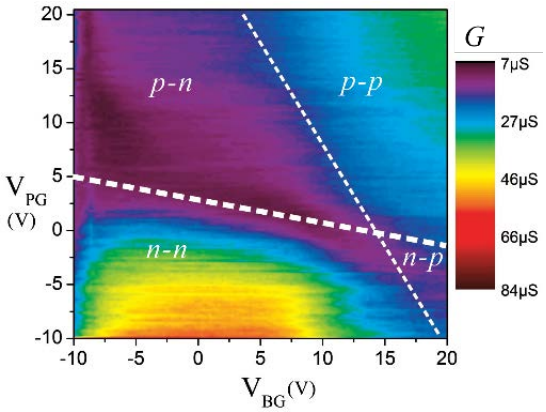

Figure 4.14 Contour plot of the source-drain conductance as a function of V_{SG} and V_{BG}. White dashed lines indicate the CNPs for the bare (thin) and PG-controlled (thick) regions.

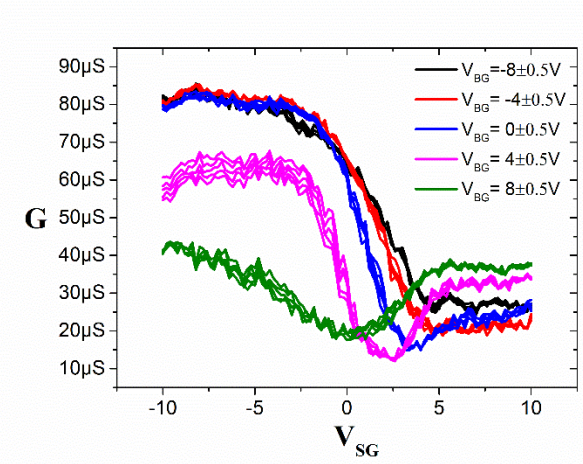

Figure 4.15 Conductance as a function of V_{SG} for V_{BG} = -4, 2, 8, 14 and 20 V

4.3 HIM-based fabrication techniques

4.3.1 Introduction

After the definition of GNR devices, the desired amount of defects needs to be embedded. Ion irradiation is our primary method due to its simplicity. The irradiation is taking place in a helium ion microscope (HIM), which is made commercially available since 2007 [120]. In this chapter we first discuss two major applications of HIM technology: metrology and direct milling as well as how they are employed in our experiments of defect engineering on graphene devices.

4.3.2 HIM microscopy

The instrument for generating the helium ion beam is a Zeiss® *Orion Plus* Helium Ion Microscope. The HIM based on a technology called 'gas field ionization source' (GFIS) has several unique features that makes it advantageous to the established scanning electron microscopy (SEM).

The atomically sharpened ion source in the HIM gives rise to high brightness. The ion source is made of tungsten and is cryogenically cooled (75 K). The emitting process resembles that used in a field ion microscope (FIM) [121] and is briefly described as follows. When biased at the extraction voltage, the electric field is very high at the sharpest curvatures (~3 V/Å). The nearby helium gas atoms are attracted towards these protrusions due to a polarisation effect. Once the gas atom crosses the 'ionisation disc' (an ionisation region with a disc shape of few Å in diameter and ~2.5 Å in thickness), they are ionised and the resulting positive ions are accelerated back by the electric field. The ionisation source in the HIM is further improved from a FIM in that its shape is pre-defined as a pyramid so that only the few atoms at the top of the pyramid are capable of emission (see Figure 4.16). The end result is bright source with high beam current ($\sim 1.4\times10^{19}$ A/cm^{2}sr). The pyramid structure can be removed or reconstructed by increasing the electric field to 5 V/Å (30 kV) in which tungsten atoms are field evaporated. A stable configuration which is most frequently used is a three-atom tip ('trimmer'). The tip is sharpened atom by atom until a relatively stable three-atom configuration is achieved.

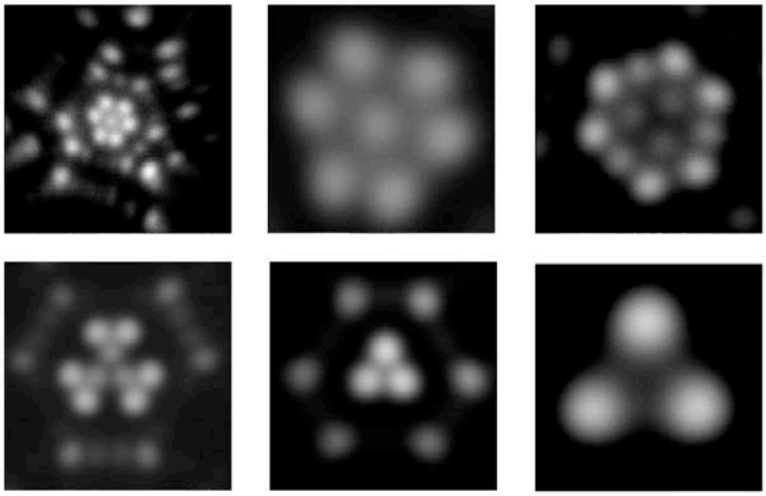

Figure 4.16 Tip formation process in HIM illustrated by Posetec *et al* [120]

From the physical principle, the resolution of SEM is limited by large interaction volume and diffraction of electron beam. On the other hand, the helium ion beam has a shorter *de* Broglie wavelength and therefore small apertures can be used leading to negligible diffraction effect. As a result, the HIM has a sub-nm probe size.

However, in order to achieve high resolution, having a small probe size is just half of the story. It is the interaction volume that determines the achievable resolution of the beam. This is evident in the case of 30 kV gallium beam (a typical set-up in a FIB), where the probe size is ~5 nm but the excitation volume can extend far beyond the probe size resulting in a much larger resolution. This is because the heavy gallium ion generates large number of recoils inside the sample which in turn excites many more secondary electrons (SE) that are able to escape the surface. Similarly, incident electrons in a SEM get backscattered near the surface producing additional SE, which makes resolution worse. By contrast, the helium ion beam penetrates much deeper into the sample and does not cause large number of recoils because of its lightness. In other words, the helium ion beam does not spread much near the surface. A much smaller interaction volume of the helium ion beam means that the only SE collected by the detector come from a very small area near the incident point, which contributes to the improved resolution of HIM.

The yield of SE of helium ion beam is also greater than an electron beam under same beam energy. In a SEM, the SE yield is usually limited to 1 per electron to prevent sample charging, while in a HIM, the issue charging is improved since the positively charged helium ions stopped deep inside the sample and are easier to be neutralized. As a result, the effective generation of SE in HIM (2-8 SE per incident ion depending on substrate

type) allows for operation at current below 1 pA and results in better signal-to-noise-ratio. In addition, the focused helium ion beam has a narrow convergence angle which increases the depth-of-field, hence improving image quality.

Different micrographs can be formed in a HIM depending on the particles collected by the scintillator, being SE or backscattered ions (BI). The Everhart Thornley detector in the HIM detects the SE and forms images containing mainly the surface information of the sample. This is the most commonly used detector due to the high yield of SE. A microchannel plate (MCP) detector can be added to the instrument for probing BI. Images formed by ions is very useful in visualising material contrast because the scattering cross-section is a function of nuclei size. Figure 4.17 shows HIM images taken with the two different detectors.

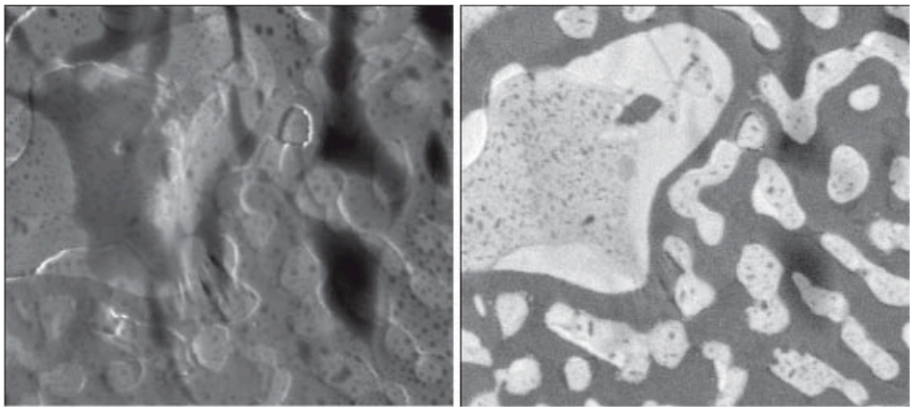

Figure 4.17 HIM images using different detectors by Morgan *et al*[122]. Left: SE image showing mainly topography information. Right: BI image showing material contrast: Pb(bright) and Sn (dark)

Here we briefly discuss the HIM imaging procedure and some considerations. Before moving the beam to any graphene-on-SiO_2 sample, it is always a good practice to tune the beam condition of HIM on a testing sample first (e.g. Sn on C (Figure 4.18)). Firstly, the extractor voltage is set to the best image voltage (BIV), which essentially maximizes the ion emission from the source. Secondly, a desired aperture is selected (5, 10 or 20 μm). The beam is properly tilted to centre the trimmer, maximizing the brightness. Thirdly, the beam must be aligned so that any observable wobbling and stigmation are eliminated. Fourthly, the working distance is adjusted to focus the beam at the surface. Finally, the dwell time and averaging can be increased to improve the image quality. Figure 4.18(a) shows a HIM image of Sn-on-C sample for calibration purpose, where the sharp edge of the Sn nanospheres can be clearly seen indicating good beam condition.

Figure 4.18(b) shows a HIM image of gold deposition using the same beam as in (a). Moreover, our system is equipped with a flood gun that floods the imaging area with low-energy electrons to neutralize the positive charging of helium ions (Figure 4.19) to avoid darkening.

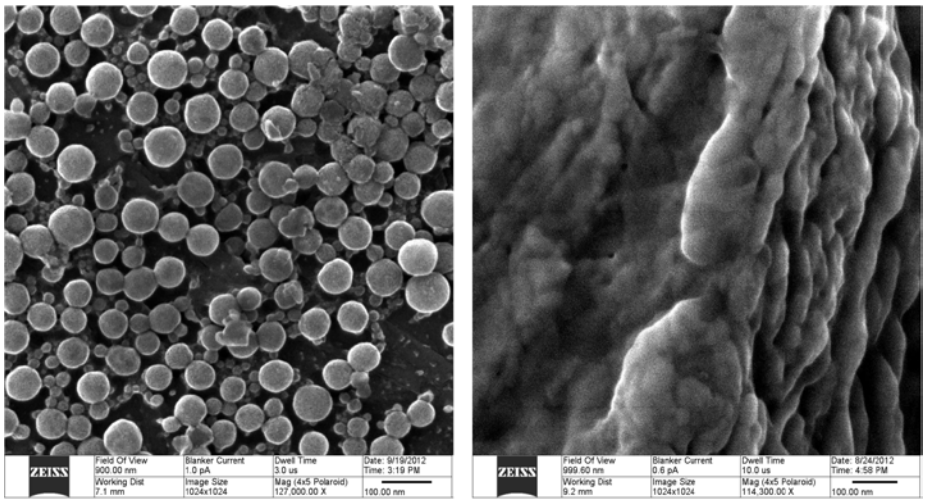

Figure 4.18 HIM image of Sn on C (left) and gold (right)

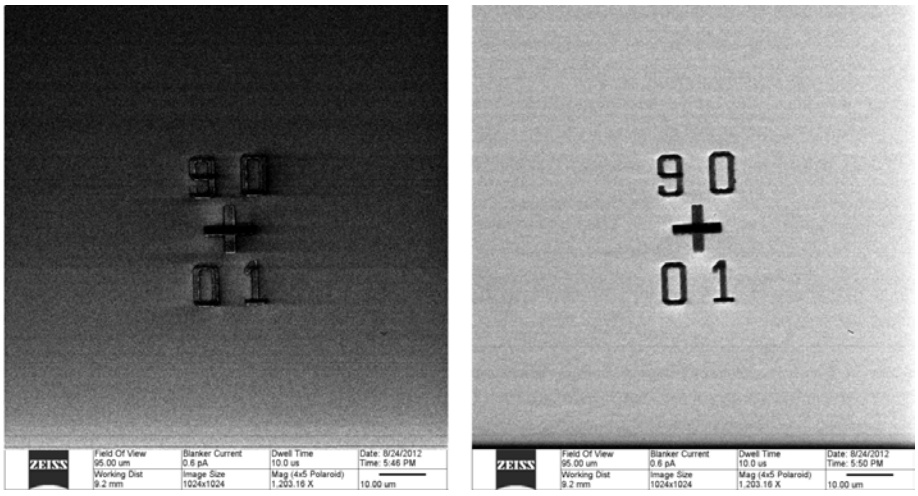

Figure 4.19 HIM image of an meatal alignment mark (Au) on SiO_2 substrate without floodgun (left) and with flood gun (right).

4.3.3 HIM milling

The intrinsic properties of graphene strongly depend on its geometry owing to its unique 2D nature. One notable example is the band-gap engineering on graphene nanoribbons

(GNR). Han *et al* [123] found that the conductance of a lithographically defined GNR scales linearly with the ribbon width. An inactive GNR width was speculated at around 5nm, below which conductance vanishes. It has also been found that the energy gap is inversely proportional to the ribbon width. Furthermore, lithographically defined quantum dots (QD) are effective platforms for transport single spins, an essential requirement for building electron spin quantum bit (qubit)[8]. An idea spin qubit platform for quantum computing should meet the DiVincenzo criteria, i.e. initialization, one- and two-quit operations, long coherence time and readout[124]. The electron spin qubit has been demonstrated in other materials such as GaAs[125,126] and Si[127]. Graphene, like other carbon-based system, is a prominent candidate for a spin qubit thanks to weak spin-orbit and hyperfine interactions[8,128]. The graphene QD devices have recently been experimentally reported by two major fabrication methods: 1) lithographically-defined, i.e. etching the EBL-patterned QD structure onto graphene[22,23,25,26,129–132] and 2) electrostatically-defined QD by top-gates[133].

In spite of the recent rapid development in these fields, these applications face the problem of downscaling beyond conventional e-beam lithography (EBL). The desired QD dimension can be estimated as follows. The dot charging energy (i.e. the energy required to transfer one elementary charge to the QD) is given by $E_c = \frac{e^2}{2C_{dot}}$, where e is the elementary charge and C is the capacitance of the dot and can be approximated by the plate capacitance $C_{dot} = 8\varepsilon_0\varepsilon_r R_{dot}$, where ε_0 and ε_r are the vacuum permittivity and relative permittivity, respectively[134–138]. R_{dot} is the QD radius. An ideal QD should be small enough so that the charging energy is greater than the thermal fluctuation, i.e. $E_c > k_B T$, where k_B is the Boltzmann constant and T is temperature. If we use $\varepsilon_r = 2.4$ for graphene and T = 300 K (room temperature). R_{dot} needs to be less than ~18 nm. Almost all the graphene QD or DQD structures reported so far are larger than this value, although R_{dot} ~50 nm have been achieved[22,23,25,26,129–132].

The feature dimension defined by EBL is usually limited by the resist uniformity and proximity effect. As mentioned in section 4.2.3, the etching of isolation patterns on graphene is usually followed by a lift-off process for contact formation. The patterning needs to be done before the lift-off because a thin layer of uniform PMMA is usually desired for defining fine nanostructures such as QD (~50 nm). For instance, a typical double quantum dot (DQD) device [130] may have seven electrodes including source,

drain and five side gates. If the metal tracks (~100 nm in thickness) were deposited first, the next layer of PMMA (~50 nm) for defining the DQD may not be uniformly spread onto the chip due to the thick metal tracks, resulting a poorly defined DQD structure after the EBL. However, depositing metal after the isolation of DQD is also problematic as the resist spinning on top of the fine structures could completely destroy the DQD in the middle area of the atomic thin graphene flake due to high molecular weight of the resist itself (247500 for 50% diluted PMMA 495). This is the case in Figure 4.20 where a pair of quantum dots is completely destroyed after the metal lift-off.

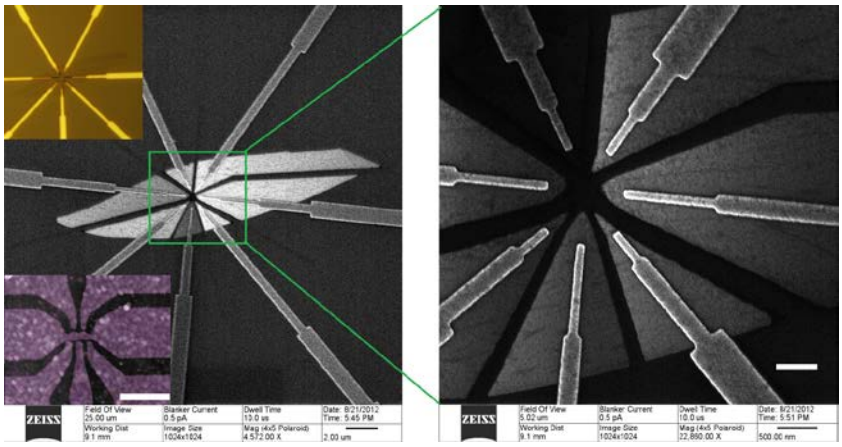

Figure 4.20 HIM image of a DQD device. The central area was destroyed after the metal deposition. Inset (upper) is the optical image of the device. Inset (lower) is the AFM image of the DQD before metal deposition.

Various approaches have been explored for downscaling, which can be categorized as 1) bottom-up and 2) top-down. In the former case, 1-D device such as extremely thin GNR with well-defined edges and widths are synthesized chemically, but a follow-up step is usually needed to selectively transfer the good GNR to the desired substrate[139,140]. On the other hand, the top-down methods aggressively reduces the feature size by direct writing involving electron/ion bombardment[32,35,36,141,142]. One can increase the particle's momentum (reducing wavelength) either by accelerating the particle or using a different particle to reduce the particle wavelength thus achieving high resolution. Sub-1nm resolution has previously been demonstrated by accelerating electrons at 200 kV in a transmission electron microscope (TEM)[36]. An alternative approach is using a tightly focused helium ion beams accelerated at 30kV[35]. In both cases, GNR of ~5 nm were fabricated. In fact, almost any pattern with achievable size can be carved using this direct-writing technology showing the main advantage of the top-down methods[142]. An early study by Pickard *et al* [141] in 2009 demonstrated the direct writing of nanoribbons down

to 5nm in width (aspect ratio 60:1) on suspended graphene using a helium ion beam. Recently (2013), Vicarelli *et al* [143] achieved 2 nm suspended GNR with atomically defined edges using accelerated electrons (30 kV) in a TEM (see Figure 4.21).

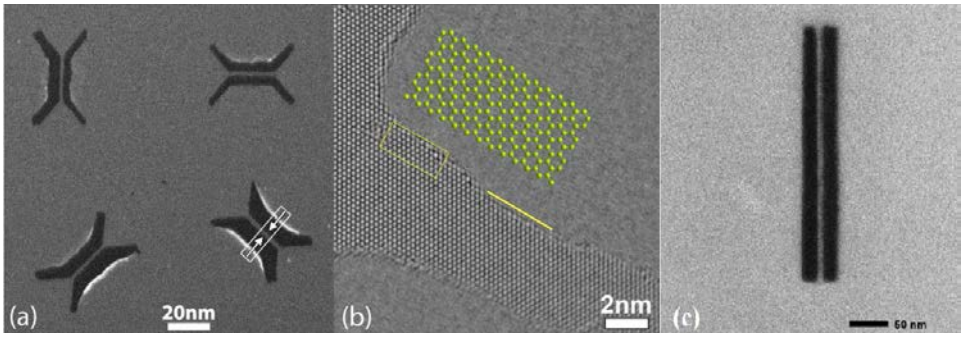

Figure 4.21 (a) TEM image of four GNRs produced by STEM (b) High resolution TEM image of one GNR made by TEM showing a well-defined Zig-Zag edge in the middle. (c) A 5 nm GNR made by helium beam milling

Although the above-mentioned works have shown very promising results in terms of lithographic advancement, little electrical characterisation has been done on devices made in this manner. This is mainly due to the fabrication complexity and vulnerability of graphene devices. Furthermore, the damage induced by ion sputtering on graphene is yet clear. Here we extensively investigated the direct helium ion milling technology using the HIM, which was first demonstrated in reference [141], but with more complex structures and most importantly, we implemented a hybrid EBL-HIM fabrication method that allows nano-machining at device level, allowing electrical measurement.

Since the helium ion beam shares same principle as any other focused ion beams, it should be beneficial to learn from what has been established in the FIB technology. In other words, what can be done in FIB can readily be applied with a HIM, such as milling [29,30,32,35], deposition [34] and resist exposure [144]. Notably, it has been demonstrated that the thinning of a TEM lamella by HIM results in significantly less crystal damage and contamination compared to FIB[145]. Since milling and sputtering is our main focus here, we will discuss some basic principles and considerations.

First the helium ion beam needs to be properly adjusted as described in section 4.3.2. The milling process we are using resembles the FIB process, i.e. a combination of current (I), dwell time ($\boldsymbol{\tau}$), pixel spacing (Δd) and number of repetitions (N_{rep}). The relationship of these parameters to the total writing time is given below:

$$T = T_R + N_{rep}\left(\tau \times \frac{A}{(\Delta d)^2}\right), \quad \textbf{4.1}$$

where T_R is the amount of time for the beam to switch between lines in the 'Raster' mode. A is area of the pattern. The number of repetitions N_{rep} is given below:

$$N_{rep} = \frac{\Delta D}{\Delta D_0}, \quad \textbf{4.2}$$

ΔD is the total dose and ΔD_0 is the exposure dose for each repetition, which is defined as below:

$$\Delta D_0 \cdot (\Delta d)^2 \equiv I \cdot \tau, \quad \textbf{4.3}$$

If one substitutes equation 4.2 and 4.3 into 4.1, one finds a simple relation:

$$T = T_R + \frac{\Delta D \cdot A}{I}, \quad \textbf{4.4}$$

When the pattern size A and current I are fixed, the only variable is the dose ΔD. One can experimentally obtain a good value for ΔD from a group of milling results. However, it is not necessarily true that any combinations of τ and Δd that gives same ΔD will result in same good milling result. Figure 4.22 shows two patterning configurations (both raster scan) that share the total dose, but with very different grid division. In Figure 4.22 (a), the pixel spacing Δd is smaller and the dwell time τ on each pixel is shorter, whereas in Figure 4.22 (b) the grid is less dense but has a larger dwell time on each pixel. Although these two configurations give exactly the same total dose, the parameters outlined in (a) gives better result in general, as the dose is better distributed and break the bonds more easily whilst the long dwell time in (b) doesn't necessarily improve the sputtering process beyond a certain level and induces damage to the substrate.

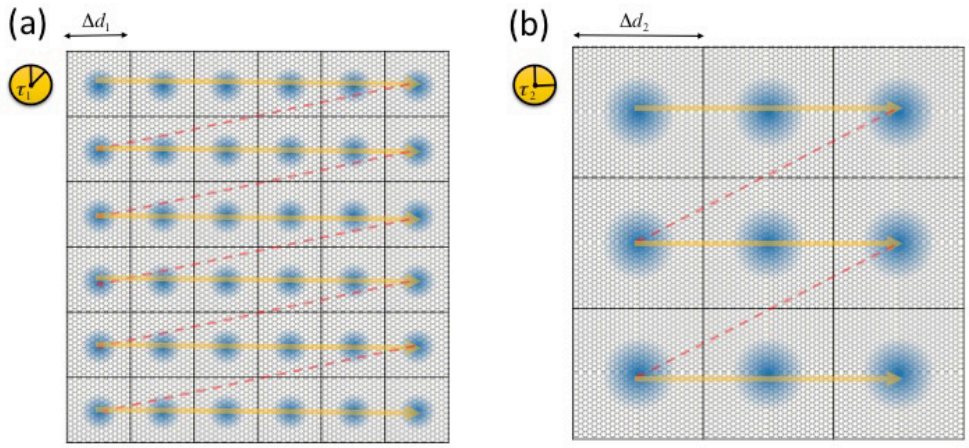

Figure 4.22 Two milling configurations with same total dose but different pixel spacing and dwell time.$\Delta d_1 = 1/2\Delta d_2$, $\tau_1 = 1/2\ \tau_2$. The yellow arrows indicate the movement of beam while the red dashed arrows show the jumping between lines in raster scan mode. Here only one repetition is demonstrated.

In addition to the mesh configuration mentioned above, another parameter that can affect the milling result is the repetition number N_{rep}. The mill profile can be largely altered by N since repetitions help clean up re-deposition of milled material. The pattern style, i.e., the scanning order can also change the milling profile, which is particularly true for large patterns. This is best illustrated in Figure 4.23 [146].

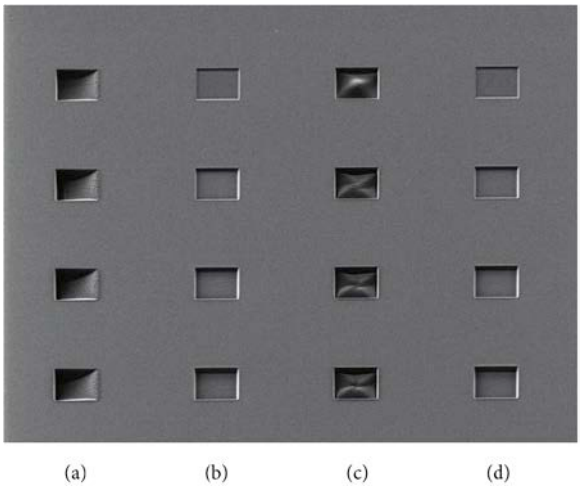

Figure 4.23 SE image scanned by gallium ion beam on milling patterns using different filling algorithms, dose and repetitions[146]. Scanning vertical lines filling from right to left was used in ((a) and (b)), and filling with concentric rectangular frames from centre outward was used in ((c) and (d)). The full dose was delivered in 1 scan in (a) and (c), while the dose was distributed to 200 repetitions in (b) and (d). The ion dose is increasing downward along the squares by the same amount in all columns ((a)–(d))

4.3.4 Substrate swelling due to milling

One could intuitively assume milling graphene should only require small dose because graphene is atomic thin. However, supported graphene sample has a different situation because the sputtered substrate can play a role here. The milling on this type of sample is investigated in this section.

Figure 4.24 shows a series of U-shape channels milled by HIM. The U-shape device has previously been fabricated using FIB and showed extraordinary on-off ratio[147]. The dose for HIM milling was 6.2×10^{17} cm^{-2}. The beam current is 1 pA with 10μm aperture size. Initially swelling was not discovered from the SE image taken by the HIM. AFM scan reveals the topography and found a swelling height of ~35 nm at the milling site. The phenomenon of swelling has been found in crystallized Si bombarded by high energy gallium ion [148] and is usually related to amorphisation because amorphous Si is less dense than crystallized Si, which induces expansion of volume[149]. In our case, swelling is not desired as the amorphous substrate creates leakage paths and bumped area induces strain that may modulate the band structure of graphene [150].

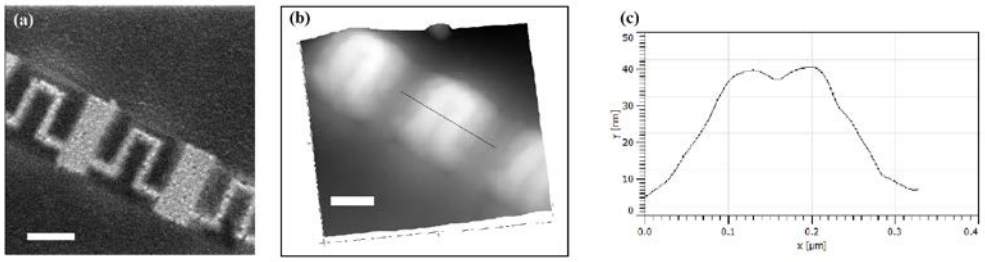

Figure 4.24 (a) HIM micrograph of three as-milled U-shape graphene GNRs covered by ~8 nm Al_2O_3 (b) AFM image of the same features. Scale bar is 100nm for both graphs. (c) Cross section of the GNR shown in (b).

The swelling can be caused by two mechanisms: amorphisation and redeposition. The dose needed for sputtering is usually two orders of magnitude higher than amorphisation. The FIB beam intensity can be modelled by a Gaussian ion distribution where the beam fringe has much lower intensity compared to the beam core, which can result in swelling[151,152]. It has been suggested that swelling can finally be eliminated at high irradiation dose for gallium ion beam [153]. However, this is not the case for helium ions. As shown in Figure 4.25 (a), 300 nm SiO_2 substrate was bombarded by helium with a set of dose values. The swelling height increase monotonically with the irradiation dose from 3.1×10^{17} cm^{-2} to 6.2×10^{18} cm^{-2}. Only at very low dose (< 6.2×10^{17} cm^{-2}) is the swelling less significant than milling. It is also observed that swelling height also increases with the patterning area, as shown Figure 4.25 (b), where the same sample was patterned with box size from 100 to 500nm, with a constant dose of 1.2×10^{18} cm^{-2}, dwell time of 3 µs and 655 repetitions. The dependence of swelling height on pattern area may be caused by redeposition but further study is needed to fully examine this problem. This is certainly not desirable as one would like to have the freedom on choice of patterns with consistent milling. It seems that the redisposition is always

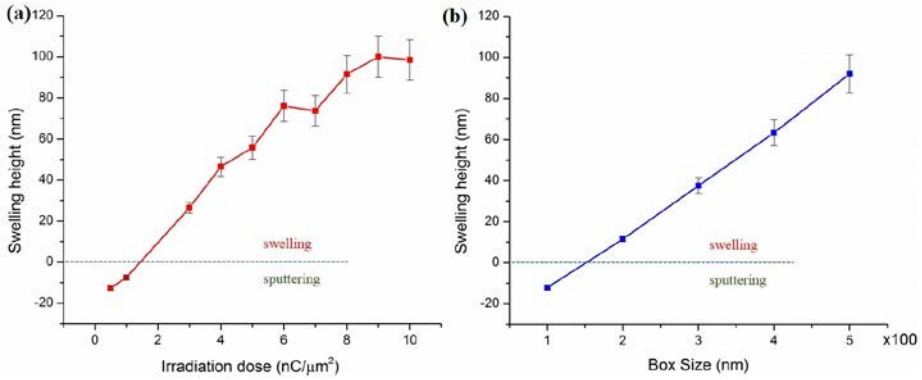

Figure 4.25 Swelling height plotted against (a) irradiation doses with constant box size = 150 nm, (b) pattern area (square boxes with size from 100-500 nm side length) with constant dose = 1.2×10^{18} cm^{-2}

We solved this problem by changing the incident angle of the helium ion beam. The working distance (WD) was adjusted to ~16mm to prevent accidental damage of the microscope during the rotation of the sample holder. The tilt was gradually varied from 0^o to 46^o and evolution of etching/swelling is shown in Figure 4.26. At low tilt (up to 20^o), the beam induces large area of swelling near the milling site forming a single ridge towards the middle. Despite small swelling at the edge, drastic change occurs at around 30^o tilt, where sputtering is dominant over the amorphisation-induced swelling. It is well-known that sputtering yield increases with incidence angle until a maximum is reached around ~80^o after which sputtering yield drops dramatically[153]. However due to the limited angle we could rotate the sample stage in a HIM, the maximum angle reached is 46^o. Swelling is completely eliminated at 46^o but it should be noted that the patterning resolution is degraded as the beam tilts, as found experimentally (see Figure 4.26). As a result, 40^o tilt is chosen as the optimum angle experimentally since the swelling is negligible while resolution is maintained.

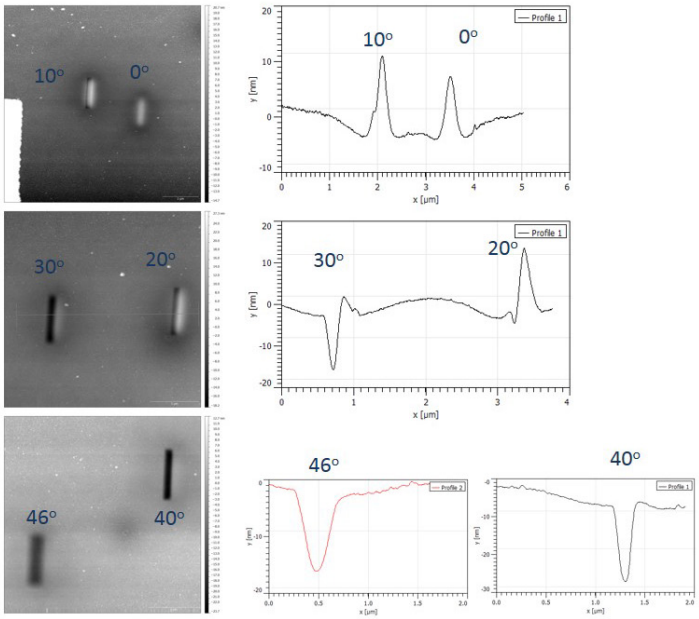

Figure 4.26 AFM topology of boxes (100nm by 1um) carved at different tilt with consistent beam conditions: dose = 1.24×10^{18} cm^{-2}, pixel spacing = 1 nm, dwell time = 3 µs. Right panels show the cross section views.

With a tilt beam, sputtering can be performed without swelling. Figure 4.27 (a-b) shows the milling of 30 nm lines with different dose. Unlike the un-tilt case, increasing dose did not cause swelling but enhanced the milling, as one would expect for a milling process where material is removed. The etching depth now depend weakly on the pattern size as shown Figure 4.27 (c-d).

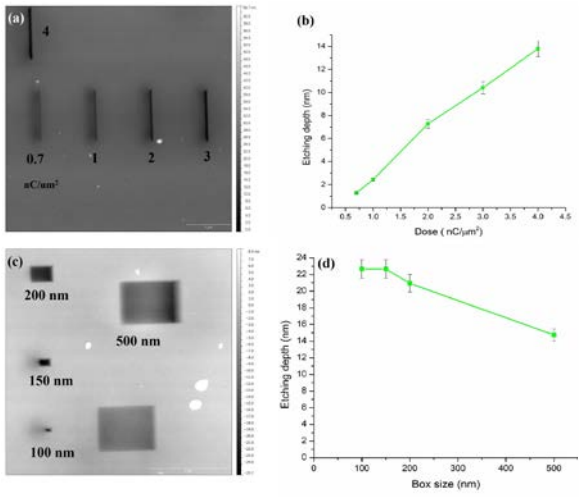

Figure 4.27 (a) The AFM image of lines carved at 40^{o} tilt with increasing dose. (b) The etching depth plotted against irradiation dose. (c) AFM image of milled boxes at dose 1.24×10^{18} cm^{-2}. (d) The etching depth plotted against box size.

Fox *et al* [145] experimentally showed that 35 keV helium ion beam creates helium bubbles at ~318 nm underneath the surface of silicon substrate, which is in accordance

with Monte Carlo simulation. The swelling observed in our experiment can be attributed to the formation of these subsurface voids, in which the voids seems to be "steered" away by the angled beam.

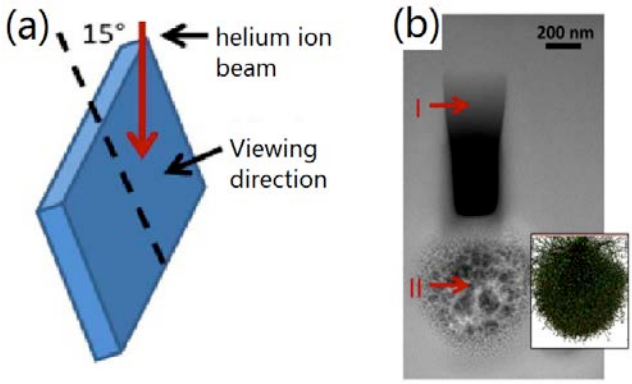

Figure 4.28 Helium ion exposure on a silicon lamella[145]. (a) Schematic of the beam. (b) High angle annular dark field (HAADF) image of the irradiated lamella showing etched wedge and an amorphous circular area due to ion implantation

Once the above-mentioned beam condition (focus, current, dose, repetition, tilt, etc.) is finely tuned, pristine graphene can be very 'milling friendly'. A couple of examples illustrating the patterning capability of HIM are 20 nm wide nano-ring and 20nm-diameter DQD structures, as shown in Figure 4.29 and Figure 4.30, respectively.

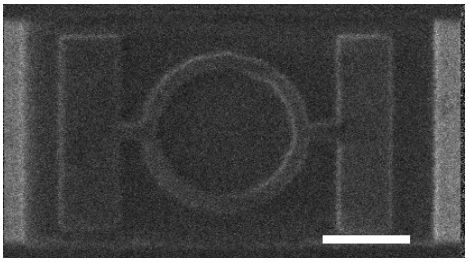

Figure 4.29 A graphene ring structure milled by HIM. Dose = 1.6×10^{18} cm^{-2}. Beam current = 1 pA. Scalebar = 100 nm.

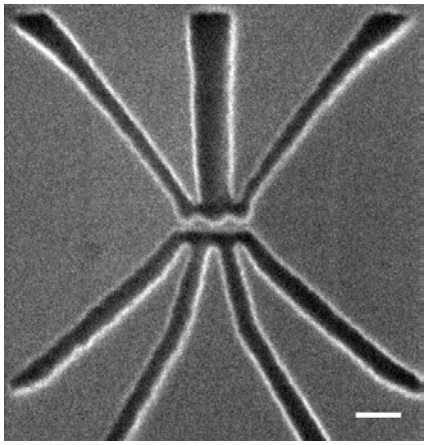

Figure 4.30 Graphene double quantum dots milled by HIM. Dose = 1.6×10^{18} cm^{-2}. Beam current = 1 pA. Scalebar = 50 nm.

4.3.5 EBL-HIM hybrid fabrication process for graphene devices

Although HIM gives a better resolution over EBL at small scale, replacing the whole EBL process with HIM is not practical. This is because the current HIM does not have the same flexibility of beam-steering and alignment as EBL. Furthermore, because it is the beam dwelling that essentially facilitates the milling of material, the ion beam writing time scales with writing area. For instance, the milling of a box (1 μm×1 μm) using a dose of 1.24×10^{18} cm^{-2} at 1 pA takes ~ 33 min according to equation 4.4. In the meantime, the stage is likely to drift, which is a common issue in the current generation HIM. As a result, it is preferred to use HIM for patterning small features only.

Hereby we established a hybrid EBL-HIM patterning method for making extremely downscaled graphene electronic devices, in which coarse etching layer and metal contacts are defined by EBL while the smallest features are milled by HIM afterwards.

One concern in the process integration is that the resist residue left by the EBL step can have a negative effect on milling. It was found in our previous study that milling on resist-treated graphene samples appears to be very difficult to mill [154]. This is possibly because the residue forms a protective layer on graphene surface. This is most noticeable in the case of methyl methacrylate (MMA), which is commonly used in conjunction with poly-methyl-methacrylate (PMMA) in a bilayer lift-off process. Figure 4.31 shows the milling results on flakes pre-treated with MMA for increasing doses. It can be seen from

(c) where a pattern is placed at the edge of a flake, that graphene is not milled even at heavy exposure.

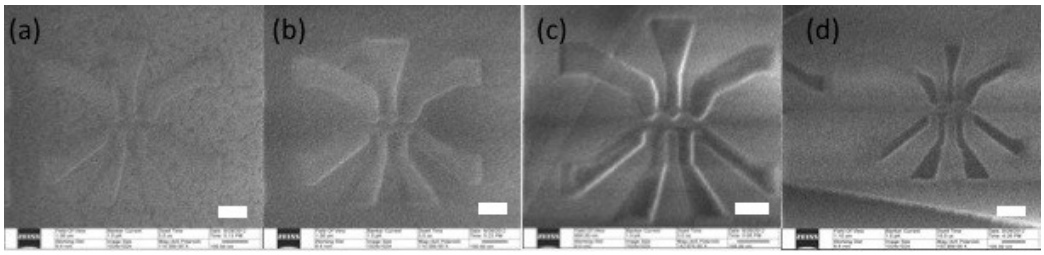

Figure 4.31 Unsuccessful milling on graphene flakes pre-treated by MMA (HIM images). The dose was increased gradually, but milling can hardly be improved. Dose values and number of repetitions are: (a) 3.7×10^{17} cm^{-2}, 11 (b) 4.6×10^{17} cm^{-2}, 25(c) 6.2×10^{17} cm^{-2}, 45 and (d) 9.3×10^{17} cm^{-2}, 75. Scalebar is 100 nm. Beam current = 1 pA.

Thermal annealing has been widely used to clean as-fabricated graphene device [155–158]. We also heated our sample at 300^{o} in forming gas (94% N_2 and 6% H_2) for several hours. However, the annealed graphene flakes are still resistant to HIM milling. As shown in Figure 4.31, the milling of a DQD pattern was attempted on different locations of the same graphene flake that was previously treated with MMA and annealed after. The annealing did not completely remove the MMA residue and seems to have harden the residue that makes the milling process more difficult. Similarly, a mechanical cleaning method has also been attempted [159] prior to HIM milling. As shown in Figure 4.32 (a), the sample was scanned using AFM tip (contact mode) until the surface roughness R_A is minimized (Figure 4.32 (b)). As can be seen from both AFM and HIM images, the polymer residue is aggregated at the edge of the flake due to the AFM tip scanning the flake in contact mode(Figure 4.32(c-d)). However, no significant improvement on milling was observed. Figure 4.32(c) shows the HIM image of the same graphene flake that was treated by the mechanical cleaning. DQD patterns could not be milled well at dose of $6.2.x\ 10^{17}\ cm^{-2}$.

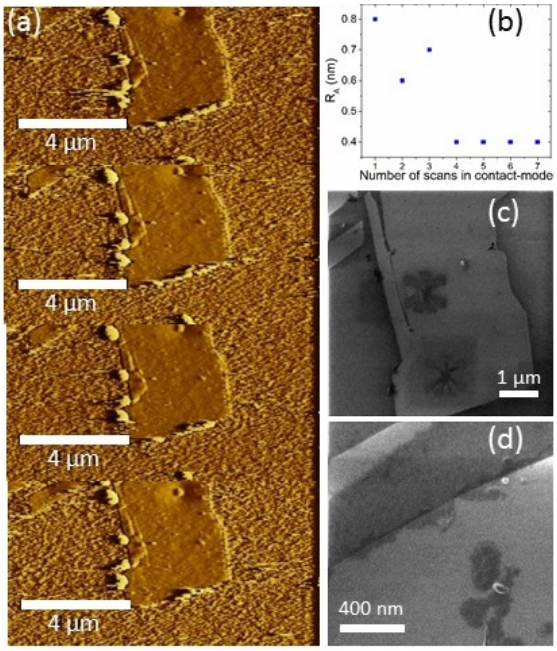

Figure 4.32 (a) Mechanical cleaning using contact-mode AFM. (b) Surface roughness measured for each scan. (c) HIM image of graphene flake patterned by HIM after mechanical cleaning. (d) HIM image of a graphene flake with resist residue accumulated at the edge due to mechanical cleaning by AFM.

Interestingly, the same issue was not seen for other resist including PMMA, ZEP and Lift-off resist (LOR). The sample shown in Figure 4.33 is a single layer flake prepared by exfoliation of graphite. The wide isolation line at the right side of the flake was patterned by EBL using 42nm PMMA. The randomly distributed stripes on graphene are perhaps the residue of PMMA.

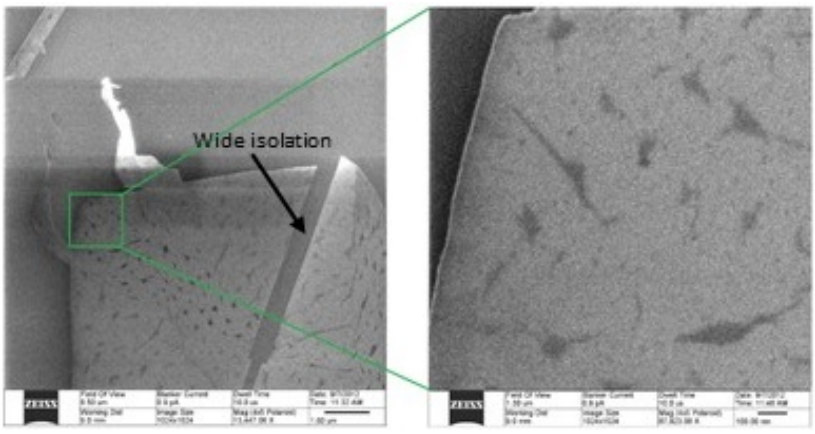

Figure 4.33 The resist residue of PMMA on graphene

In order to mill the graphene flake, the acceleration voltage is set to ~ 30 kV and beam current is set to 1 pA (by changing the He pressure and spot control). The optimum dose for milling well-defined features on graphene is around 4.03×10^{17} cm^{-2}. Figure 4.34 (a)

and (b) show the comparison of milling results for two doses on MLG. Figure 4.34 (c) is a blow-up view of the DQD structure milled using the 4.03×10^{17} cm^{-2} dose. The structure is well defined compared to the less reliable EBL results. The main dimensions are extracted as follows: quantum dot size ~ 55×60 nm^2, gate-dot distance ~26 nm, constriction width ~ 40 nm. Albeit a little bit under-exposure, this is clearly a proof HIM's feasibility of ultrafine graphene patterning.

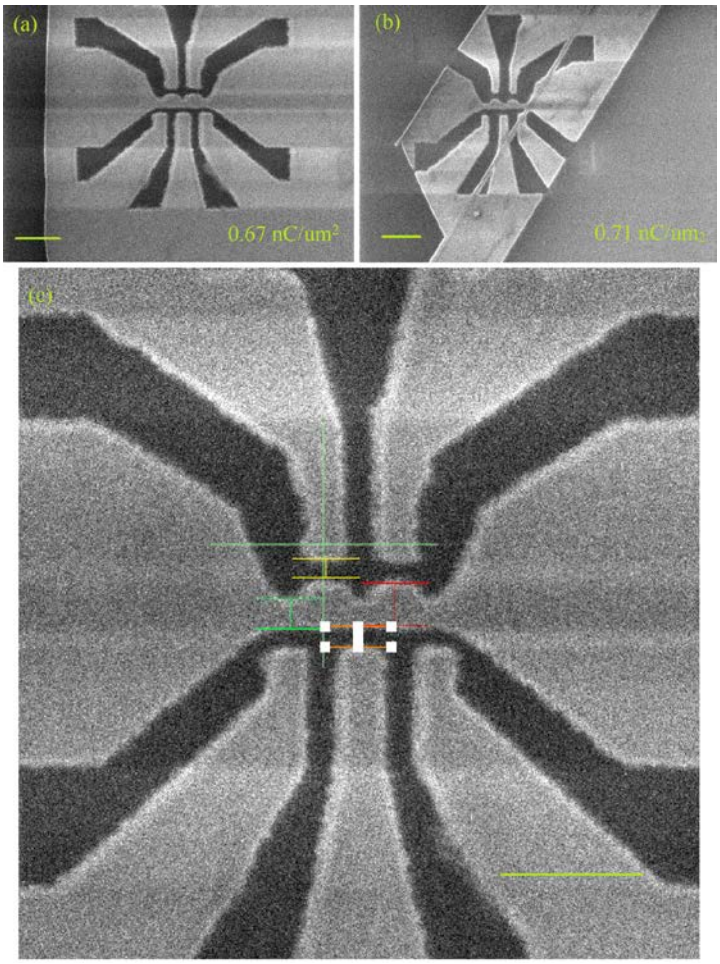

Figure 4.34 DQD structures patterned by HIM milling with two doses (a) 4.15×10^{17} cm^{-2} and (b) 4.40×10^{17} cm^{-2} (c) The blow-up of the central area in (a) with colour lines measuring key dimensions: d = 26 nm, W_{cons} = 40 nm, D = 55 nm. Scale bar: 200 nm.

In order to successfully fabricate a device, the HIM milling pattern needs to be precisely positioned in the middle of EBL-defined isolations. Initially this alignment is done by first taking a snapshot of the target area followed by manually aligning the pattern in the centre. However, the bombardment of helium ions during imaging inevitably creates some defects in graphene. Therefore, it is best to expose the target area only while blanking the beam at the rest of the flake. This can be done by introducing an additional

alignment mark away from the exposure area (see Figure 4.35). The alignment mark is located at the edge of the flake. The HIM magnification is adjusted such that the main device channel is outside the field of view (FOV). The pattern is then milled using an external Xenos® pattern generator using the GDSII file.

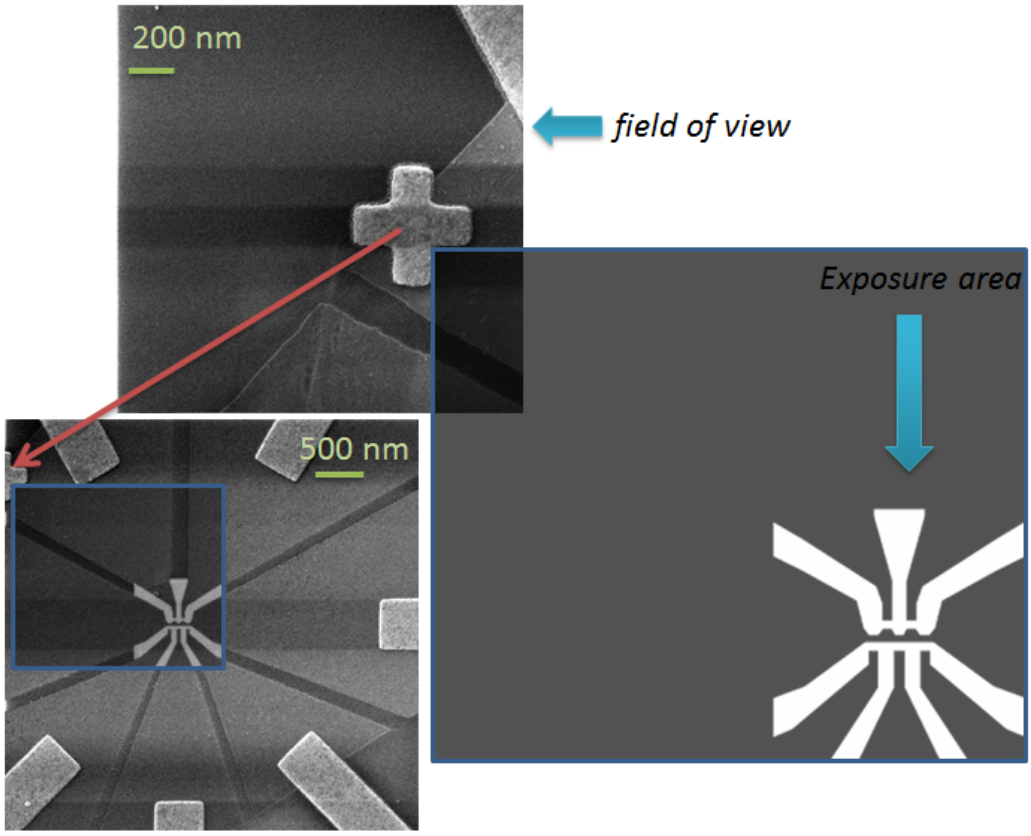

Figure 4.35 Manual alignment in HIM. Extra alignment mark is positioned around the flake. Magnification is adjusted such that the exposure area is out of the FOV. By using the external pattern generator, patterns can be written remotely.

4.4 Conclusions

In this chapter, we discussed the fabrication techniques for our graphene devices, which comprises two parts: a well-established e-beam based process and the integration of helium ion beam milling technology. Both graphene isolation layer and metallisation layer are defined by the e-beam lithography. A third layer of AlO_x top-gate can be added in the same manner for providing additional modulation and device passivation. A side gate approach made by etching was also demonstrated. The helium ion milling is applied for two purposes: irradiation and milling. The operation of a helium ion microscope was discussed along with principles of ion milling. Fine milling of several patterns were illustrated including a 20 nm graphene quantum dot.

Chapter 5 Raman study of damage extent in graphene nanostructures carved by HIM

5.1 Introduction

Despite the high resolution and the ease of pattern choice, most of the fabrication achievement using HIM were carried out on suspended graphene, limiting its usefulness for many practical applications where a substrate is needed[160,161]. In addition, suspended graphene devices are difficult to handle and are not suitable for many practical applications, mainly because the variable range of gate modulation is restricted to ~5 V avoid electrostatic collapse. On the other hand, recent progress on the quasi-suspended graphene made by stacking with other 2D materials has shown superior properties implying that a structural suspension may no longer be necessary for many high performance devices[161–163]. The mechanisms at play during the carving of suspended graphene and supported graphene can be very different owing the complex interaction between ion/electron beams and the substrate material[148]. For instance, atomic simulation suggests that supported graphene has much larger displacement threshold (T_d) compared to suspended graphene[164]. Lastly, due to the tininess of the device structures, there is yet an effective way to examine the damage on graphene after fabrication. TEM and imaging seems to be a good approach, but again requires the sample to be suspended. STM could potentially be an alternative, however we don't have access to an STM in our lab. The AFM resolution depends on the tip size which is usually larger than atomic size.

In this work, we investigate the extent of the damage in graphene after fine patterning with a highly energetic helium ion beam. The patterned area and its surroundings are

systematically characterized using Raman spectroscopy. We show that backscattered ions and other dislodged substrate atoms are a major source of damage and we propose solutions to minimize the amount of defects in the useful areas of patterned graphene nanodevices.

We show that milling will create defects of various degrees near the milling site by analysing the spatially resolved Raman mapping. We will focus on *G*, *D*, and *D'* peaks because they contain information about defect density[72,81,165,166] and defect type[166,167]. By using the activation model mentioned in section 3.2, L_D can be quantified locally. We will be using the following notations: 1) *I(D)*, *I(G)* and *I(D')* for absolute intensity of *D*, *G* and *D'* peak, respectively 2) *Γ(G)* for the full width at half maximum (FWHM) of *G* peak 3) *I(D)/I(G)* for the ratio of *I(D)* to *I(G)* 4) *I(D)/I(D')* for the ratio of *I(D)* to *I(D')*.

5.2 Experimental

Graphene flakes were prepared by mechanical exfoliation of highly oriented pyrolytic graphite on a 300 nm SiO_2 substrate. Single layer flakes were identified using both an optical contrast method and Raman spectroscopy[78]. As shown in Figure 5.1, the Raman spectrum show a *G* peak at ~1587 cm^{-1} and a sharp *2D* peak at ~2680 cm^{-1} with a ratio *I(G)/I(2D)*~2.37 . No *D* peak at ~ 1344 cm^{-1} was observed in pristine samples. No significant shifts of all the peaks were observed. A Zeiss ORION scanning helium ion microscope (HIM) was used for precision patterning [13,29,32,35,38,142,144]. We consistently accelerated helium ions at 30 kV to obtain good image brightness and contrast. The beam current was maintained at 1 pA. The patterning resolution was 1 pixel/nm^2 and the dwell time on each pixel was 3 μs. Figure 5.1 shows the evolution of Raman spectrum of the same single layer graphene flake which was subjected to an increasing helium ion irradiation dose. The dose for rough imaging is around three orders of magnitude smaller than the dose used for milling and shows little damage on graphene as verified by Raman spectroscopy.

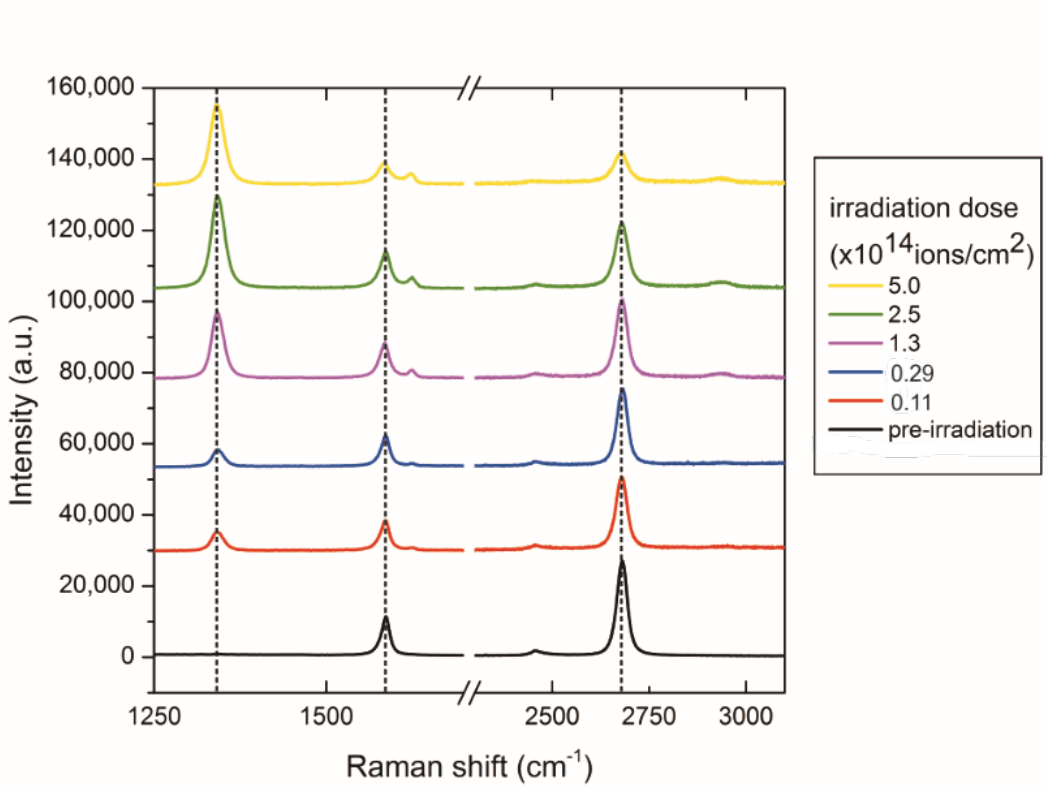

Figure 5.1 Raman spectra of a single layer graphene before and after the irradiation of 30 kV helium ions at various doses

We first conducted milling tests at various conditions on bare SiO_2 to minimize the substrate swelling/re-deposition as the sputtering of substrate atoms is a major source of indirect damage to graphene[164]. The milling profile was measured using tapping mode atomic force microscope (AFM) which has a tip diameter of ~87 nm. As mentioned in the 4.3.4, the swelling is only completely eliminated for tilt angle equal to or larger than 40^{o}. As a result, we chose a beam angle of 43^{o} and irradiation dose of 6.24×10^{17} cm^{-2} to directly carve graphene.

Raman spectrum was acquired using a confocal Raman microscope (RENISHAW inVia^{TM}) with a ×100 lens (numerical aperture 0.8) and a 532 nm (2.33 eV) laser, giving a finite spot radius of ~400 nm. Raman map was obtained over a range spanning from 1000 cm^{-1} to 2100 cm^{-1}, covering the *D* peak, *G* peak and *D'* peak. The distance between each data point is 100 nm. The laser power is maintained at 2mW to prevent thermal heating on the sample surface.

5.3 Results and discussion

Figure 5.2 (a) shows the AFM image of a single layer graphene with a 35 nm wide line carved by HIM with a beam-tilt of 43° and dose of 6.24×10^{17} cm^{-2}. The measured graphene thickness is ~1nm, slightly thicker than clean graphene. This is mainly due to the moisture covering the surface since our measurement was conducted in ambient environment. We adjusted the beam focus at the edges of the graphene prior to milling in the bulk area therefore the corners are flatter owing to a beam-induced cleaning. The inset shows the cross section view of the milled line Figure 5.2 (a) that presents an asymmetric 'V' shaped feature where the slope is less sharp on the left hand side (LHS) of the carved line (a dip at the centre). We attribute this to the structural change in the substrate at the LHS, as will be discussed at the end of this section.

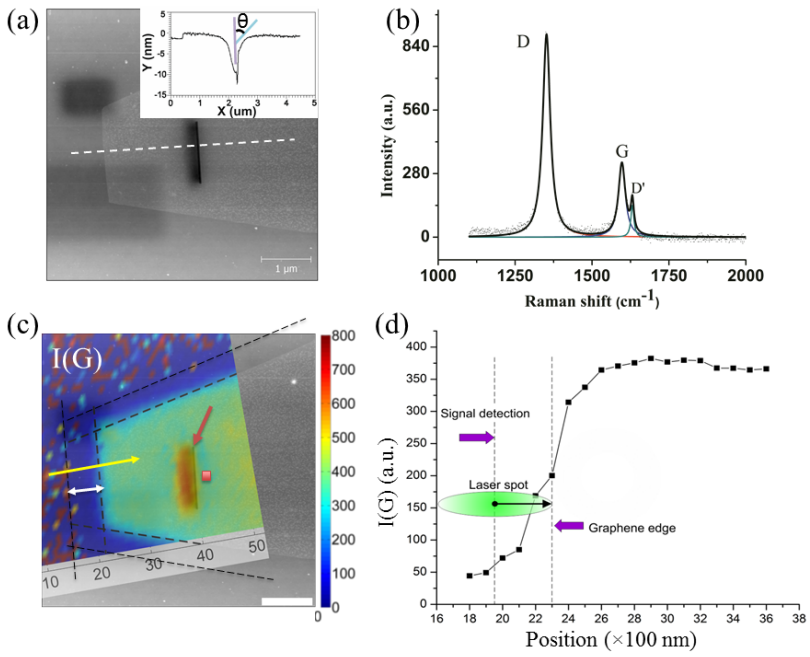

Figure 5.2 (a) AFM image of the graphene with a 30 nm line carved by HIM at 43°, 6.24×10^{17} cm^{-2} dose. The dark squares at the two corners indicate lower topology due to beam-induced cleaning and etching. Inset: the cross section profile along the white dashed line. Purple line indicates normal direction while the blue line indicates the beam direction. θ = 43° is the tilt. (b) The Raman spectra of a point near the milling site (the red dot in (c)) is fitted with three Lorentzian curves centered at corresponding peak positions. (c) Raman mapping on top of AFM image of the same area shown in (a). Outer and inner black dashed lines labelled the onset of *I(G)* and actual edge of the flake, respectively. White double-arrow indicates the inter-line distance of ~400 nm.

The red arrow pointed at the 30 nm carved line(d) *I(G)* values along the yellow arrow across the graphene edge shown in (c).

Raman spectrum at each data point was fitted with three Lorentzians centred at corresponding peak positions as shown in Figure 5.2 (b). We used the *I(G)* map, shown in Figure 5.2 (c), to determine the boundaries of graphene because *I(G)* does not depend on edge type unlike *I(D)* [83]. In Figure 5.2 (d) we plot the *I(*G) values across the edge along the yellow arrow shown in Figure 5.2 (c). The edge is defined as the position where *I(G)* is roughly half of its value inside the flake [83]. This position is ~400nm from where *I(G)* starts to increase, consistent with the spot size of our laser.

Lastly the Raman map is scaled and aligned with the AFM graph to form a hybrid Raman-AFM image (Figure 5.2(c)). Two observations can be made from Figure 5.2 (c). Firstly, *I(G)* is almost constant across the whole flake except an area of 300nm wide at the left of the carved line. *I(G)* should not change too much at Stage 1 disorder[167]. However at Stage 2, the intensity near the original *G* position increases due to 1) merging of *G* and *D'* bands, as can be seen from Figure 5.2 (b) and 2) broadening of *D* band. Secondly, the high *I(G)* region (orange colour in Figure 5.2 (c)) does not centre at the carved line but it is located along the left edge. This is not due to the error caused by manual aligning since the method we described above is fairly accurate. Interestingly, the AFM data shows lower topology at the same location. Therefore, we attribute this asymmetric feature to our milling technique where a tilt beam is applied.

We also observe that *Γ(G)* always increases with disorder[72,81,168,169]. Therefore we use *Γ(G)* map to partition the flake into five regions (A-E) for the convenience of analysis (Figure 5.3). Region A spans 300 nm to the left of the carved line. Region B covers the carved line and a 250 nm wide region to the right of it. Region C and D are where the beam focus is adjusted at high resolution (irradiation dose ~ 8×10^{15} cm^{-2}). E is far from the carved line where less irradiation was introduced. As can be seen from the coloured map, graphene in region A has the largest disorder as $\Gamma(G)_A \sim 60$ cm^{-1}. The graphene near the milling, i.e., region B shows overall less disorder: $\Gamma(G)_B \sim 40$ cm^{-1}. It is usually a good practice to focus the beam near the target site to achieve the best resolution for the actual milling. Focusing on the graphene creates moderate damage at C and D: $\Gamma(G)_C \sim 33$ cm^{-1} and $\Gamma(G)_D \sim 50$ cm^{-1}. Graphene lattice is much preserved in E as $\Gamma(G)_E$ is only around 13 cm^{-1}.

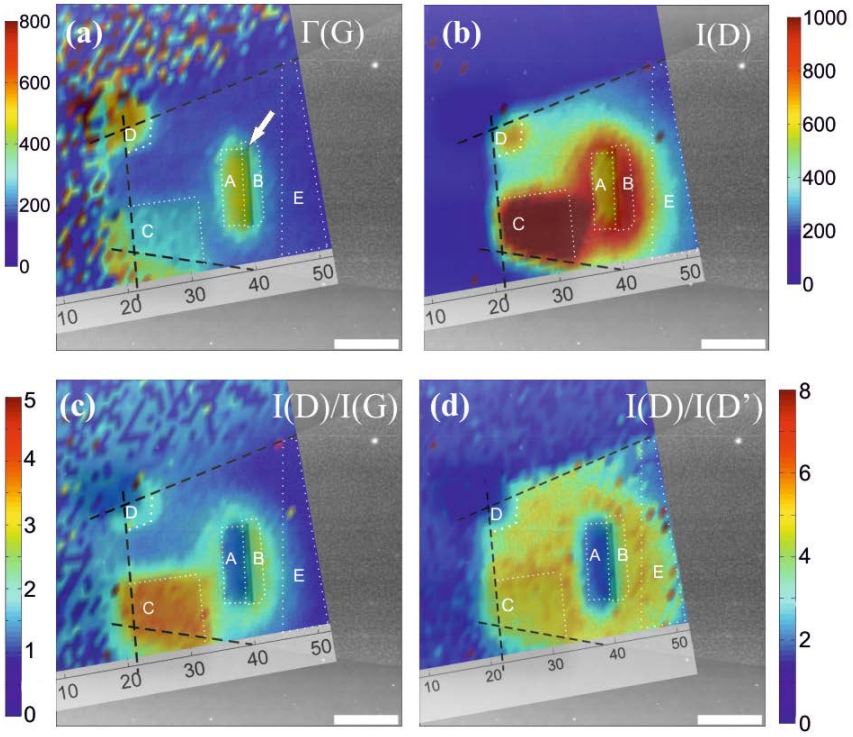

Figure 5.3 (a-d) Mappings of *Γ(G)*, *I(D)*, *I(D)/I(G)* and *I(D)/I(D')* on top of the AFM image shown in Figure 5.3 (a) The unit of the Raman mapping axis is 100nm. Scale bar is 1μm. White dashed lines define the following five regions of interest: A is a 300nm wide area at the LHS adjacent to the carved line. B is an 250nm wide region at RHS containing the carved line (pointed by the white arrow in (a)). C and D are regions where beam focusing was adjusted.

Figure 5.3 (b) shows the map of *I(D)* whose evolution tracks the development of disorder in the graphene lattice. *D* should increase with the defect density in Stage 1 and starts decreasing in Stage 2 due to the loss the hexagonal rings, according to the local activation model [72,81]. In order to derive the L_D in the defective regions induced by helium ion bombardment, the spatial map of *I(D)/I(G)* is obtained as shown in Figure 5.3 (c). Unlike the monotonic increase of *Γ(G)* towards region A, *I(D)/I(G)* near region A has a 'ring' shape. At the centre of the ring (i.e., region A), *I(D)/I(G)* reaches the lowest $I(D)/I(G)_A \sim 1$. At the body of the ring (i.e., region B), $I(D)/I(G)_B$ reads ~2.5. *I(D)/I(G)* has a peak value at region C, $I(D)/I(G)_C \sim 4$. Combining this with the *Γ(G)* data, we can conclude that region B is in Stage 1 disorder while A and D are in Stage 2 disorder. C is near the transition between Stage 1 and Stage 2 disorder. This is done by finding the corresponding L_D of each *I(D)/I(G)* using equation 5.1.

Figure 5.4 shows the plot of equation 5.1, with $r_S = 1$ nm and $r_A = 3$ nm. C_A depends on excitation energy and is experimentally fit by $C_A = 160E_L^{-4}$ where $E_L = 2.33$ eV being the

laser energy[81]. C_S has experimental values of 0.87 or 0, as was determined experimentally in reference[72] and reference[81], respectively. In Stage 1, C_S should account for less than 10% variation of, therefore it is safe to set $C_S = 0$ for all defect types[166]. However in stage 2, C_S has a more significant influence on *I(D)/I(G)* since it dictates the minimum value of *I(D)/I(G)* in this stage when $L_D \rightarrow 0$. In our case, *I(D)/I(G)*>1 is always observed for the most defective region (i.e., region A) implying that C_S has a finite value of ~1. This is because the physical meaning of *Cs* is the contribution of purely S regions to *I(D)/I(G)*, which is the case for highly disorder. As displayed in Figure 5.4, L_D in different regions can be estimated: $L_{D(A)}$~1.5 nm, $L_{D(B)}$~8.5 nm, $L_{D(C)}$ is either ~4.0 nm or ~7.0 nm, $L_{D(D)}$~2.5 nm. Note it is not possible to unambiguously discriminate between the two disorder stages for region C due to the lack of data near the transition point.

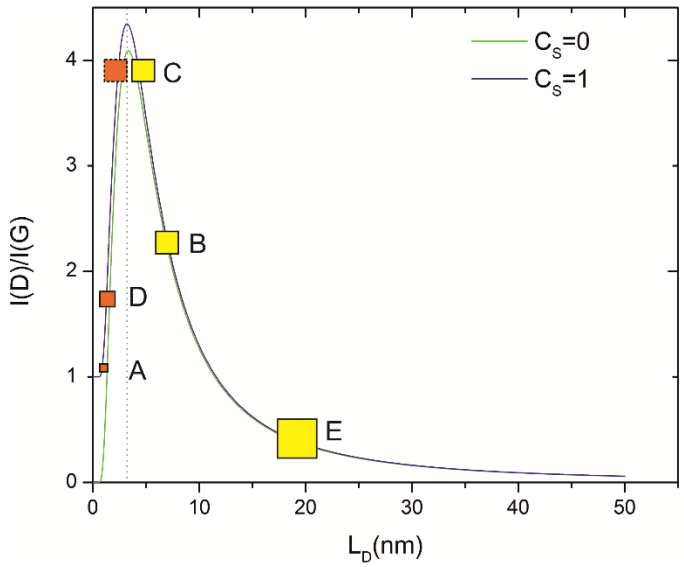

Figure 5.4 Plot of equation 5.1 with *Cs* = 0 (green curve) and *Cs* = 1 (violet curve). Stage 1 disordered regions are illustrated as yellow boxes while Stage 2 disorderd regions are shown as orange boxes. The size of the boxes indicate the deviation of data in these regions.

It is surprising that although the designed pattern is 30 nm wide, the defective region after milling extends to 300 nm to the left (region A) and 250 nm to the right (region B). However, the exact length scale cannot be determined owing to the resolution (~400 nm) of our Raman spectroscopy. Techniques such as tip enhanced Raman spectroscopy (TERS) can be employed where a much higher lateral resolution is provided by an AFM [170,171].

Reference [166,167] demonstrated that *D'* depends on the disorder structure and thus *I(D)/I(D')* can be used to experimentally determine the defect type in graphene. Figure 5.3 (d) shows the *I(D)/I(D')* map of the same sample. The value of *I(D)/I(D')* is ~ 7 for vacancy-type defect created by Ar^+ bombardment, 3.5 for boundary-like defects in graphite and 13 for sp^3-type defect, as observed in reference [167]. In the map shown in Figure 5.3 (d) we see that the for the Stage 1 disorder regions (i.e. C, B and E), *I(D)/I(D')* ~5 is observed. Therefore, we deduce that in our case the graphene lattice near the milling (C, B and E) site may be presented with multiple types of defects, i.e. a mixture of vacancies (single, double and complex) and amorphous area[172]. However, it is not possible to attain information on defect type from *I(D)/I(D')* values for Stage 2 disorder regions (A and D) because defect structure is no longer complete at extremely high defect density[167].

To understand why helium ion milling caused such distribution of damage in graphene and more specifically, to find out the interaction between the helium ion beam and the substrate, a Monte Carlo simulation on the stopping range of ions using SRIM package [173] was conducted. The simulator tracks the trajectories of 10^5 helium ion ions with 30 keV energy incident 43^o to the target. The target consists of a 0.35 nm thick carbon layer, 300 nm SiO_2 and 700 nm Si. In order to mimic the graphene supported by SiO_2, modifications have been made to the graphite layer. Since graphene binds weakly to the SiO_2, we changed the surface binding energy E_B to 15meV from previous first principle calculations[174]. We also changed the displacement threshold T_d to 68 eV as more energy is required to displace C atom in supported graphene compared to suspended graphene [164]. Here we consider a stable configuration where an O atom on the SiO_2 surface (either O-terminated or OH-terminated) is below the hollow site of C hexagonal ring [164,174]. As shown in Figure 5.5 (a) where X and Y position indicate the lateral position and depth respectively, most helium ions stop at around 250 nm inside the oxide. Although only 3% of incident helium ions were backscattered to the surface, almost all of these ions escaped the surface from the LHS of the milled line within 100-300 nm of the ion incident location, consistent with the size of region A. This could be a potential source of defect formation in region A as these escaped helium ions remain energetic with a large scattering cross-section. In addition to backscattered ions, recoiled Si and O atoms that reach the surface should also be responsible for the indirect damage in graphene lattice [164]. Our simulation shows the sputtering yield for Si and O are 0.026 and 0.034,

respectively. Most of these recoil atoms have energy larger than 3 eV, being able to generate various types of defects[10]. Combining the 3% backscattered He^{+}, 2.6% sputtered Si and 3.4% sputtered O atoms gives rise to the estimated dose received in region A of about 5.5×10^{16} cm^{-2}. The simulation is repeated with a normal angle of incident as shown in Figure 5.5 (b). The insets show the ion distribution at the surface. Although the angled case shows large ion density at the LHS, the number of ions that stopped at RHS is significantly reduced in comparison to the non-tilt case.

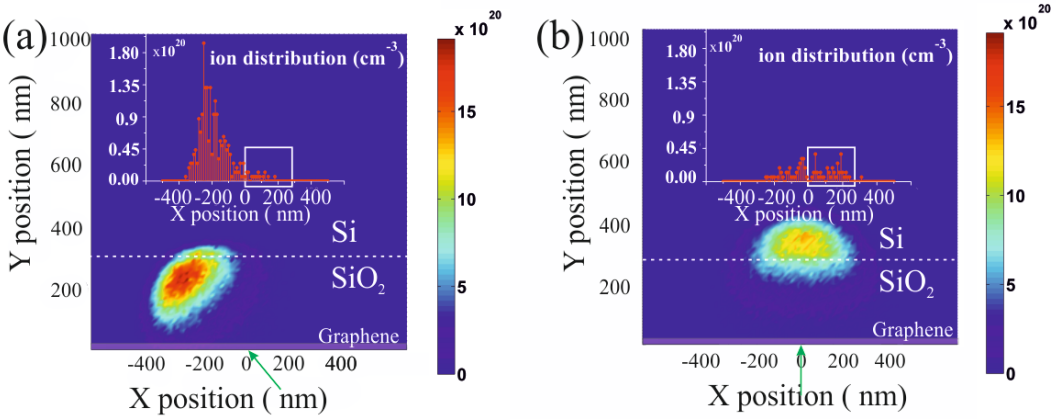

Figure 5.5 SRIM simulation of helium ions distribution inside the Graphene-SiO_2(300nm)-Si(700nm) volume with a dose equal to 6.27×10^{17} cm^{-2} for two different incident angles: (a) 43° tilt (b) 0° tilt. The white dashed lines indicate the interface between Si and SiO_2. Green arrows point at the incident point following the beam direction. The insets show the backscattered ion distribution at the surface. The white rectangles outlines the distance 280 nm to the right of incident point showing distinct difference in the backscattered ion distribution.

We repeated the above-mentioned angled milling (at 43°) technique on graphene with doses close to but smaller the threshold value we found for complete carving (~6.24×10^{17} cm^{-2}). The line width is 5 nm. As can be seen from the AFM image (Figure 5.6 (a)), the tearing of graphene sheet has not developed thoroughly but the adjacent area has already shown wide structural change. Γ(G) and I(D)/I(G) measured at the LHS of the groove are plotted in Figure 5.6 (b) as functions of the irradiation dose. The increase of FWHM with the dose is attributed to the indirect damage by the sputtering of underlying SiO_2 and backscattered helium ions. The I(D)/I(G) data shows a peak value of ~1.9 at 3.74×10^{17} cm^{-2} where Γ(G) is around 29. This is in reasonable agreement with the maximum I(D)/I(G) of 4 where Γ(G) is 33 as found in Region C shown in Figure 5.3 (a), implying the indirect damage caused by such dose level is comparable to the damage caused by direct exposure of helium ions at ~8×10^{15} cm^{-2}.

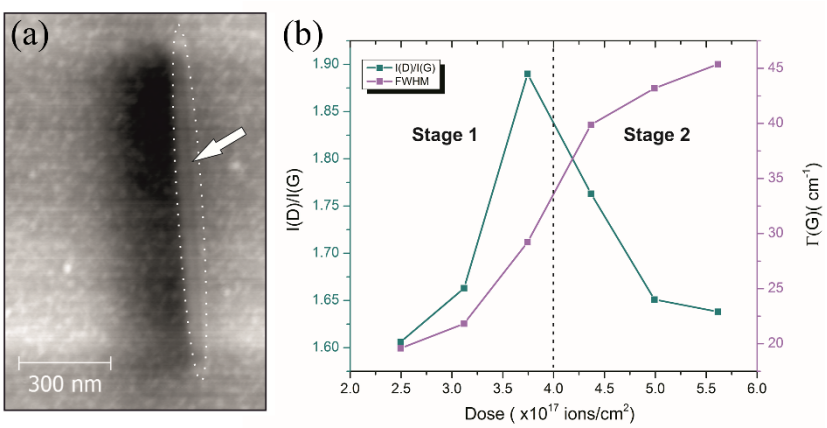

Figure 5.6 (a) AFM image of this sample where a 5 nm groove (enclosed by the white dashed ellipse) starts to appear after irradiation of helium ions at 4.4×10^{17} cm^{-2}. (b) I(D)/I(G) (cyan) and Γ(G) (purple) measured for another sample milled with a set of doses lower than the threshold value.

It has been found that the as-fabricated down-scaled graphene nano-electronic devices no longer shows characteristics of graphene such as gate tunability, after being carved by a well-focused helium ion beam[29]. This is shown in Figure 5.7 (a) where a U-shape GNR channel was fabricated by helium milling. The I-V characteristic is linear showing a resistance of ~1 MΩ, but no gate modulation was observed (at negligible gate leakage). We attribute this to the highly disordered carbon network caused by milling at 0^o angle of incident. We hereby propose a novel fabrication technique that dynamically tilts the beam in order to shift the damage of the backscattered ions and sputtered atoms to the far side of the active region, thus preserving the channel itself. This is schematically illustrated in Figure 5.7 (b). Also shown Monte Carlo simulation of incident ions trajectories. For instance, the beam will be tilted twice to mill at both sides of a GNR. As can be seen from Figure 5.7 (c), our method effectively avoids the damage in the centre channel region while milling from a normal direction has equal damage on both sides of the beam.

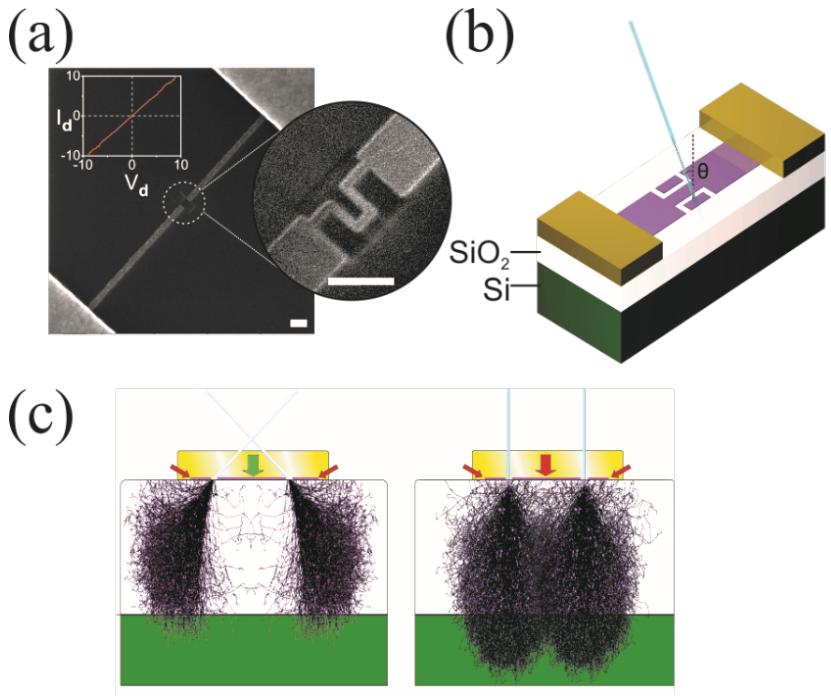

Figure 5.7 (a) The HIM image of a 50 nm wide U-shape channel carved on a GNR. Both scale bars are 200 nm. The inset is the drain-source IV curve. (b) Schematic of a GNR device being carved by a tilt helium ion beam. (c) Schematic drawing of the helium carving of a graphene device using a tilted and a non-tilted beam. Also shown the helium ions trajectories inside the substrate, calculated using Monte Carlo simulation. Green and red arrows point at the preserved graphene and highly damaged graphene, respectively.

5.4 Conclusions

We performed controlled milling of graphene on SiO_2 using 30 kV helium beam with a tilt angle of 43°. Spatially resolved Raman spectrum near the milling site indicates an asymmetric defect distribution where Stage 2 disorder (L_D~1.5 nm) was found along the direction of incident beam and Stage 1 disorder (L_D~8.5nm) on the other side. The defective region spans ~ 300 nm and ~ 250 nm on each side of the milling site. We attributed the formation of these damaged regions to 1) backscattered helium ions and 2) recoil substrate atoms. Although within Stage 1 disorder, it is not yet clear why the angled beam would generate a ~250 nm on the other side. It could be due to extended edge damage due to milling without He^+ probe size optimisation[33]. Further surface characterisation method is needed to investigate this feature fully. Our work provides knowledge for the characterization of damage induced in ion-beam associated patterning of graphene, which is essential for the downscaling of electronic, spintronic and quantum devices on any 2D materials.

Chapter 6 Electrical characterisation of irradiated graphene devices

6.1 Introduction

In this chapter we extend our discussion on irradiation-modified graphene with a focus on its electrical properties. The fundamental device structure used in this study is irradiated graphene nanoribbon (iGNR) with some variations such as dimension, number of terminals for different purposes. The major findings are revealed in a logical order in which experimental methods were improved step by step. We initially made two-terminal bilayer iGNR devices and observed suppression of ambipolar conductance dependence due to irradiation. Subsequently, we made similar structures using single layer graphene and irradiate them with increasing dose and a metal-insulator transition was observed. In order to clarify the mechanism behind, four-terminal iGNR devices of variable lengths were fabricated and displayed a signature of strong localization. This is followed by temperature-dependence measurement on iGNRs with patterned irradiation zones where the energy barriers were estimated. Lastly, an X-ray photoelectron spectroscope (XPS) was used to provide possible explanation of above-mentioned findings.

6.2 Suppression of ambipolar behaviour

It is our interest to study any influence that HIM irradiation could potentially have on the transport properties of graphene devices. In order to examine this systematically, graphene channel of 200nm wide and 2μm long was fabricated using methods described in 4.2.3 on BLG (Figure 6.1). Defects created by helium ions under different dose was deliberately introduced to create point defects in the GNR.

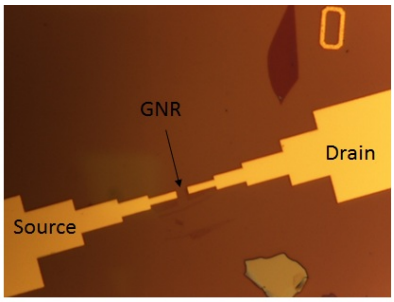

Figure 6.1 Optical image of the GNR device contacted by source/drain electrodes.

Graphene in ambient environment is usually hole doped due to O_2 and H_2O molecules adsorbed on the surface [156]. Besides, residues of e-beam resist are source of external scattering centres and degrade its electronic properties, e.g. electron/hole mobility [158]. Thermal annealing method was conducted to clean the graphene sample bringing the graphene back to intrinsic condition. However annealing at excessive temperature (>400 ^{o}C) was found to increase the coupling between graphene and SiO_2 substrate resulting in more hole doping [158]. Our device was annealed in forming gas ($H_2^{6\%}/N_2^{94\%}$) at 350^{o}C for 1h30mins before the irradiation of helium ions and also prior to the electrical measurement. This cleaning procedure should assist the irradiation process as it 'burns' some of the PMMA/MMA residue which somehow 'protects' the graphene surface from ions bombardment. Figure 6.2 shows (a) the I_d-V_g curves for different bias voltage V_d and (b) the resistance against V_g swept in two directions. The asymmetric I_d-V_g curve observed in (a) and resistance hysteresis in (b) indicate that the hole doping is probably due to the trapped charges near the graphene-oxide interface rather than the resist residue or air molecules since the sample was annealed just before the measurement.

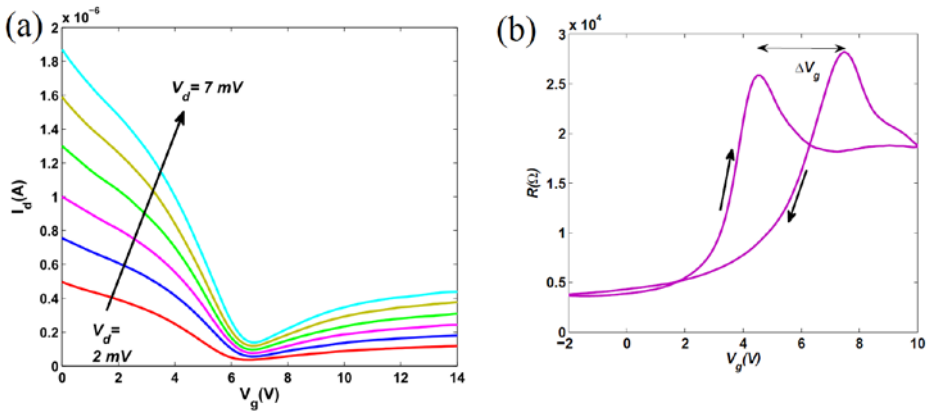

Figure 6.2 (a) I_d-V_g plot at different source-drain voltage showing bipolar characteristic of graphene. (b) Resistance of the GNR as a function of V_g. Hysteresis is probably due to charge traps in the substrate.

Figure 6.3 shows the measured conductivity against $V_g - V_{NP}$ for the same nanoribbon device under three radiation doses. The black lines are the linear fitting of Boltzmann expression $\sigma = n\mu e$, where carrier density is proportional to back-gate voltage by $n = \frac{C_g}{e}(V_{BG} - V_{NP})$, where V_{NP} is the voltage neutrality point. Three findings can be summarised form Figure 6.3. 1) There is a clear sub-linear bending at large carrier density in the hole conduction for pre-radiation and moderate irradiation. 2) The conductivity approaches to linear for the highest dose. 3) The irradiation decreases the carrier mobility ($\mu = (C_g \cdot \frac{W}{L})^{-1} \cdot \frac{dG}{dV_g}$) and broadens the minimum conductivity plateau which is consistent with previous theoretical work [175] The minimum conductivity decreases with the irradiation dose (inset).

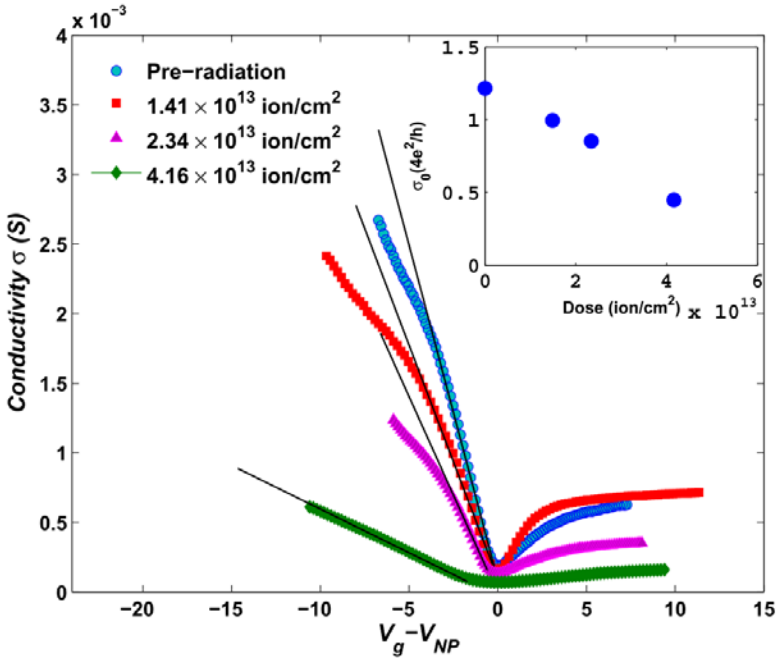

Figure 6.3 Conductivity as a function of V_g-V_{NP}. Sublinear bending in conductance was found at the negative side where holes are majority carriers. Inset: minimum conductivity σ_0 as a function of dose.

At lower carrier density, the linear dependence before the radiation is more likely due to the charge impurities rather than short range scatterers since we annealed our sample, although both of which result in linear dependence [41]. The sublinear bending at large carrier density certainly cannot be explained by these two scattering mechanism. Neither the phonon scattering nor rippling in BLG can contribute to the sub-linearity to such extent. However, if we take into account of the finite width of the BLG ribbon, the sub-linearity emerges as a result of diffusive transport at the edges (see discussion below).

The transition from sub-linear bending to linear is also in contrast with the findings in previous experimental work [176], in which the conductivity dependence is always sub-linear at large carrier density for BLG in the presence of charged impurities.

Point defects are created when graphene is subject to irradiation as some of the carbon atoms are sputtered by high energy helium ions. This is justified by Raman spectroscopy [167] on the radiated sample where a D peak indicating the defects is found around 1360 cm^{-1}(Figure 6.4). Most of the helium ions penetrate deep (~300 nm) inside the oxide therefore we deem that they are remote and do not contribute significantly to the screened Coulomb scattering which also brings the dependence back to linear[50]. Instead, vacancy-like point defects are resonant scatterers which gives rise to linear dependence in BLG [177].

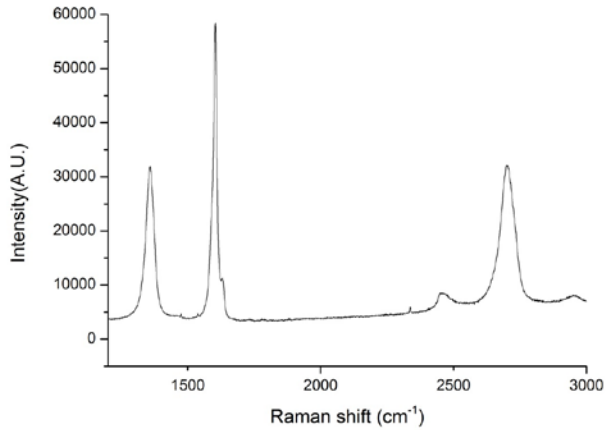

Figure 6.4 Raman spectroscopy of the irradiated GNR. Defect peak at ~ 1370 cm^{-1} was detected.

Here the finite width (w) of our iGNR must be taken into account since it is comparable with the electron mean free path (l_{MFP}~$10w$) due to the diffusive scattering at the lithographically defined graphene edges. An approximation of the resistivity for $l_{MFP}/w \leq 10$ is given by $\rho = \rho_0(1 + \frac{4}{3\pi}\frac{l_{MFP}}{w})$ [134], where $\rho_0$is the resistivity of infinite large graphene sheet considering other scattering mechanism (e.g. impurities, short range, etc.). The mean free path is related to conductivity by $l_{MFP} = \frac{h\sigma}{2e^2 k_F}$[39,134,178], where $k_F$is the Fermi wave vector in BLG $k_F = \sqrt{\pi n}$. The conductivity prior to the irradiation is given by $\sigma_0 = \frac{4e^2}{\pi h}\frac{n}{n_{imp}} = {\rho_0}^{-1}$, only taking into account the scattering of charged impurities (proper approximation for annealed sample). After some simple substitution, an explicit form of conductivity can be obtained, which is valid when $l_{MFP} \leq 10w$:

$$\sigma_n = \rho^{-1} = \frac{4e^2}{\pi h} \cdot \frac{n}{n_{imp}} [1 + \frac{8}{3\pi^{\frac{5}{2}}} \cdot \frac{\sqrt{n}}{n_{imp} w}]^{-1} \qquad \textbf{6.1}$$

The n-term and the$\sqrt{n}$ term (in the bracket) result in the linear dependence and sub-linear bending in the conductivity, respectively. When subject to helium ion radiation, the impurity concentration n_{imp} is replaced by $n_{imp} = n_{imp} + n_d (n_d = 0$ for pre-radiation case), where n_d is the defect concentration. One finds the dependence on GNR width vanishes when n_d is too high and the linear dependence prevails, which is the case for the strongest radiation case in our experiment.

Both $n_{imp}$and n_d can be extracted from the fitting of equation 6.1 to experimental data (Figure 6.5). The impurities concentration is found to be $n_{imp} \approx 7.36 \times 10^9 \text{cm}^{-2}$ from the fitting to the pre-radiation data. This value is inserted back to determine the defects concentrations which are shown in Table 6.1.

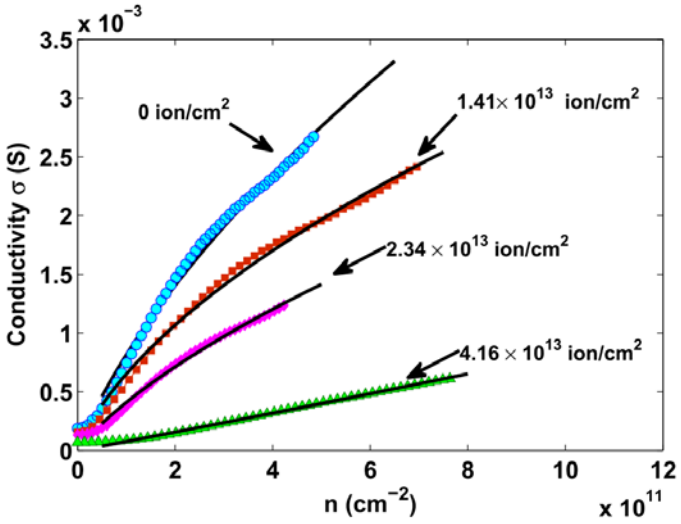

Figure 6.5 The hole conductivity of same GNR after irradiation. Blacklines are the fitting of equation 6.1. The irradiation doses are as labelled.

Table 6-1 The defects densities (n_d) and mean free path (l_{MFP}) extracted from the data fitting. Defects density increases with irradiation dose.

Irradiation dose ($\times 10^{13}$ ion/cm^2)	1.41	2.34	4.16
n_d ($\times 10^9$ cm^{-2})	3.40	6.53	52.0
l_{MFP} (nm) at $n = 1.5 \times 10^{11} cm^{-2}$	~129	~98	~23

In conclusion, the sub-linear bending in the conductivity has been observed in BLG. Point defects are generated by helium ion bombardment. The sub-linearity before irradiation is attributed to the edge scattering owing to the finite width of the GNR. As irradiation generates more defects into the channel, the mean free path is largely reduced and the conductivity is dominant by the initial charged impurities and irradiation-induced point defects, which give rise to a linear dependency, hence the transition.

6.3 Metal-insulator transition

The electronic properties of graphene are highly affected by the presence of defects such as vacancies and adsorbed molecular species [56]. Hence deliberate introduction of these defects can be an effective method to tune graphene electronic properties, such as opening band/transport gaps [13]. From single-vacancy to multi-vacancies, and to amorphous carbon, defects can be created step by step by electron/ion irradiation as demonstrated in [76]. Our motivation here is to generate a highly disordered carbon lattice and characterise its room temperature transport properties. As a result, we carried out our previous experiment (6.3) further by irradiating samples with doses two orders of magnitude higher. We measured two-terminal iGNR devices which shown a transition into insulating phase. This study opens possibilities for precision-engineered graphene nanoelectronic devices such as two-dimensional heterostructures and quantum dots, two-dimensional Anderson insulators and etc.

Single layer graphene flakes were obtained by micro-cleavage of HOPG onto Si/SiO_2 substrate. The highly doped Si substrate is used as a back gate. GNRs were patterned using E-beam lithography and oxygen plasma etching. The nanoribbons were 1 um long and 200 nm wide. Ti/Au contacts were defined by EBL and depositor by PVD. The devices were then loaded into a HIM for irradiation. The exposure doses were precisely delivered to the GNR channel using a built-in pattern generator allowing for deliberate introduction of point defects in the channel. For the present study we irradiated the whole GNR in high vacuum chamber (~10^{-7} Torr) with doses ranging from 1 x 10^{15} to 6 x 10^{15} ion/cm^2 at normal incident angle. The samples were taken out from the HIM chamber for electrical measurement at ambient environment (*ex-situ*).

The I_d-V_g characteristic is shown in Figure 6.6. Pre-irradiated and moderately irradiated graphene channel show a usual ambipolar behaviour. The current varies linearly with the

carrier concentration near the charge neutrality point (CNP) and shows a sub-linear behaviour far from the CNP due to scattering with charged impurities [41]. Up to 2 x 10^{15} ion/cm^2 the drain current decreased with dose with well-defined NP. However, above 2 x 10^{15} ion/cm^2(Figure 6.6) the device no longer displays the usual ambipolar Id-Vg curves but rather a flat characteristic on the electron side and a super-linear behaviour in the hole side.

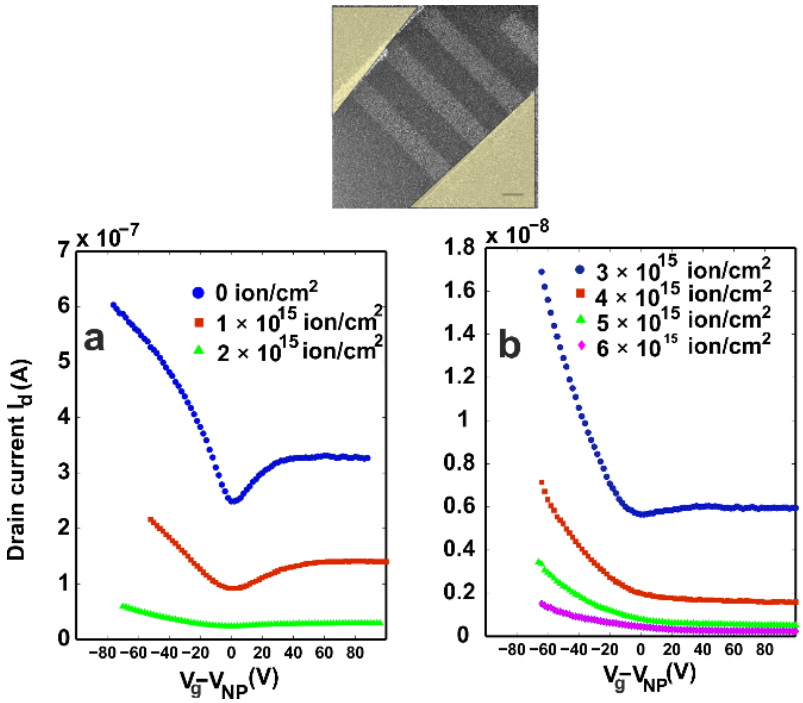

Figure 6.6 a) Id-Vg curves for non-irradiated and moderately irradiated graphene nanoribbons. b) Id-Vg curves for heavily disordered graphene resulting from applied large doses. Here the drain voltage is Vd = 5 mV. Top image: highly irradiated graphene nanoribbons used in the current experiment. The false-colour areas are the metal contacts. The scale bar is 200 nm.

This behaviour becomes pronounced as the dose increases. A decrease in the drain current is also noticeable to a level of few tens of pA for largest dose of 6 x 10^{15} ion/cm^2. We calculate the field effect mobility μ from the transconductance:

$$g_m = \left.\frac{\partial I_d}{\partial V_g}\right|_{V_{d=const}} = -\left(\frac{W}{L}\right).\mu.C_g.(V_g - V_{CNP}), \qquad \textbf{6.2}$$

where C_g is the capacitance per unit area is while W and L are the width and the length of the channel, respectively, while V_{NP} is the voltage at the neutrality point. In Figure 6.7 the electron and hole mobility are plotted as a function of the irradiation dose for a set of

V_g. The mobility decreases abruptly from irradiation dose of 2×10^{15} cm^{-2} which separates a conductive phase from an insulating phase. For instance, the electron mobility dropped by more than five orders of magnitude for the largest dose, from its value corresponding to a non-irradiated channel.

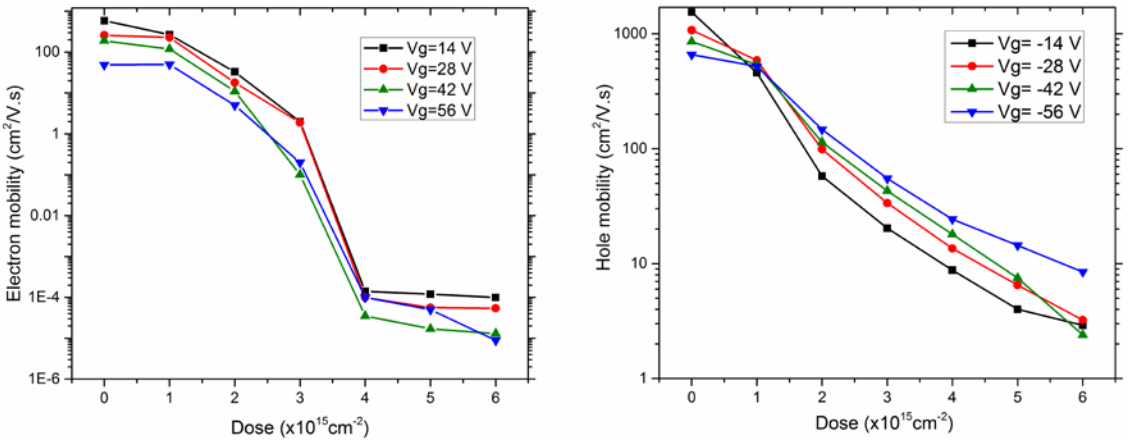

Figure 6.7 Logarithmic scale electron (left) and hole (right) mobility versus irradiation dose for several values of the gate voltage.

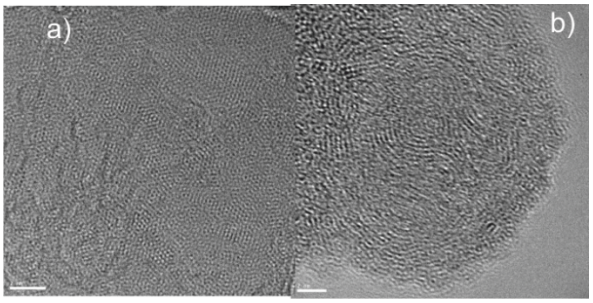

Figure 6.8 TEM images of non-irradiated (a) and irradiated (b) CVD graphene showing different atomic arrangement for irradiated graphene. This image was taken at moderate dose (~10^{14}cm^{-2}). The scale bar is 2 nm.

To gain more information about the atomic structure of irradiated graphene, a suspended CVD graphene sheet irradiated by my colleague Mr. Jamie Reynolds was sent to our collaborators at JAIST for TEM imaging[179]. The result is shown in Figure 6.8 where a clear difference in atomic arrangement is observed. Irradiated graphene loses its crystallinity and atoms rearrange themselves into more amorphous-like structure. This observation correlates well with our transport measurements, which are also consistent with theoretical predictions where quantum interferences and Anderson localization dominate the carrier transport in highly disordered graphene [4].

We conclude that irradiated graphene manifests as insulator when irradiated above certain levels of dose. TEM images show that irradiated graphene becomes a highly disordered two-dimensional carbon network where Anderson localization may be responsible for the insulating behaviour.

6.4 Signature of localisation

Anderson localization, also known as strong localization, is the absence of diffusive propagation of electrons in highly disordered medium, where the electron wave function localizes rather than propagating causing the increase in the resistivity. It has been widely observed that low dimension carbon materials that are subject to high level irradiation can enter the strong Anderson localization regime showing a decrease in conductivity and a further metal-insulator transition (MIT) [13,180,181]. In particular, the localized density of states (LDOS) at the edges is the possible cause of conductivity scaling in GNR[181]. In our case, GNRs bombarded by helium ions becomes insulating as a result of highly disordered edge and high defect density in the channel.

Here we extracted the localization length change by monitoring the conductance as a function of the channel lengths. Multi-terminal GNRs (see Figure 6.9) of different widths and lengths are fabricated using EBL based methods. The non-invasive four-probe configuration rules out the contact resistance allowing for more accurate measurement [182]. The channel length is varied by using probes locating at different points on the GNR. Here we denoted the three lengths on one GNR by L_1, L_2, and L_3. The measurement is carried out on one GNR with width of 1 μm, length L_1 = 500nm, L_2 = 1μm and L_3 = 2.3μm.

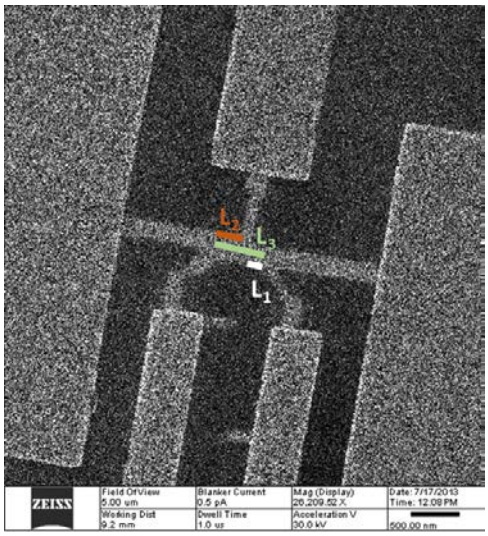

Figure 6.9 HIM image of a smaller five-terminal GNR, where L_1 = 100 nm (white), L_2 = 200 nm(red) and L_3 = 400 nm(green). Scalebar = 500 nm

Resistance was measured prior to and after the irradiation (Figure 6.10). Although there are only three lengths, the data at different hole concentrations (n_p) can be fitted well with an exponential decay, i.e. $G \sim e^{-L/\xi}$, where ξ is localization length and can be extracted by fitting (Figure 6.10). The exponential behaviour for non-irradiated sample suggests that the sample was already in strong localisation regime possibly due to the resist residue and moisture from the ambience. The localisation length of the non-exposed GNR has a value of $\xi = 2.1$ µm at $n_p = 2 \times 10^{12}$ cm^{-2}, and for the exposed GNR, $\xi =$ 1.82 µm at same concentration.

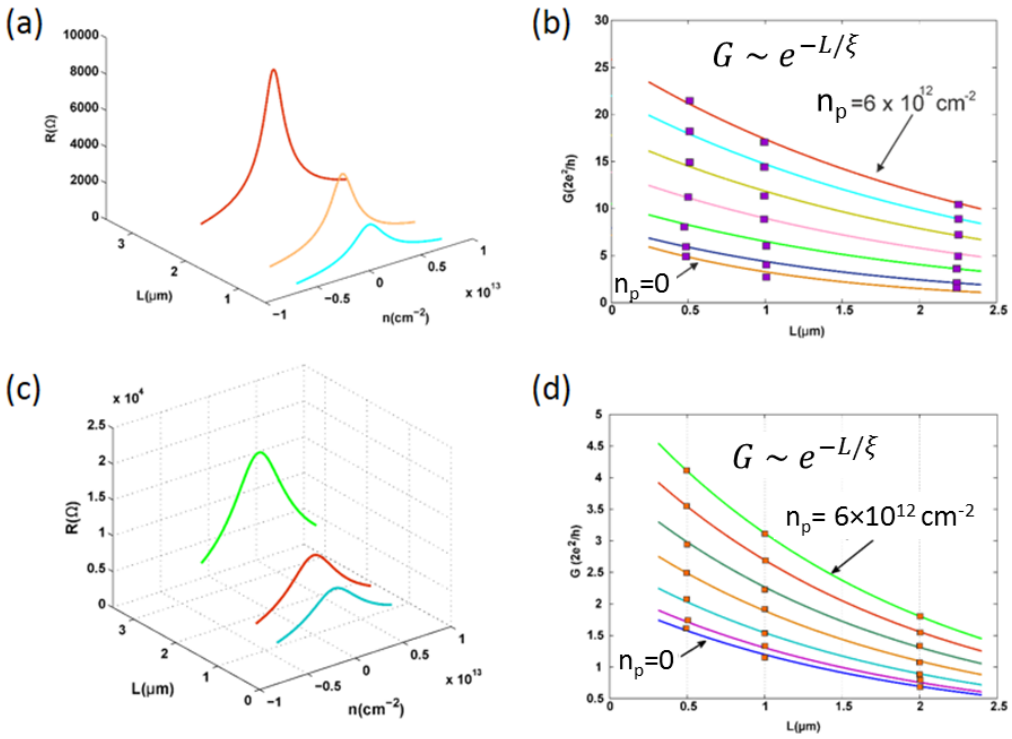

Figure 6.10 Resistance measured before (a) and after (c) irradiation as a function of carrier density for GNRs with various lengths. (b) Conductance measured before irradiation plotted as a function of channel length at different hole concentrations. The solid colour lines are fitted with an exponential function. (c) Resistance of the same GNR after helium irradiation (dose = 1x10^{15} cm^{-2}) as a function of carrier density for GNRs with various lengths. (d) Conductance measured after irradiation (dose = 1x10^{15} cm^{-2}) plotted as a function of channel length at different hole concentrations. The solid colour lines are fitted with an exponential function.

The sample was exposed further to a total dose of 2×10^{15} cm^{-2}. The conductance show a strong suppression of the ambipolar characteristics in the electron branch (Figure 6.11(a)), which is consistent with the findings stated in the section 6.2. Apart from a decrease in mobility, ξ was found to increase with n_p. The extracted ξ versus n_p for three level irradiation are plotted in Figure 6.11 (b). The localisation length ξ slightly increases with n_p for both non-irradiated and irradiated sample. Counter-intuitively, the device irradiated with 1×10^{15} cm^{-2} shows smaller ξ than the non-irradiated sample. This is because the initial irradiation actually cleans the sample surface before damaging the graphene itself. For the dose of 2×10^{15} cm^{-2} it also increases with hole density (n_p). As the neutrality point is not well defined for the third dose, the localisation length is plotted as a function of the gate voltage in Figure 6.11 (c). The monotonic increase of ξ with n_p may be explained by the screening of potential well near the defects by holes. However, more work is needed to investigate this relationship in more detail.

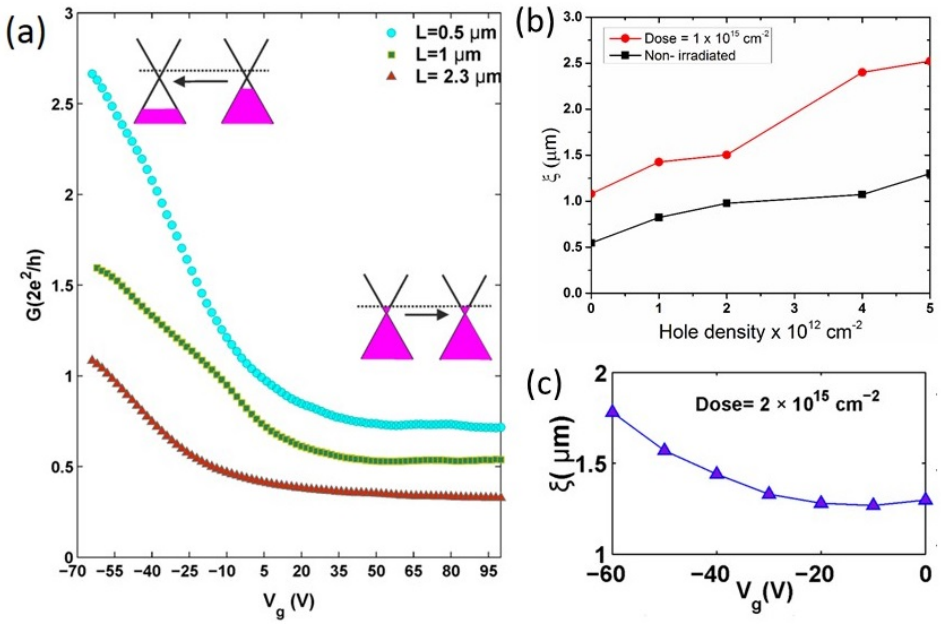

Figure 6.11 (a) Conductance versus the gate voltage for exposed multi-probe nanowires for different lengths (width = 1 um) with a dose of 2×10^{15} cm^{-2}. These characteristics are different from the typical graphene ones. They show a conduction band pinned Fermi level which results from high density of defects induced by irradiation. (b) Localisation length plotted as function of hole density for samples before and after irradiation. (c) Localisation length plotted as function of gate voltage for dose of 2×10^{15} cm^{-2}

6.5 X-ray photoelectron spectroscopy analysis

In order to explain the origin of the transport behaviour of our irradiated devices described in section 6.2, 6.3 and 6.4, in particular, the suppression of ambipolar behaviour, we proposed a scenario based on the pinning of graphene's Fermi level (Figure 6.12). The flatness of electron branch observed in our iGNR devices indicates large density of states near the Dirac point and consequent Fermi level pinning. This can possibly be attributed to the unsaturated dangling bonds due to irradiation.

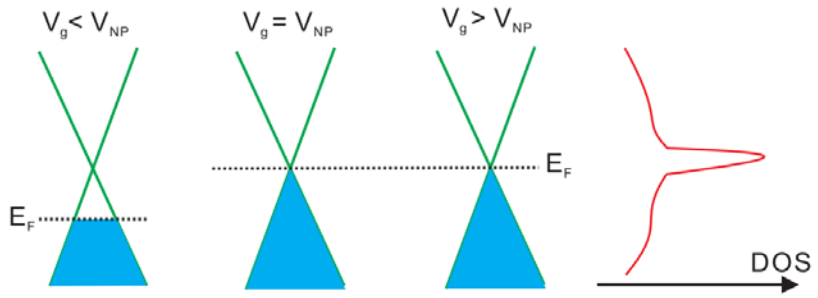

Figure 6.12 Proposed band-structure of our iGNR devices. Fermi level pinnng is attributed to large DOS near the Dirac point.

In order to verify our hypothesis, X-ray photoelectron spectroscopy (XPS) was employed. The XPS measures the chemical composition of a material, which can be used as a complementary method to examine the bond changes in irradiated graphene. This work was primarily conducted by Dr. Zakaria Moktadir, the first author of reference [183].

The XPS measurement was performed on a transferred CVD graphene sample which was freshly transferred onto Si/SiO2 substrate, using a Theta Probe Angle-Resolved X-ray Photoelectron Spectrometer, from Thermo Scientific^{TM}[183]. The system uses a monochromatic, micro-focused Al K-Alpha source delivering a spot size between 15 µm and 400 µm. For our samples a spot size of 100 µm was chosen for optimum measurements. The graphene was divided into small square areas and each of them was irradiated in HIM with increasing dose from 1 to 6×10^{15} cm^{-2} in steps of 1×10^{15} cm^{-2}.

A survey across binding energy [0, 1200] eV identified the different atomic species in the sample: oxygen, silicon and carbon. The former two are due to the SiO_2 substrate. Figure 6.13 shows the C1s core level spectrum for different defect concentrations. The spectrum was fitted with Gaussian and Lorentzian peaks corresponding to three chemical bonds: C-C (284.4 eV), C-O (286 eV) and C=O (288.5 eV). Note that although the C1s core level binding energy varies depending on the substrate material for up to hundreds meV, we used the value for graphite for the sp2 line, i.e. 284.4 eV as a reference. As defect density increases, the FWHM of this main peak broadens.

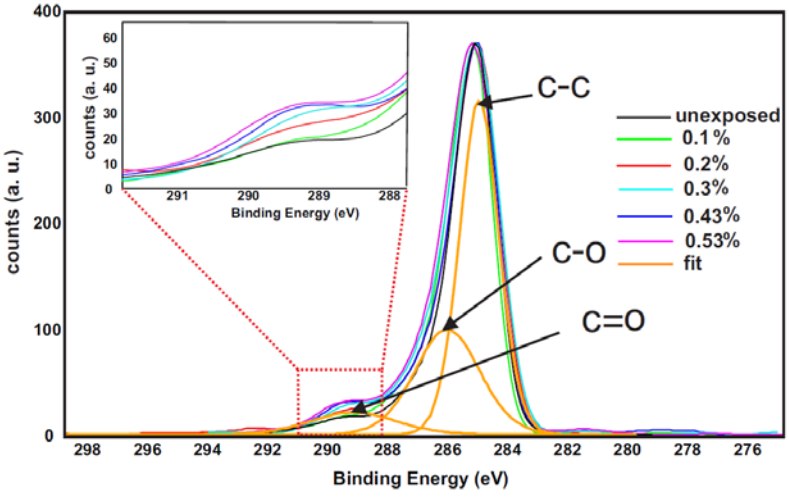

Figure 6.13 XPS spectrum of C1s core level for different defect concentrations. Inset shows the close-up of spectrum near 288 eV.

The sp3 to sp2 ratio can be determined by the D-parameter which is the distance between the Auger electron 1st derivative spectrum's minimum and maximum[184]. The D-

parameter has a value of 21 eV for graphite (only sp2) and 13 eV for diamond (sp3). It was found out to be ~18 eV for the both non-irradiated and irradiated samples which however, did not vary much for the range of defect densities in our study. Neither can our XPS spectrum be able to resolve the tiny shift of C1s level for different types of defects such as single vacancy (-0.64 eV), double vacancy (-0.49 eV) and Stone-Wales defect (-0.34 eV), as predicted by previous DFT calculations[185]. This might be due to the fact that the dangling bonds were already largely saturated in the air during the transfer from the high vacuum chamber of HIM to the XPS. The measured D-parameter also suggests the presence of sp3 component which is attributed to out-of-plane structures and are mainly oxygen groups attached to the dangling bonds induced by defects, as observed in the XPS spectrum. Further improvement on experimental procedure such as introducing *in-situ* bond-termination with hydrogen gas is needed to investigate the problem fully.

6.6 Temperature dependence measurement

One of the major challenges in modern electronics is the reduction of power consumption. Many device-level solutions have been proposed, among which single electron transistor (SET) realised in semiconductor quantum dots is a promising platform owing to its capability of transporting individual electron due to Coulomb blockade[186,187]. One important component of an SET is a tunnel barrier, which is the energy barrier that limits the current flow. Graphene is also a candidate in this direction owing to the long spin coherence time in carbon atoms[25,188]. Lithographically defined graphene SET has been demonstrated, however the downscaling remains a challenge since the etching process results in very random edge disorder. Here we proposed a tunnel barrier formation method based on irradiation-induced metal-insulator transition which have been discussed in previous sections. The device schematic is shown in Figure 6.14 where the whole channel is covered with polymer layer but a small opening. By using modern EBL patterning, the gap width can be well defined. The channel is subsequently irradiated with helium ions. This effectively creates an insulating region in the channel which act as a tunnel barrier. By fabricating multiple barriers, one can produce more elaborated structures such as a quantum dot with at least two barriers. The advantage of our device is that the graphene underneath the polymer mask is well protected from undesired ion bombardment. The primary parameters of interest are the gap width and irradiation dose.

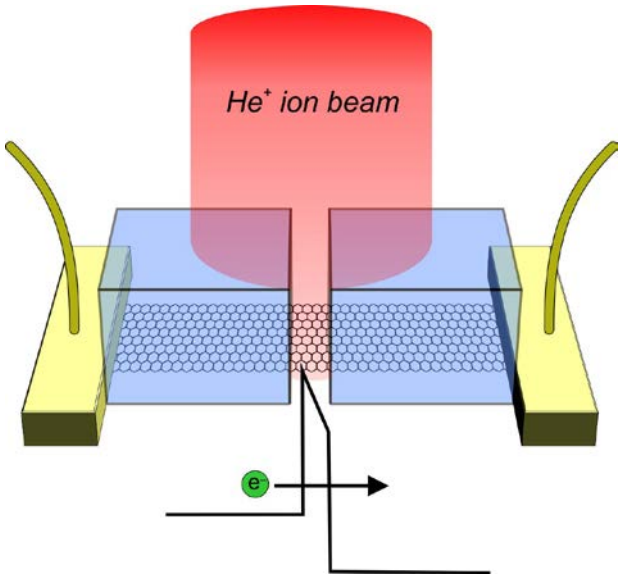

Figure 6.14 Device Schematics. The GNR is covered with polymeric mask (light blue) except a small opening is exposed to helium ion beam.

A pair of as-fabricated devices prior to irradiation is shown in Figure 6.15 where the graphene channel is covered with 300 nm thick PMMA protection layer. The resist layer should be thick enough to stop most of the incident helium ions but thin enough to retain the minimum feature size, hence why we choose 300nm as the PMMA thickness. The HIM irradiation process is shown in Figure 6.16 where the yellow rectangle depicts the irradiation pattern and the dark region indicates the PMMA due to charging.

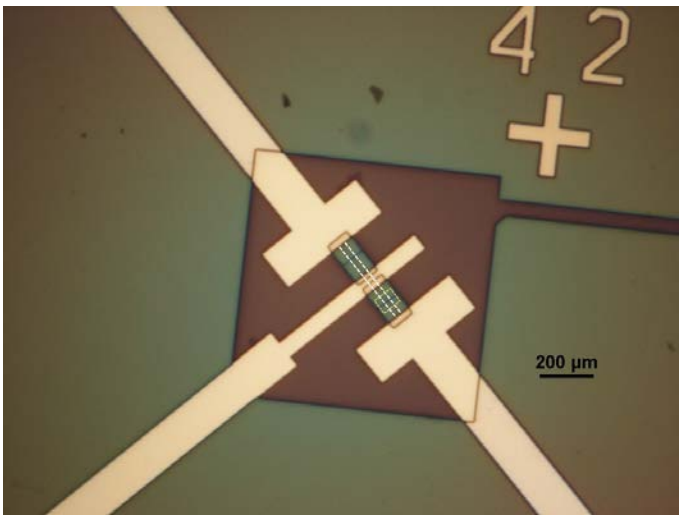

Figure 6.15 A pair of as-fabricated iGNR devices. The graphene channel is outlined by white dashed lines.

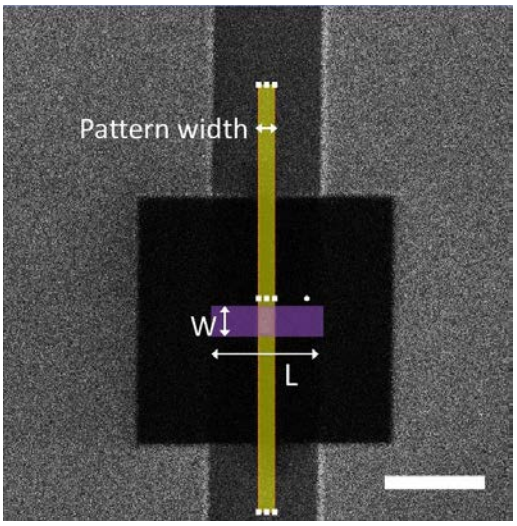

Figure 6.16 The helium ion irradiation on the exposed channel. The images shows the area outlined by the yellow dashed box in Figure 6.15. The graphene channel is indicated by violet rectangle with length L and width W. The irradiation channel is indicated by the yellow vertical bar. Scalebar is 2 µm.

Two single layer devices, labelled device 1 and device 2 have been irradiated with different dose sets: $n\times10^{15}$ cm^{-2} (n = 1, 2, 3, 4, 5) and $n\times10^{16}$ cm^{-2} (n = 1, 2, and 3), respectively. This means Stage 2 disorder should be created for both cases[38]. The defect levels corresponding to theses doses can be roughly estimated by assuming a linear dependency of defect density on irradiation dose and estimated the defect density for each device 1 and device 2 to be n×0.068% (n = 1-5) and n×0.68%(n = 1-3), respectively. The irradiation pattern width on device 1 and device 2 are 200nm and 50nm, respectively. The dimension of device 1 and device 2 is $L = 2.5$ µm, $W = 0.5$ µm.

We first monitored I_d-V_d for device 1 and device 2 at room temperature after each irradiation, as shown in Figure 6.17 and Figure 6.18, respectively. Although the I_d-V_d measurement for the pre-irradiated sample and first irradiation run did not extend to large V_d range, it can be seen that I_d is very linear. The non-linearity of the I_d-V_d curve increases with increasing defect concentration, which can even be seen at voltage range below 1V. The observation of non-linearity is the first step towards observing quantum tunnelling[135,189]. However, we did not see significant suppression of current at low V_d at room temperature. Note that sweeping across large V_d effectively provides current annealing for our device improving both metal-graphene contact and surface cleanness. The non-linear I_d-V_d characteristic without I_d suppression also indicates no current-induced rupture of the GNR which may form unintentional quantum dots[190].

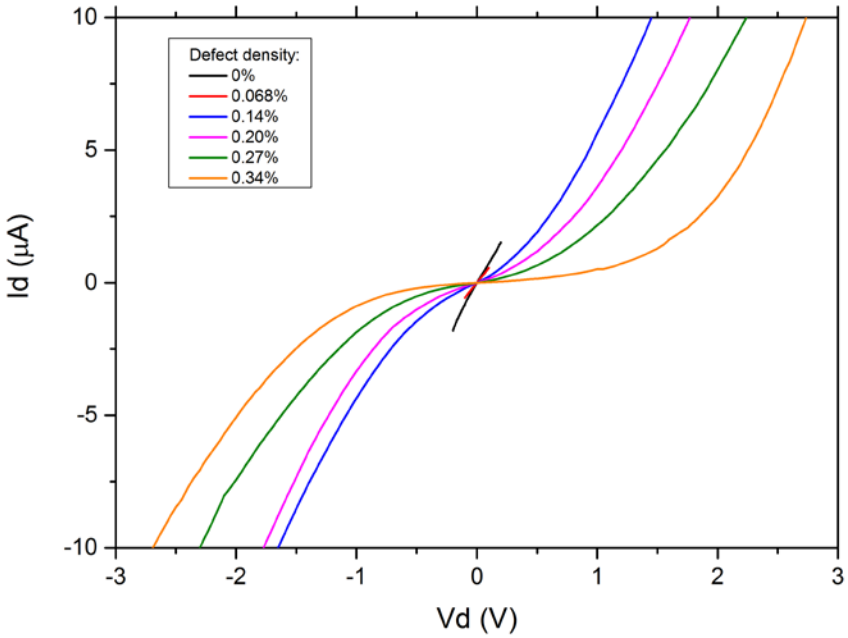

Figure 6.17 Id-Vd characteristic of device 1 at increasing defect densities.

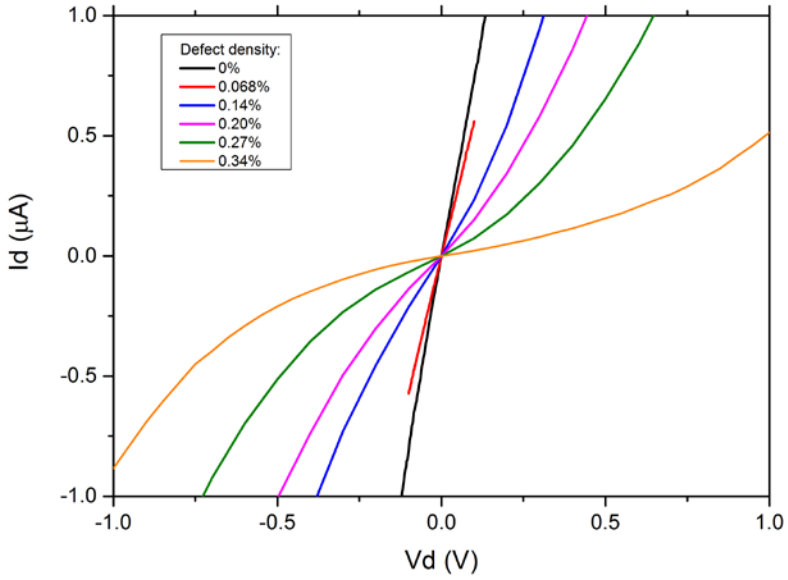

Figure 6.18 Id-Vd characteristic of device 2 at increasing defect densities.

We subsequently conducted temperature dependence measurement on the two irradiated devices down to 4.2 K. The measurement was conducted in a fully sealed vacuum chamber (~10^{-8} kPa) in a cryogenic prober (see Figure 6.19). The sample was loaded at least one night prior to measurement allowing for full desorption of surface impurities.

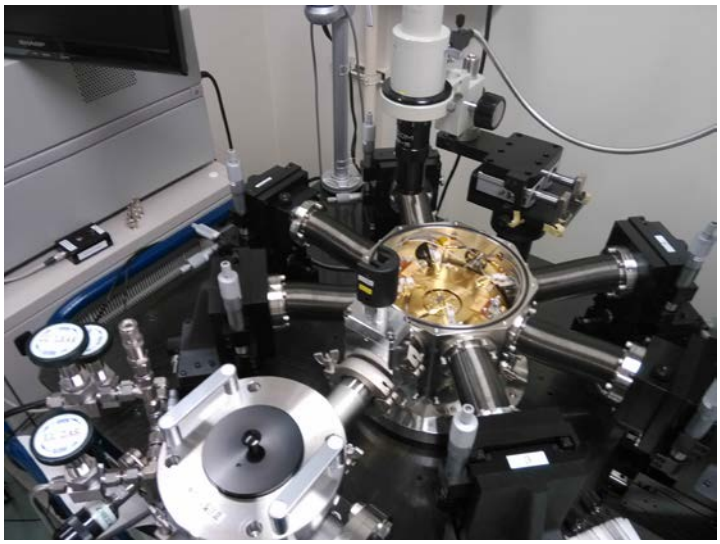

Figure 6.19 The cryogenic probe station used for this experiment.

The logarithmic-scale conductivity of device 1 and device 2 is plotted in Figure 6.20 and Figure 6.21, respectively. The conductance saturates at a finite value of ~37 nS and ~30 nS for device 1 and device 2, respectively. Since no suppression of conductivity at low temperature, no strong localisation is probed at the present device. We attributed the absence of localisation to the limited pattern width we used for HIM irradiation which has generated a significantly smaller amount of defects compared the case described in section 6.4 where the whole graphene channel was irradiated. Similar temperature dependence was observed on device 2. Device 2 was irradiated in the same manner except that the exposure area was only 50 nm wide but with a ten times higher dose.

The conductance of the irradiated GNR can consists of two parts: band conduction and hopping conduction. The former is facilitated by carriers excited across the mobility edge[191] into non-localised states and usually is dominant at high temperature (i.e., thermal activation), while the latter is by carriers excited into localised states via hopping and is the main mechanism at low temperature[192]. These two mechanisms dominate at different temperature range and contribute in parallel[193,194] to the conductance. We first extracted the activation energy E_A by fitting the conductance with the thermal activated transport scheme $G \propto exp\,(-\frac{E_A}{2k_BT})$ from 71 K to 295 K, where k_B is Boltzmann's constant and E_A is the activation energy. We obtained the value of E_A by the following relation:

$$\frac{dln(G)}{d(1/T)} = -\frac{E_A}{2k_BT}, \qquad \textbf{6.3}$$

where $\frac{dln(G)}{d(1/T)}$ is the slope of the *ln(G)* v.s. *(1/T)* plot. E_A was 10 meV and 11 meV for device 1 and device 2, respectively.

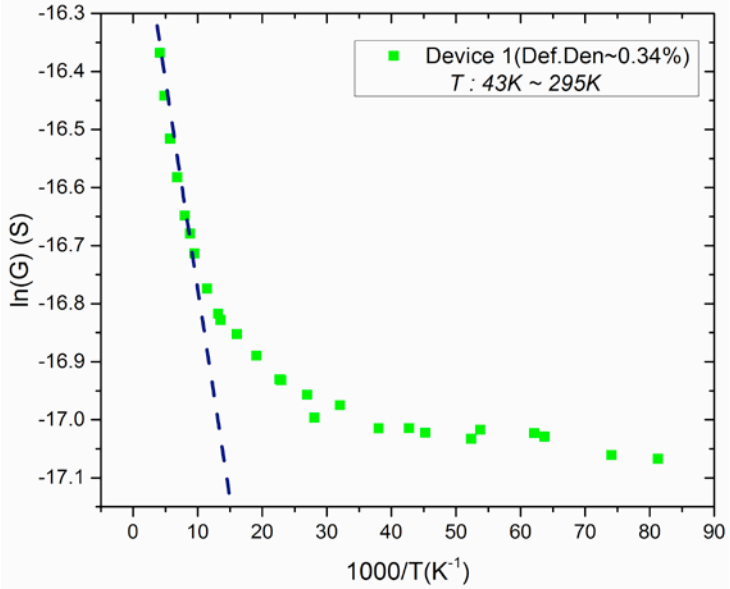

Figure 6.20 *ln(G)* as a function of 1000/*T* for device 1. The dashed line shows the linear fitting of thermal activation model on temperature range 105 *K*<*T*<240 K

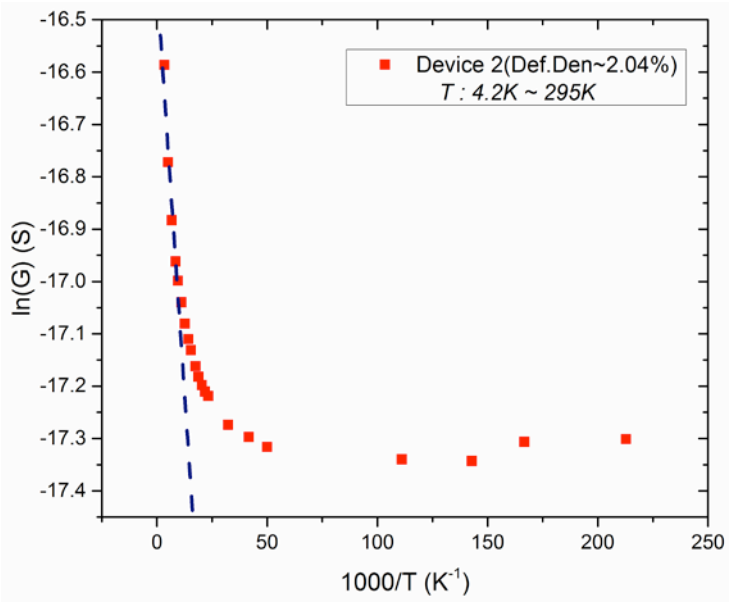

Figure 6.21 ln(G) as a function of 1000/T for device 2. The dashed line shows the linear fitting of thermal activation model on temperature range 105 K<T<295 K

The conduction of highly disordered material at low temperature can be described by variable range hopping (VRH)[195], in which the tunnelling of carriers between localised

states is dominantly responsible for the conduction. In particular, VRH conduction was observed in a wide range of disordered graphene samples including reduced graphene oxide(rGO)[196,197], hydrogenated graphene[95,198] , bilayer graphene[193,199] and irradiated graphene[13,200]. In the limit of zero bias, the hopping process is essentially phonon-assisted tunnelling where the energy is provided by phonons which is dependent on temperature. The hopping conductance is given as follows:

$$G = G_0 exp\left(-\left(\frac{T_0}{T}\right)^p\right), \qquad \textbf{6.4}$$

where G_0 is a weak T-dependent pre-factor, T_0 is a characteristic temperature (so-called "*Mott* coefficient") and p is the exponent which differs depending on hopping mechanisms. In "Mott-VRH", $p = 1/1+D$, where D is the dimension of the system. For 2D system $p = 1/3$ and $T_0 = \frac{13.8}{k_B g_F \xi^2}$, where k_B is Boltzmann constant, g_F is the constant density of states (DOS) near Fermi level and ξ is the localisation length. Efros and Shklovskii [201]pointed that at low-enough temperature $p = 1/2$ for all dimensions as a result of vanishing DOS at Fermi level due to Coulomb electron-hole interaction. In this so-called "ES-VRH", $T_0 = \frac{6.2e^2}{4\pi\varepsilon_0 \varepsilon k_B \xi}$, where $\varepsilon_0, \varepsilon$ are the permittivity of vacuum and relative permittivity of the material (in our case, ε=2.4 for graphene[202]). ES-VRH is dominant if the sample is very disordered due to high Coulomb gap E_{CG}, whereas Mott-VRH is observed if the disorder is relatively low.

The conductance from 43 K to 105 K for both device 1 and 2 deviated from $1/T$ to $(1/T)^p$ which implies VRH conduction over the measured temperature range. We fitted ln(G) with both $T^{-1/3}$(Mott) and $T^{-1/2}$(ES). If Mott-VRH is dominant, the hopping coefficient T_0 is 12.1 K and 16.0 K for device 1 and device 2, respectively. If ES-VRH dominates, T_0 = 17.8 K and 27.54 K for device 1 and device 2, respectively. In either case, device 1 shows a smaller T_0 than device 2. Since T_0 is inversely related to the localisation length ξ, device 1 is more disordered than device 2, which is in accordance to the fact that the irradiation pattern on device 1 is 4 times wider and albeit a stronger dose was delivered to device 2.

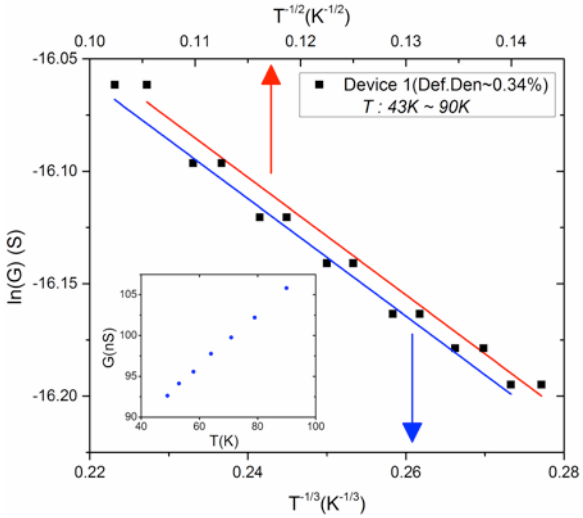

Figure 6.22 ln(G) of device 1 as a functions of $T^{-1/3}$(blue) and $T^{-1/2}$(red) from 43 K to 90 K . Inset shows the *G* vs *T* plot.

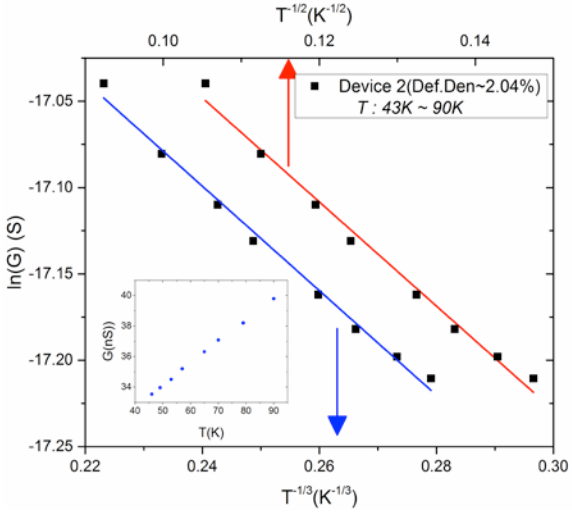

Figure 6.23 ln(G) of device 2 as functions of $T^{-1/3}$(blue) and $T^{-1/2}$(red) from 43 K to 90 K . Inset shows the *G* vs *T* plot.

As can be seen from Figure 6.22 and Figure 6.23, ln(*G*) fits well to both Mott- and ES-VRH, as somewhat expected [95]. In order to differentiate between two mechanisms, a method called resistance curve derivative analysis (RCDA)[203] can be used to explicitly find the exponent *p*. However, this method requires a large change in resistance/conductance with temperature by at least two orders of magnitude, to obtain enough accuracy. However, our data showed fairly moderate change of conductance, therefore the accuracy is limited to some extent. A reduced activation energy *w* is defined as follows:

$$w = \frac{dln(G)}{dln(T)}, \qquad \textbf{6.5}$$

where *G* has the form of 6.4 and subsequently *w* can be expressed as:

$$w = p\times(\frac{T_0}{T})^p, \qquad \textbf{6.6}$$

As a result, p can be found by:

$$p = \frac{dlnw}{dlnT}, \qquad \textbf{6.7}$$

Due to the limited resolution of our data, we could only obtain a ln$w$ versus ln$T$ plot for device 1 and found that $p \approx 0.58$ indicating possible existence of ES-VRH (see Figure 6.24), which was also experimentally observed in disordered graphene samples [95,196].

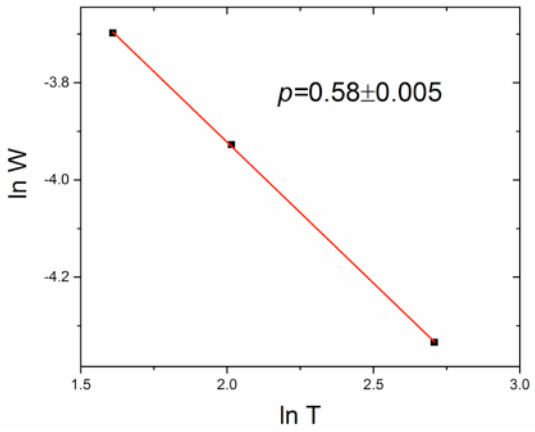

Figure 6.24 ln W versus ln T for device 1

Assuming the ES-VRH, the estimated localisation length ξ is 2.4 μm and 1.6 μm, respectively. This is in good agreement with values obtained from conductivity measurement discussed in 6.2 and indeed suggests that our iGNR is not yet in strong localisation regime. This can also be seen from the saturation of G at temperatures down to 4.2 K where no significant suppression of current was observed, which is expected for graphene with large disorder.

The current shows a transition from linear to non-linear dependence on V_d, i.e., from ohmic to non-ohmic conduction (shown in Figure 6.25) as temperature increases. This implies the interplay of three hopping regimes: thermally assisted VRH, field-assisted thermally activated VRH and field-driven VRH.

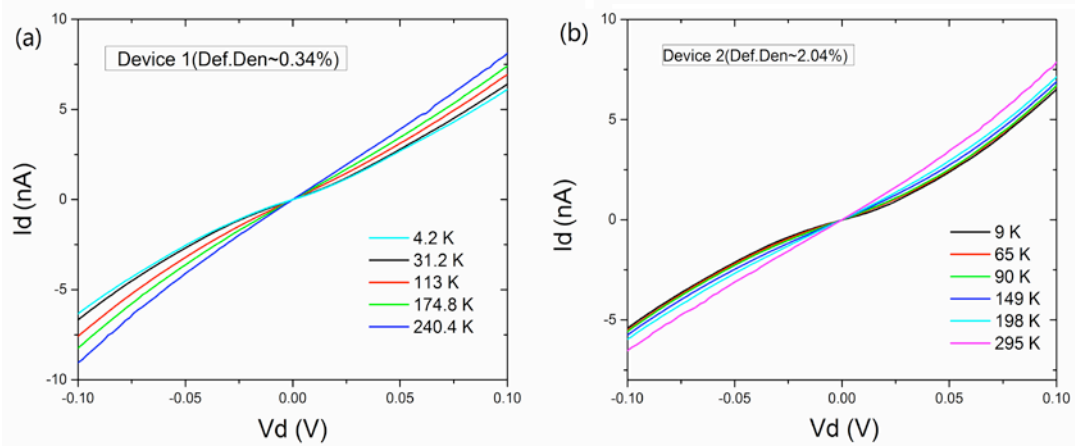

Figure 6.25 Id-Vd plot of device 1(a) and device 2(b)

As the electric field increases to intermediate values, the VRH becomes field-assisted but still thermally activated and is described by the following equation:

$$G(T,E) = G_0 exp\ (-(\frac{T_0}{T})^p) exp(\frac{E}{E_a}), \qquad \textbf{6.8}$$

where G_0 is a pre-factor, E_a is given by $\frac{k_B \mathrm{T}}{0.18\mathrm{r(T)}e}$ where $r(T)$ is the mean hopping distance and e is the elementary charge.

As the electric field further increases, the hopping becomes temperature-independent or "activation-less" where the energy difference is mainly supplied by electric field. Under this regime, the conductance is given by:

$$G(E) = G1 exp(-(\frac{E_0}{E})^s), \qquad \textbf{6.9}$$

where G1 is the pre-factor and E_0 is a field constant linearly related to T_0. The exponent s is usually equal to p in equation 6.8. The crossover between the above-mentioned hopping situations has been studied in detail in reference [204].

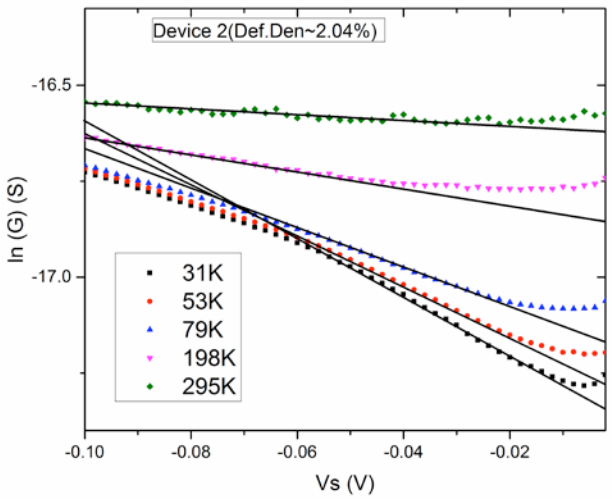

Figure 6.26 ln(*G*) vs *Vs* for device 2 for 31 K, 53 K, 79 K, 198 K and 295 K . Black solid lines denoted linear dependence of ln(*G*) on *Vs* for intermediate voltages.

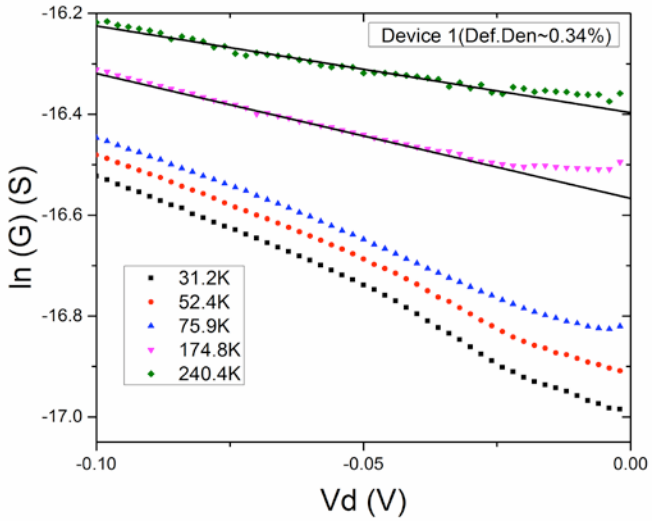

Figure 6.27 ln(*G*) vs *Vs* for device 1 for31 K, 52 K, 76 K, 175 K and 240 K . Black solid lines denoted linear dependence of ln(*G*) on Vs for intermediate voltages.

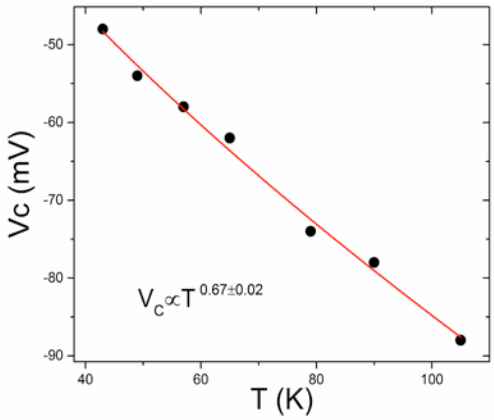

Figure 6.28 The cross-over voltage *Vc* for device 2 as a function of *T*. Solid line is the power fit.

Figure 6.26 and Figure 6.27 show the *Vs*-dependent ln(*G*) of device 1 and 2 for different *T* values. The linear dependence reflects the field-assisted nature of VRH, i.e., the second exponential term in 6.8. Note that at high temperature, thermal activated VRH always dominates such that the linear behaviour remains even at large V_S for *T*>110 K. A transition from field-assisted thermal activated VRH to activationless VRH occurs for relatively low *T* (<79 K) at high field where the ln(*G*) deviates from the linear regions. It can be seen that the *T*-independent activationless VRH is obvious for device 2 whereas conductance remains T dependent for device 1 even at high field. In Figure 6.28, the cross-over voltage V_C of device 2 is plotted against *T* shows a linear trend, which is in good agreement with the criteria for activationless hopping, that is, $E_{C.O.} \equiv k_B T/e\xi$ [197], where $E_{C.O.}$ is the cross-over field . For device 1, $E_{C.O.}$ is much larger indicating a much smaller ξ, reflecting a larger extent disorder caused by irradiation.

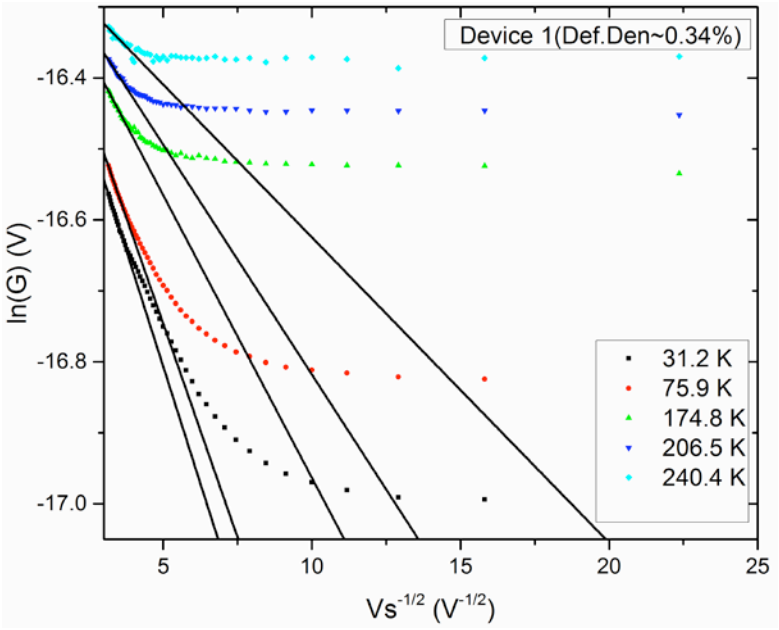

Figure 6.29 ln(*G*) of device 1 as a function of $Vs^{-1/2}$ for 31 K, 76 K, 175 K, 207 K, and 240 K. Solid lines are linear fit over *Vs*>70 mV.

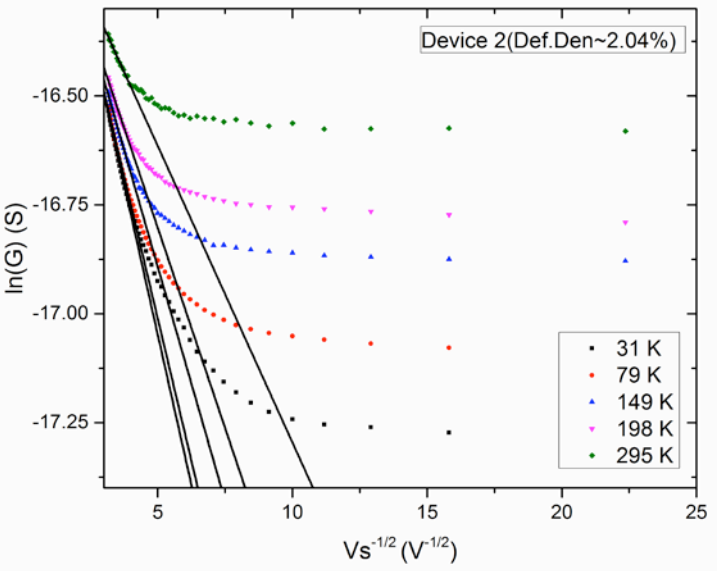

Figure 6.30 ln(*G*) of device 2 as a function of $Vs^{-1/2}$ for 31 K, 79 K, 149 K, 198 K, and 295 K. Solid lines are linear fit over *Vs*>70 mV.

As shown in Figure 6.29, the high-field conductance of highly irradiated device 1 indeed shows the exponential dependence on bias voltage described in equation 6.9 where s = 1/2, indicating the onset of activationless VRH.

6.7 Conclusions

In this chapter, we demonstrated the electrical characteristics of our irradiated graphene nanoribbon devices (iGNR). The simple two-terminal devices showed decrease in conductance mobility with irradiation while the sub-linear to linear transition is attributed to both edge disorder and channel defects. Metal-insulator transition was observed for iGNRs with heavier exposure to helium ions which causes sharp mobility decrease at dose of~2×10^{15} cm^{-2}, which was attributed to amorphisation of carbon network. This was supported by TEM image on irradiated CVD graphene sheet where disordered atomic arrangement was observed. Furthermore, multi-terminal iGNRs showed exponential length-dependence leading to signature of Anderson-like localisation. The estimated localisation length decreased from ~2.1 µm in non-irradiated sample to ~1.8 µm in moderate irradiated sample. The suppression of electron conductance is related to Fermi level pinning. The XPS spectrum implies that the observed Fermi level pinning is possibly due to unsaturated dangling bonds introduced by irradiation. Furthermore, the GNR with irradiation pattern behaves as disordered material with ES-VRH dominated at low temperature. The localisation lengths extracted from hopping temperature showed good agreement with that from length-dependent conductance described above.

Chapter 7 Conclusions and outlook

7.1 Conclusions

Graphene has attracted enormous interests thanks to its extraordinary electronic[2,205,206], optical[207] and mechanical properties[5] since its discovery in 2004[1]. The intrinsic properties of graphene strongly depend on its geometry owing to its unique 2D nature. One notable example is the band-gap engineering on graphene nanoribbons (GNR)[123]. Furthermore, lithographically defined quantum dots are effective structures for building a spin qubit, the building block for quantum information technology[8,22,26,130].

In this thesis, we investigated the defect engineering of graphene by introducing point defects using helium ion irradiation. We first explored the fabrication possibilities with the established e-beam lithography and a new helium ion milling technology, particularly for graphene devices. Extremely small but well-defined structures such as 20 nm quantum dot were illustrated not only as a standalone pattern but also as an integrated device thanks to the hybrid EBL-HIM approach.

We then systematically studied the extent of beam damage in graphene for both irradiation and milling using spatially resolved Raman spectroscopy. The tilt beam created an asymmetric defect landscape where Stage 2 disorder (L_D~1.5 nm) was found along the direction of incidence and Stage 1 disorder (L_D~8.5 nm) on the other side. The damage region spans ~ 300 nm and ~ 250 nm on each side of the milling site. The formation of these regions is attributed to backscattered helium ions and recoil substrate atoms.

Subsequently we studied the electrical properties of defect-embedded graphene devices in order to understand the impact of helium ion irradiation and to explore its applications. Transport measurement of two- and multi-terminal iGNRs were conducted. The observed sub-linear bending in conductivity in iGNRs can be explained by considering both point defects scattering and reduced electron mean free path which is comparable to the channel width. Irradiated GNRs showed dramatic mobility decrease compared to non-irradiated ones indicating a metal-insulator transition (MIT) Another important observation is the increasing unipolar behaviour in the conductance implying the Fermi level pinning for the electron branch. The exponentially length-dependent conductivity of four-terminal iGNR revealed presence of strong localisation. The estimated localisation length decreased from ~2.1 μm in non-irradiated GNR to ~1.8 μm in moderate irradiated GNR. The XPS spectrum implies that the observed Fermi level pinning is possibly due to unsaturated dangling bonds introduced by irradiation. Lastly, the GNR with irradiation pattern behaves as disordered material with ES-VRH dominated at low temperature. The localisation lengths extracted from hopping temperature showed good agreement with that from length-dependent conductance.

In conclusion, the presented work provides knowledge for the characterisation of damage induced in ion-beam associated patterning of graphene, which is essential for the downscaling of electronic, spintronic and quantum devices on 2D materials.

7.2 Future work

The two basic topics discussed in this work are graphene and helium ion fabrication technology. Based on methods and techniques we have developed, it is possible to extend our current research to several other directions. We discuss potential improvement to our current work and then we consider other research topics that may benefit from our results.

7.2.1 Atomic visualisation of irradiated graphene surface

Although the beam-induced damage in irradiated graphene is evident from Raman spectroscopy, the detailed surface landscape is yet directly visualised. With the help of a scan tunnelling microscope (STM), one can obtain more information about the damage in the lattice. To our best knowledge, this type of examination has not been reported. The contribution from various sources, i.e. primary ions, backscattered ions, recoils and etc.

to the damage is still not clear until atomic images are available. This would be greatly beneficial for other supported 2D material platforms.

7.2.2 *In-situ* hydrogenation

It was mentioned in 6.6 that the oxygen group attached to the dangling bond may be the cause of Fermi level pinning, which is generally observed for iGNR devices. In order to avoid such issue, it is desired to immediately saturate the dangling bonds created by beam irradiation with hydrogen atoms. This can be achieved by injecting hydrogen inside the HIM chamber while milling or irradiation is conducted. The proposed approach also minimises the beam-induced deposition of other contaminant.

7.2.3 iGNRs with variable irradiation doses and widths

In section 6.6 only two irradiation widths and five doses were used. A complete study on the width-dose combination of irradiation effect requires a number of values for the irradiation width as well as immediate measurement after each irradiation, which was not possible in our case due to the limitation of experimental set-ups. Future work may include a broader tuning on these parameters.

7.2.4 Other device structures

The hybrid EBL-HIM fabrication method we developed opens possibilities for more advanced device structures such as lithography-defined double quantum dots (DQD), a building block of spin qubit. Our method has already achieved 20nm dot size which surpasses the smallest QD fabricated with EBL [22]. Such quantum dot devices exploits phenomena such as Coulomb blockade and electron tunnelling. The tininess of the structure allows for quantum operations at higher temperature.

Furthermore, our work on irradiation-modified GNRs pave the way for nano-scale defect engineering, which could in turn, benefit many other researches such as quantum electronics, DNA sequencing using nano-pores. However, further work is needed to get better control on delivering the dose to the desired location. Finally, different beam types (e.g. hydrogen, nitrogen etc.) could be employed for different purposes, which is already a topic attracting intensive interests.

Reference

[1] Novoselov KS, Geim AK, Morozov S V., Jiang D, Zhang Y, Dubonos S V., et al. Electric field effect in atomically thin carbon films. Science 2004;306:666–9. doi:10.1126/science.1102896.

[2] Novoselov KS, Geim AK, Morozov S V., Jiang D, Katsnelson MI, Grigorieva I V., et al. Two-dimensional gas of massless Dirac fermions in graphene. Nature 2005;438:197–200. doi:10.1038/nature04233.

[3] Butler SZ, Hollen SM, Cao L, Cui Y, Gupta J a., Gutiérrez HR, et al. Progress, challenges, and opportunities in two-dimensional materials beyond graphene. ACS Nano 2013;7:2898–926. doi:10.1021/nn400280c.

[4] Bolotin KI, Sikes KJ, Hone J, Stormer HL, Kim P. Temperature-Dependent Transport in Suspended Graphene. Phys Rev Lett 2008;101:096802. doi:10.1103/PhysRevLett.101.096802.

[5] Lee C, Wei X, Kysar JW, Hone J. Measurement of the elastic properties and intrinsic strength of monolayer graphene. Science 2008;321:385–8. doi:10.1126/science.1157996.

[6] Balandin A a., Ghosh S, Bao W, Calizo I, Teweldebrhan D, Miao F, et al. Superior thermal conductivity of single-layer graphene. Nano Lett 2008;8:902–7. doi:10.1021/nl0731872.

[7] Murali R, Yang Y, Brenner K, Beck T, Meindl JD. Breakdown current density of graphene nanoribbons. Appl Phys Lett 2009;94:2007–10. doi:10.1063/1.3147183.

[8] Trauzettel B, Bulaev D V., Loss D, Burkard G. Spin qubits in graphene quantum dots. Nat Phys 2007;3:192–6. doi:10.1038/nphys544.

[9] Meyer JC, Kisielowski C, Erni R, Rossell MD, Crommie MF, Zettl a. Direct imaging of lattice atoms and topological defects in graphene membranes. Nano Lett 2008;8:3582–6. doi:10.1021/nl801386m.

[10] Banhart F, Kotakoski J, Krasheninnikov A V. Structural defects in graphene. ACS Nano 2011;5:26–41. doi:10.1021/nn102598m.

[11] Ni ZH, Ponomarenko L a., Nair RR, Yang R, Anissimova S, Grigorieva I V., et al. On resonant scatterers as a factor limiting carrier mobility in graphene. Nano Lett 2010;10:3868–72. doi:10.1021/nl101399r.

[12] Chen J-H, Cullen WG, Jang C, Fuhrer MS, Williams ED. Defect Scattering in Graphene. Phys Rev Lett 2009;102:10–2. doi:10.1103/PhysRevLett.102.236805.

[13] Nakaharai S, Iijima T, Ogawa S, Suzuki S, Li S, Tsukagoshi K. Conduction Tuning of Graphene Based Defect-induced Localization. ACS Nano 2013;7:5694–700.

[14] Van Tuan D, Kotakoski J, Louvet T, Ortmann F, Meyer JC, Roche S. Scaling properties of charge transport in polycrystalline graphene. Nano Lett 2013;13:1730–5. doi:10.1021/nl400321r.

[15] Gunlycke D, White CT. Graphene Valley Filter Using a Line Defect. Phys Rev Lett 2011;106:136806. doi:10.1103/PhysRevLett.106.136806.

[16] Kurasch S, Kotakoski J, Lehtinen O, Skákalová V, Smet J, Krill CE, et al. Atom-by-atom observation of grain boundary migration in graphene. Nano Lett 2012;12:3168–73. doi:10.1021/nl301141g.

[17] Kotakoski J, Mangler C, Meyer JC. Imaging atomic-level random walk of a point defect in graphene. Nat Commun 2014;5:3991. doi:10.1038/ncomms4991.

[18] Cretu O, Krasheninnikov A V., Rodríguez-Manzo J a., Sun L, Nieminen RM, Banhart F. Migration and localization of metal atoms on strained graphene. Phys Rev Lett 2010;105:1–4. doi:10.1103/PhysRevLett.105.196102.

[19] Kotakoski J, Meyer JC, Kurasch S, Santos-Cottin D, Kaiser U, Krasheninnikov a. V. Stone-Wales-type transformations in carbon nanostructures driven by electron irradiation. Phys Rev B 2011;83:245420. doi:10.1103/PhysRevB.83.245420.

[20] Yazyev O V., Tavernelli I, Rothlisberger U, Helm L. Early stages of radiation damage in graphite and carbon nanostructures: A first-principles molecular dynamics study 2007:5. doi:10.1103/PhysRevB.75.115418.

[21] Lahiri J, Lin Y, Bozkurt P, Oleynik II, Batzill M. An extended defect in graphene as a metallic wire. Nat Nanotechnol 2010;5:326–9. doi:10.1038/nnano.2010.53.

[22] Ponomarenko LA, Schedin F, Katsnelson MI, Yang R, Hill EW, Novoselov KS, et al. Chaotic Dirac billiard in graphene quantum dots. Science 2008;320:356–8. doi:10.1126/science.1154663.

[23] Molitor F, Dröscher S, Güttinger J, Jacobsen A, Stampfer C, Ihn T, et al. Transport through graphene double dots. Appl Phys Lett 2009;94:222107. doi:10.1063/1.3148367.

[24] Neumann C, Volk C, Engels S, Stampfer C. Graphene-based charge sensors. Nanotechnology 2013;24:444001. doi:10.1088/0957-4484/24/44/444001.

[25] Wang L-J, Cao G, Tu T, Li H-O, Zhou C, Hao X-J, et al. A graphene quantum dot with a single electron transistor as an integrated charge sensor. Appl Phys Lett 2010;97:262113. doi:10.1063/1.3533021.

[26] Connolly MR, Chiu KL, Giblin SP, Kataoka M, Fletcher JD, Chua C, et al. Gigahertz quantized charge pumping in graphene quantum dots. Nat Nanotechnol 2013;8:417–20. doi:10.1038/nnano.2013.73.

[27] Bischoff D, Varlet a, Simonet P, Ihn T, Ensslin K. Electronic triple-dot transport through a bilayer graphene island with ultrasmall constrictions. New J Phys 2013;15:083029. doi:10.1088/1367-2630/15/8/083029.

[28] Han MY, Brant JC, Kim P. Electron Transport in Disordered Graphene Nanoribbons. Phys Rev Lett 2010;104. doi:10.1103/PhysRevLett.104.056801.

[29] Kalhor N, Boden SA, Mizuta H. Sub-10 nm patterning by focused He-ion beam milling for fabrication of downscaled graphene nano devices. Microelectron Eng 2014;114:70–7. doi:10.1016/j.mee.2013.09.018.

[30] Abbas AN, Liu G, Liu B, Zhang L, Liu H, Ohlberg D, et al. Patterning, characterization, and chemical sensing applications of graphene nanoribbon arrays down to 5 nm using helium ion beam lithography. ACS Nano 2014;8:1538–46. doi:10.1021/nn405759v.

[31] Fox D, Chen Y, Faulkner CC, Zhang H. Nano-structuring , surface and bulk modification with a focused helium ion beam 2012:579–85. doi:10.3762/bjnano.3.67.

[32] Bell DC, Lemme MC, Stern LA, Williams JR, Marcus CM. Precision cutting and patterning of graphene with helium ions. Nanotechnology 2009;20:455301. doi:10.1088/0957-4484/20/45/455301.

[33] Fox DS, Zhou Y, Maguire P, O'Neill A, Ó'Coileáin C, Gatensby R, et al. Nanopatterning and Electrical Tuning of MoS_2 Layers with a Subnanometer Helium Ion Beam. Nano Lett 2015:150715144824008. doi:10.1021/acs.nanolett.5b01673.

[34] Boden S a., Moktadir Z, Bagnall DM, Mizuta H, Rutt HN. Focused helium ion beam milling and deposition. Microelectron Eng 2011;88:2452–5. doi:10.1016/j.mee.2010.11.041.

[35] Lemme MC, Bell DC, Williams JR, Stern LA, Baugher BWH, Jarillo-Herrero P, et al. Etching of graphene devices with a helium ion beam. ACS Nano 2009;3:2674–6. doi:10.1021/nn900744z.

[36] Fischbein MD, Drndić M. Electron beam nanosculpting of suspended graphene sheets. Appl Phys Lett 2008;93:113107. doi:10.1063/1.2980518.

[37] Liu X, Xu T, Wu X, Zhang Z, Yu J, Qiu H, et al. Top-down fabrication of sub-nanometre semiconducting nanoribbons derived from molybdenum disulfide sheets. Nat Commun 2013;4:1776. doi:10.1038/ncomms2803.

[38] Fox D, Zhou YB, O'Neill A, Kumar S, Wang JJ, Coleman JN, et al. Helium ion microscopy of graphene: beam damage, image quality and edge contrast. Nanotechnology 2013;24:335702. doi:10.1088/0957-4484/24/33/335702.

[39] Castro Neto a. H, Peres NMR, Novoselov KS, Geim AK. The electronic properties of graphene. Rev Mod Phys 2009;81:109–62. doi:10.1103/RevModPhys.81.109.

[40] Wallace P. The Band Theory of Graphite. Phys Rev 1947;329.

[41] Das Sarma S, Adam S, Hwang E, Rossi E. Electronic transport in two-dimensional graphene. Rev Mod Phys 2011;83:407–70. doi:10.1103/RevModPhys.83.407.

[42] Hwang EH, Adam S, Das Sarma S, Sarma S. Carrier Transport in Two-Dimensional Graphene Layers. Phys Rev Lett 2007;98:186806. doi:10.1103/PhysRevLett.98.186806.

[43] Chen J-H, Jang C, Ishigami M, Xiao S, Cullen WG, Williams ED, et al. Diffusive charge transport in graphene on SiO2. Solid State Commun 2009;149:1080–6. doi:10.1016/j.ssc.2009.02.042.

[44] Ishigami M, Chen JH, Cullen WG, Fuhrer MS, Williams ED. Atomic structure of graphene on SiO2. Nano Lett 2007;7:1643–8. doi:10.1021/nl070613a.

[45] Chen J-H, Jang C, Xiao S, Ishigami M, Fuhrer MS. Intrinsic and extrinsic performance limits of graphene devices on SiO2. Nat Nanotechnol 2008;3:206–9. doi:10.1038/nnano.2008.58.

[46] Ando T. Screening Effect and Impurity Scattering in Monolayer Graphene. J Phys Soc Japan 2006;75:074716. doi:10.1143/JPSJ.75.074716.

[47] Nomura K, MacDonald a. H. Quantum Transport of Massless Dirac Fermions. Phys Rev Lett 2007;98:076602. doi:10.1103/PhysRevLett.98.076602.

[48] Adam S, Hwang EH, Galitski VM, Das Sarma S. A self-consistent theory for graphene transport. Proc Natl Acad Sci U S A 2007;104:18392–7. doi:10.1073/pnas.0704772104.

[49] Li Q, Hwang EH, Das Sarma S. Disorder-induced temperature-dependent transport in graphene: Puddles, impurities, activation, and diffusion. Phys Rev B 2011;84:115442. doi:10.1103/PhysRevB.84.115442.

[50] Chen J-H, Jang C, Adam S, Fuhrer MS, Williams ED, Ishigami M. Charged-impurity scattering in graphene. Nat Phys 2008;4:377–81. doi:10.1038/nphys935.

[51] Yan J, Fuhrer MS. Correlated Charged Impurity Scattering in Graphene. Phys Rev Lett 2011;107:206601. doi:10.1103/PhysRevLett.107.206601.

[52] Chen JH, Jang C, Xiao S, Ishigami M, Fuhrer MS. Intrinsic and Extrinsic Performance Limits of Graphene Devices on SiO 2 n.d.

[53] Jafri SHM, Carva K, Widenkvist E, Blom T, Sanyal B, Fransson J, et al. Conductivity engineering of graphene by defect formation. J Phys D Appl Phys 2010;43:045404. doi:10.1088/0022-3727/43/4/045404.

[54] Stauber T, Peres N, Guinea F. Electronic transport in graphene: A semiclassical approach including midgap states. Phys Rev B 2007;76:205423. doi:10.1103/PhysRevB.76.205423.

[55] Wehling T, Katsnelson M, Lichtenstein a. Impurities on graphene: Midgap states and migration barriers. Phys Rev B 2009;80:1–7. doi:10.1103/PhysRevB.80.085428.

[56] Wehling T, Yuan S, Lichtenstein a., Geim a., Katsnelson M. Resonant Scattering by Realistic Impurities in Graphene. Phys Rev Lett 2010;105:3–6. doi:10.1103/PhysRevLett.105.056802.

[57] Robinson JP, Schomerus H, Oroszlány L, Fal'ko VI. Adsorbate-Limited Conductivity of Graphene. Phys Rev Lett 2008;101:196803. doi:10.1103/PhysRevLett.101.196803.

[58] Shon NH, Ando T. Quantum Transport in Two-Dimensional Graphite System. J Phys Soc Japan 1998;67:2421–9. doi:10.1143/JPSJ.67.2421.

[59] Jang C, Adam S, Chen J-H, Williams ED, Das Sarma S, Fuhrer MS. Tuning the Effective Fine Structure Constant in Graphene: Opposing Effects of Dielectric Screening on Short- and Long-Range Potential Scattering. Phys Rev Lett 2008;101:146805. doi:10.1103/PhysRevLett.101.146805.

[60] Martin J, Akerman N, Ulbricht G, Lohmann T, Smet JH, von Klitzing K, et al. Observation of electron–hole puddles in graphene using a scanning single-electron transistor. Nat Phys 2007;4:144–8. doi:10.1038/nphys781.

[61] Lee G Do, Wang CZ, Yoon E, Hwang NM, Kim DY, Ho KM. Diffusion, coalescence, and reconstruction of vacancy defects in graphene layers. Phys Rev Lett 2005;95:1–4. doi:10.1103/PhysRevLett.95.205501.

[62] Lusk MT, Carr LD. Nanoengineering defect structures on graphene. Phys Rev Lett 2008;100:1–4. doi:10.1103/PhysRevLett.100.175503.

[63] Li L, Reich S, Robertson J. Defect energies of graphite: Density-functional calculations. Phys Rev B 2005;72:184109. doi:10.1103/PhysRevB.72.184109.

[64] Ma J, Alfè D, Michaelides A, Wang E. Stone-Wales defects in graphene and other planar s p2 -bonded materials. Phys Rev B - Condens Matter Mater Phys 2009;80:1–4. doi:10.1103/PhysRevB.80.033407.

[65] El-Barbary a a, Telling RH, Ewels CP, Heggie MI, Briddon PR. Structure and energetics of the vacancy in graphite 2003:1–7. doi:10.1103/PhysRevB.68.144107.

[66] Krasheninnikov a. V., Lehtinen PO, Foster a. S, Nieminen RM. Bending the rules: Contrasting vacancy energetics and migration in graphite and carbon nanotubes. Chem Phys Lett 2006;418:132–6. doi:10.1016/j.cplett.2005.10.106.

[67] Lee Y, Kim S, Tománek D. Catalytic Growth of Single-Wall Carbon Nanotubes: An Ab Initio Study. Phys Rev Lett 1997;78:2393–6. doi:10.1103/PhysRevLett.78.2393.

[68] Krasheninnikov a. V., Nordlund K. Ion and electron irradiation-induced effects in nanostructured materials. J Appl Phys 2010;107. doi:10.1063/1.3318261.

[69] Nordlund K, Järvi TT, Meinander K, Samela J. Cluster ion-solid interactions from meV to MeV energies. Appl Phys A Mater Sci Process 2008;91:561–6. doi:10.1007/s00339-008-4514-2.

[70] Meyer JC, Eder F, Kurasch S, Skakalova V, Kotakoski J, Park HJ, et al. Accurate Measurement of Electron Beam Induced Displacement Cross Sections for Single-Layer Graphene. Phys Rev Lett 2012;108:196102. doi:10.1103/PhysRevLett.108.196102.

[71] Mølhave K, Gudnason SB, Pedersen AT, Clausen CH, Horsewell A, Bøggild P. Electron irradiation-induced destruction of carbon nanotubes in electron microscopes. Ultramicroscopy 2007;108:52–7. doi:10.1016/j.ultramic.2007.03.001.

[72] Lucchese MM, Stavale F, Ferreira EHM, Vilani C, Moutinho MVO, Capaz RB, et al. Quantifying ion-induced defects and Raman relaxation length in graphene. Carbon N Y 2010;48:1592–7. doi:10.1016/j.carbon.2009.12.057.

[73] Tapasztó L, Dobrik G, Nemes-Incze P, Vertesy G, Lambin P, Biró L. Tuning the electronic structure of graphene by ion irradiation. Phys Rev B 2008;78:233407. doi:10.1103/PhysRevB.78.233407.

[74] Flannigan DJ, Zewail AH. 4D Electron Microscopy: Principles and Applications 2012;45.

[75] Van Dyck D, Lobato I, Chen F-R, Kisielowski C. Do you believe that atoms stay in place when you observe them in HREM? Micron 2015;68:158–63. doi:10.1016/j.micron.2014.09.003.

[76] Kotakoski J, Krasheninnikov a. V., Kaiser U, Meyer JC. From Point Defects in Graphene to Two-Dimensional Amorphous Carbon. Phys Rev Lett 2011;106:105505. doi:10.1103/PhysRevLett.106.105505.

[77] Smith BW, Luzzi DE. Electron irradiation effects in single wall carbon nanotubes. J Appl Phys 2001;90:3509–15. doi:10.1063/1.1383020.

[78] Ferrari AC, Meyer JC, Scardaci V, Casiraghi C, Lazzeri M, Mauri F, et al. Raman Spectrum of Graphene and Graphene Layers. Phys Rev Lett 2006;187401:1–4. doi:10.1103/PhysRevLett.97.187401.

[79] Ferrari AC, Basko DM. Raman spectroscopy as a versatile tool for studying the properties of graphene. Nat Nanotechnol 2013;8:235–46. doi:10.1038/nnano.2013.46.

[80] Ryu S, Maultzsch J, Han MY, Kim P, Brus LE. Raman Spectroscopy of Lithographically Patterned Graphene Nanoribbons 2011;5:4123–30.

[81] Cançado LG, Jorio A, Ferreira EHM, Stavale F, Achete CA, Capaz RB, et al. Quantifying defects in graphene via Raman spectroscopy at different excitation energies. Nano Lett 2011;11:3190–6. doi:10.1021/nl201432g.

[82] Tuinstra F. Raman Spectrum of Graphite. J Chem Phys 1970;53:1126. doi:10.1063/1.1674108.

[83] Casiraghi C, Hartschuh A, Qian H, Piscanec S, Georgi C, Fasoli A, et al. Raman Spectroscopy of Graphene Edges. Nano Lett 2009;9:1433–41.

[84] Cançado LG, Takai K, Enoki T, Endo M, Kim Y a., Mizusaki H, et al. General equation for the determination of the crystallite size L[sub a] of nanographite by Raman spectroscopy. Appl Phys Lett 2006;88:163106. doi:10.1063/1.2196057.

[85] Cançado LG, Pimenta M a., Neves BR a, Dantas MSS, Jorio a. Influence of the atomic structure on the Raman spectra of graphite edges. Phys Rev Lett 2004;93:5–8. doi:10.1103/PhysRevLett.93.247401.

[86] Boukhvalov DW, Katsnelson MI. Chemical functionalization of graphene with defects. Nano Lett 2008;8:4374–9. doi:10.1021/nl802234n.

[87] Elias DC, Nair RR, Mohiuddin TMG, Morozov S V, Blake P, Halsall MP, et al. Control of graphene's properties by reversible hydrogenation: evidence for graphane. Science 2009;323:610–3. doi:10.1126/science.1167130.

[88] Bostwick A, McChesney JL, Emtsev K V., Seyller T, Horn K, Kevan SD, et al. Quasiparticle transformation during a metal-insulator transition in graphene. Phys Rev Lett 2009;103:1–4. doi:10.1103/PhysRevLett.103.056404.

[89] Bang J, Chang KJ. Localization and one-parameter scaling in hydrogenated graphene. Phys Rev B 2010;81:193412. doi:10.1103/PhysRevB.81.193412.

[90] Havu P, Ijäs M, Harju A. Hydrogenated graphene on silicon dioxide surfaces. Phys Rev B 2011;84:205423. doi:10.1103/PhysRevB.84.205423.

[91] Sofo JO, Chaudhari AS, Barber GD. Graphane: A two-dimensional hydrocarbon. Phys Rev B 2007;75:153401. doi:10.1103/PhysRevB.75.153401.

[92] Matis BR, Burgess JS, Bulat FA, Friedman AL, Houston BH, Baldwin JW. Surface Doping and Band Gap Tunability in Hydrogenated Graphene. ACS Nano 2012;6:17–22. doi:10.1021/nn2034555.

[93] Balog R, Jørgensen B, Nilsson L, Andersen M, Rienks E, Bianchi M, et al. Bandgap opening in graphene induced by patterned hydrogen adsorption. Nat Mater 2010;9:315–9. doi:10.1038/nmat2710.

[94] Ryu S, Han MY, Maultzsch J, Heinz TF, Kim P, Steigerwald ML, et al. Reversible Basal Plane Hydrogenation of Graphene. Nano Lett 2008;8:4597–602. doi:10.1021/nl802940s.

[95] Chuang C, Puddy RK, Lin H De, Lo ST, Chen TM, Smith CG, et al. Experimental evidence for Efros-Shklovskii variable range hopping in hydrogenated graphene. Solid State Commun 2012;152:905–8. doi:10.1016/j.ssc.2012.02.002.

[96] Ijäs M, Havu P, Harju A. Fracturing graphene by chlorination: A theoretical viewpoint. Phys Rev B 2012;85:035440. doi:10.1103/PhysRevB.85.035440.

[97] Wu J, Xie L, Li Y, Wang H, Ouyang Y, Guo J, et al. Controlled chlorine plasma reaction for noninvasive graphene doping. J Am Chem Soc 2011;133:19668–71. doi:10.1021/ja2091068.

[98] Cheng S-H, Zou K, Okino F, Gutierrez HR, Gupta A, Shen N, et al. Reversible fluorination of graphene: Evidence of a two-dimensional wide bandgap semiconductor. Phys Rev B 2010;81:205435. doi:10.1103/PhysRevB.81.205435.

[99] Withers F, Bointon TH, Dubois M, Russo S, Craciun MF. Nanopatterning of Fluorinated Graphene by Electron Beam Irradiation. Nano Lett 2011;11:3912–6. doi:10.1021/nl2020697.

[100] Lee WH, Suk JW, Chou H, Lee J, Hao Y, Wu Y, et al. Selective-Area Fluorination of Graphene with Fluoropolymer and Laser Irradiation. Nano Lett 2012;12:2374–8. doi:10.1021/nl300346j.

[101] Withers F, Dubois M, Savchenko AK. Electron properties of fluorinated single-layer graphene transistors. Phys Rev B 2010;82:073403. doi:10.1103/PhysRevB.82.073403.

[102] Nair RR, Ren W, Jalil R, Riaz I, Kravets VG, Britnell L, et al. Fluorographene: A Two-Dimensional Counterpart of Teflon. Small 2010;6:2877–84. doi:10.1002/smll.201001555.

[103] Boukhvalov DW, Katsnelson MI. Chemical functionalization of graphene. J Phys Condens Matter 2009;21:344205. doi:10.1088/0953-8984/21/34/344205.

[104] Sun JT, Lu YH, Chen W, Feng YP, Wee ATS. Linear tuning of charge carriers in graphene by organic molecules and charge-transfer

complexes. Phys Rev B 2010;81:155403. doi:10.1103/PhysRevB.81.155403.

[105] Joucken F, Tison Y, Lagoute J, Dumont J, Cabosart D, Zheng B, et al. Localized state and charge transfer in nitrogen-doped graphene. Phys Rev B 2012;85:161408. doi:10.1103/PhysRevB.85.161408.

[106] Zhang H, Bekyarova E, Huang J-W, Zhao Z, Bao W, Wang F, et al. Aryl Functionalization as a Route to Band Gap Engineering in Single Layer Graphene Devices. Nano Lett 2011;11:4047–51. doi:10.1021/nl200803q.

[107] Niyogi S, Bekyarova E, Itkis ME, Zhang H, Shepperd K, Hicks J, et al. Spectroscopy of covalently functionalized graphene. Nano Lett 2010;10:4061–6. doi:10.1021/nl1021128.

[108] Anwar A, Nabet B, Culp J, Castro F. Effects of electron confinement on thermionic emission current in a modulation doped heterostructure. J Appl Phys 1999;85:2663. doi:10.1063/1.369627.

[109] McCann E. Asymmetry gap in the electronic band structure of bilayer graphene. Phys Rev B 2006;74:161403. doi:10.1103/PhysRevB.74.161403.

[110] Min H, Sahu B, Banerjee SK, MacDonald AH. Ab initio theory of gate induced gaps in graphene bilayers. Phys Rev B 2007;75:155115. doi:10.1103/PhysRevB.75.155115.

[111] McCann E, Abergel DSL, Fal'ko VI. Electrons in bilayer graphene. Solid State Commun 2007;143:110–5. doi:10.1016/j.ssc.2007.03.054.

[112] Koshino M. Interlayer screening effect in graphene multilayers with A B A and A B C stacking. Phys Rev B 2010;81:125304. doi:10.1103/PhysRevB.81.125304.

[113] Miyazaki H, Odaka S, Sato T, Tanaka S, Goto H, Kanda A, et al. Inter-Layer Screening Length to Electric Field in Thin Graphite Film. Appl Phys Express 2008;1:034007. doi:10.1143/APEX.1.034007.

[114] Kim S, Nah J, Jo I, Shahrjerdi D, Colombo L. Realization of a high mobility dual-gated graphene field-effect transistor with Al2O3 dielectric Realization of a high mobility dual-gated graphene field-effect transistor with Al 2 O 3 dielectric 2013;062107. doi:10.1063/1.3077021.

[115] Lee B, Mordi G, Kim MJ, Chabal YJ, Vogel EM, Wallace RM, et al. Characteristics of high-k Al[sub 2]O[sub 3] dielectric using ozone-based atomic layer deposition for dual-gated graphene devices. Appl Phys Lett 2010;97:043107. doi:10.1063/1.3467454.

[116] Miyazaki H, Li S-L, Nakaharai S, Tsukagoshi K. Unipolar transport in bilayer graphene controlled by multiple p-n interfaces. Appl Phys Lett 2012;100:163115. doi:10.1063/1.3701592.

[117] Miyazaki H, Li S, Kanda A, Tsukagoshi K. Resistance modulation of multilayer graphene controlled by the gate electric field. Semicond Sci Technol 2010;25:034008. doi:10.1088/0268-1242/25/3/034008.

[118] Molitor F, Jacobsen A, Stampfer C, Güttinger J, Ihn T, Ensslin K. Transport gap in side-gated graphene constrictions. Phys Rev B 2009;79. doi:10.1103/PhysRevB.79.075426.

[119] Güttinger J, Stampfer C, Hellmüller S, Molitor F, Ihn T, Ensslin K. Charge detection in graphene quantum dots. Appl Phys Lett 2008;93:212102. doi:10.1063/1.3036419.

[120] Postek MT, Vladar AE, Kramar J, Stern L a., Notte J, McVey S. Helium ion microscopy: A new technique for semiconductor metrology and nanotechnology. AIP Conf Proc 2007;931:161–7. doi:10.1063/1.2799363.

[121] Müller EW, Bahadur K. Field ionization of gases at a metal surface and the resolution of the field Ion microscope. Phys Rev 1956;102:624–31. doi:10.1103/PhysRev.102.624.

[122] Morgan J, Notte J, Hill R, Ward B. An Introduction to the Helium Ion Microscope. Micros Today 2006;14:24. doi:10.1063/1.2799423.

[123] Han MY, Özyilmaz B, Zhang Y, Kim P. Energy Band-Gap Engineering of Graphene Nanoribbons. Phys Rev Lett 2007;98:206805. doi:10.1103/PhysRevLett.98.206805.

[124] DiVincenzo DP. The Physical Implementation of Quantum Computation. Fortschritte Der Phys 2000;48:771–83. doi:10.1002/1521-3978(200009)48:9/11<771::AID-PROP771>3.0.CO;2-E.

[125] Petta JR, Johnson a C, Taylor JM, Laird E a, Yacoby a, Lukin MD, et al. Coherent manipulation of coupled electron spins in semiconductor

quantum dots. Science 2005;309:2180–4. doi:10.1126/science.1116955.

[126] Koppens FHL, Buizert C, Tielrooij KJ, Vink IT, Nowack KC, Meunier T, et al. Driven coherent oscillations of a single electron spin in a quantum dot. Nature 2006;442:766–71. doi:10.1038/nature05065.

[127] Simmons CB, Prance JR, Van Bael BJ, Koh TS, Shi Z, Savage DE, et al. Tunable Spin Loading and T_{1} of a Silicon Spin Qubit Measured by Single-Shot Readout. Phys Rev Lett 2011;106:156804. doi:10.1103/PhysRevLett.106.156804.

[128] Huertas-Hernando D, Guinea F, Brataas A. Spin-orbit coupling in curved graphene, fullerenes, nanotubes, and nanotube caps. Phys Rev B 2006;74. doi:10.1103/PhysRevB.74.155426.

[129] Stampfer C, Güttinger J, Molitor F, Graf D, Ihn T, Ensslin K. Tunable Coulomb blockade in nanostructured graphene. Appl Phys Lett 2008;92:012102. doi:10.1063/1.2827188.

[130] Molitor F, Knowles H, Dröscher S, Gasser U, Choi T, Roulleau P, et al. Observation of excited states in a graphene double quantum dot. Eur Lett 2010;89:67005. doi:10.1209/0295-5075/89/67005.

[131] Güttinger J, Seif J, Stampfer C, Capelli A, Ensslin K, Ihn T. Time-resolved charge detection in graphene quantum dots. Phys Rev B 2011;83. doi:10.1103/PhysRevB.83.165445.

[132] Schnez S, Molitor F, Stampfer C, Güttinger J, Shorubalko I, Ihn T, et al. Observation of excited states in a graphene quantum dot. Appl Phys Lett 2009;94:012107. doi:10.1063/1.3064128.

[133] Liu XL, Hug D, Vandersypen LMK. Gate-defined graphene double quantum dot and excited state spectroscopy. Nano Lett 2010;10:1623–7. doi:10.1021/nl9040912.

[134] Beenakker CWJ, van Houten H. Quantum Transport in Semiconductor Nanostructures 2004;228:111. doi:10.1016/S0081-1947(08)60091-0.

[135] Wiel WG Van Der. Electron transport through double quantum dots 2003;75:1–22.

[136] Angus SJ, Ferguson AJ, Dzurak AS, Clark RG. Gate-defined quantum dots in intrinsic silicon. Nano Lett 2007;7:2051–5. doi:10.1021/nl070949k.

[137] Tilke AT, Simmel FC, Blick RH, Lorenz H, Kotthaus JP. Coulomb blockade in silicon nanostructures 2001;25:97–138.

[138] McCann E, Abergel DSL, Fal'ko VI. Electrons in bilayer graphene. Solid State Commun 2007;143:110–5. doi:10.1016/j.ssc.2007.03.054.

[139] Cai J, Ruffieux P, Jaafar R, Bieri M, Braun T, Blankenburg S, et al. Atomically precise bottom-up fabrication of graphene nanoribbons. Nature 2010;466:470–3. doi:10.1038/nature09211.

[140] Blankenburg S, Cai J, Ruffieux P, Jaafar R, Passerone D, Feng X, et al. Intraribbon heterojunction formation in ultranarrow graphene nanoribbons. ACS Nano 2012;6:2020–5. doi:10.1021/nn203129a.

[141] Picakrd D, Scipioni L. Graphene Nano-Ribbon Patterning in the ORION ® PLUS. Zeiss Appl Note 2009.

[142] Boden SA, Moktadir Z, Bagnall DMM, Mizuta H, Rutt HNN. Focused helium ion beam milling and deposition. Microelectron Eng 2011;88:2452–5. doi:10.1016/j.mee.2010.11.041.

[143] Vicarelli L, Xu Q, Zandbergen HW. Graphene Nanoribbons with atomically well-defined edges through Scanning Transmission Electron Microscopy n.d.;7:2013.

[144] Winston D, Cord BM, Ming B, Bell DC, DiNatale WF, Stern L a., et al. Scanning-helium-ion-beam lithography with hydrogen silsesquioxane resist. J Vac Sci Technol B Microelectron Nanom Struct 2009;27:2702. doi:10.1116/1.3250204.

[145] Fox D, Chen Y, Faulkner CC, Zhang H. Nano-structuring, surface and bulk modification with a focused helium ion beam. Beilstein J Nanotechnol 2012;3:579–85. doi:10.3762/bjnano.3.67.

[146] Joshi-imre A, Bauerdick S. Direct-Write Ion Beam Lithography 2014;2014.

[147] Moktadir Z, Boden S a., Ghiass a., Rutt H, Mizuta H. U-shaped bilayer graphene channel transistor with very high Ion/Ioff ratio. Electron Lett 2011;47:199. doi:10.1049/el.2010.3029.

[148] Tseng AA. Recent developments in nanofabrication using focused ion beams. Small 2005;1:924–39. doi:10.1002/smll.200500113.

[149] Custer JS, Thompson MO, Jacobson DC, Poate JM, Roorda S, Sinke WC, et al. Density of amorphous Si. Appl Phys Lett 1994;64:437. doi:10.1063/1.111121.

[150] Gui G, Li J, Zhong J. Band structure engineering of graphene by strain: First-principles calculations. Phys Rev B 2008;78:075435. doi:10.1103/PhysRevB.78.075435.

[151] Lugstein A, Basnar B, Smoliner J, Bertagnolli E. FIB processing of silicon in the nanoscale regime. Appl Phys A Mater Sci Process 2003;76:545–8. doi:10.1007/s00339-002-1890-x.

[152] Frey L, Lehrer C, Ryssel H. Nanoscale effects in focused ion beam processing. Appl Phys A Mater Sci Process 2003;76:1017–23. doi:10.1007/s00339-002-1943-1.

[153] Tseng A a. Recent developments in micromilling using focused ion beam technology. J Micromechanics Microengineering 2004;14:R15–34. doi:10.1088/0960-1317/14/4/R01.

[154] Mizuta H, Moktadir Z, Boden S a., Kalhor N, Hang S, Schmidt ME, et al. Fabrication and ab initio study of downscaled graphene nanoelectronic devices 2012;8462:846206. doi:10.1117/12.956439.

[155] Lin Y-C, Lu C-C, Yeh C-H, Jin C, Suenaga K, Chiu P-W. Graphene annealing: how clean can it be? Nano Lett 2012;12:414–9. doi:10.1021/nl203733r.

[156] Ni ZH, Wang HM, Luo ZQ, Wang YY, Yu T, Wu YH, et al. The effect of vacuum annealing on graphene. J Raman Spectrosc 2009;41:479–83. doi:10.1002/jrs.2485.

[157] Kumar K, Kim Y-S, Yang E-H. The influence of thermal annealing to remove polymeric residue on the electronic doping and morphological characteristics of graphene. Carbon N Y 2013;65:35–45. doi:10.1016/j.carbon.2013.07.088.

[158] Cheng Z, Zhou Q, Wang C, Li Q, Fang Y. Toward intrinsic graphene surfaces: a systematic study on thermal annealing and wet-chemical treatment of SiO2-supported graphene devices. Nano Lett 2011:767–71.

[159] Goossens a. M, Calado VE, Barreiro a., Watanabe K, Taniguchi T, Vandersypen LMK. Mechanical cleaning of graphene. Appl Phys Lett 2012;100:073110. doi:10.1063/1.3685504.

[160] Volk C, Fringes S, Terrés B, Dauber J, Engels S, Trellenkamp S, et al. Electronic excited states in bilayer graphene double quantum dots. Nano Lett 2011;11:3581–6. doi:10.1021/nl201295s.

[161] Dean CR, Young AF, Meric I, Lee C, Wang L, Sorgenfrei S, et al. Boron nitride substrates for high-quality graphene electronics. Nat Nanotechnol 2010;5:722–6. doi:10.1038/nnano.2010.172.

[162] Epitaxial Q, Bresnehan MS, Hollander MJ, Wetherington M, Labella M, Trumbull KA, et al. Integration of Hexagonal Boron Nitride with Quasi-freestanding Epitaxial Graphene: Toward Wafer-Scale, High-Performance Devices. ACS Nano 2012;6:5234–41. doi:10.1021/nn300996t.

[163] Goossens ASM, Driessen SCM, Baart TA, Watanabe K, Taniguchi T, Vandersypen LMK. Gate-defined confinement in bilayer graphene-hexagonal boron nitride hybrid devices. Nano Lett 2012;12:4656–60. doi:10.1021/nl301986q.

[164] Zhao S, Xue J, Wang Y, Yan S. Effect of SiO2 substrate on the irradiation-assisted manipulation of supported graphene: a molecular dynamics study. Nanotechnology 2012;23:285703. doi:10.1088/0957-4484/23/28/285703.

[165] Das A, Pisana S, Chakraborty B, Piscanec S, Saha SK, Waghmare U V, et al. Monitoring dopants by Raman scattering in an electrochemically top-gated graphene transistor. Nat Nanotechnol 2008;3:210–5. doi:10.1038/nnano.2008.67.

[166] Eckmann A, Felten A, Verzhbitskiy I, Davey R, Casiraghi C. Raman study on defective graphene: Effect of the excitation energy, type, and amount of defects. Phys Rev B 2013;88:035426. doi:10.1103/PhysRevB.88.035426.

[167] Eckmann A, Felten A, Mishchenko A, Britnell L, Krupke R, Novoselov KS, et al. Probing the Nature of Defects in Graphene by Raman Spectroscopy. Nano Lett 2012;12:3925–30. doi:10.1021/nl300901a.

[168] Cançado L, Jorio A, Pimenta M. Measuring the absolute Raman cross section of nanographites as a function of laser energy and crystallite size. Phys Rev B 2007;76:064304. doi:10.1103/PhysRevB.76.064304.

[169] Martins Ferreira EH, Moutinho MVO, Stavale F, Lucchese MM, Capaz RB, Achete CA, et al. Evolution of the Raman spectra from single-, few-, and many-layer graphene with increasing disorder. Phys Rev B 2010;82:125429. doi:10.1103/PhysRevB.82.125429.

[170] Ghislandi M, Hoffmann GG, Tkalya E, Xue L, With G De. Tip-Enhanced Raman Spectroscopy and Mapping of Graphene Sheets. Appl Spectrosc Rev 2012;47:371–81. doi:10.1080/05704928.2012.666773.

[171] Cançado LG, Hartschuh A, Novotny L. Tip-enhanced Raman spectroscopy of carbon nanotubes. J Raman Spectrosc 2009;40:1420–6. doi:10.1002/jrs.2448.

[172] Lehtinen O, Kotakoski J, Krasheninnikov A V, Keinonen J. Cutting and controlled modification of graphene with ion beams. Nanotechnology 2011;22:175306. doi:10.1088/0957-4484/22/17/175306.

[173] Ziegler JF, Ziegler MD, Biersack JP. SRIM – The stopping and range of ions in matter (2010). Nucl Instruments Methods Phys Res Sect B Beam Interact with Mater Atoms 2010;268:1818–23. doi:10.1016/j.nimb.2010.02.091.

[174] Nguyen TC, Otani M, Okada S. Semiconducting Electronic Property of Graphene Adsorbed on (0001) Surfaces of SiO2. Phys Rev Lett 2011;106:106801. doi:10.1103/PhysRevLett.106.106801.

[175] Adam S, Das Sarma S. Boltzmann transport and residual conductivity in bilayer graphene. Phys Rev B 2008;77. doi:10.1103/PhysRevB.77.115436.

[176] Xiao S, Chen J-H, Adam S, Williams E, Fuhrer M. Charged impurity scattering in bilayer graphene. Phys Rev B 2010;82:2–5. doi:10.1103/PhysRevB.82.041406.

[177] Yuan S, De Raedt H, Katsnelson M. Electronic transport in disordered bilayer and trilayer graphene. Phys Rev B 2010;82:1–13. doi:10.1103/PhysRevB.82.235409.

[178] Wang L, Meric I, Huang PY, Gao Q, Gao Y, Tran H, et al. One-dimensional electrical contact to a two-dimensional material. Science 2013;342:614–7. doi:10.1126/science.1244358.

[179] Moktadir Z, Hang S, Reynolds J, Higashimine K, Mizuta H. Metal-Insulating transition in disordered graphene nanoribbons controlled by helium ion irradiation n.d.:3–4.

[180] Gómez-Navarro C, de Pablo PJ, Gómez-Herrero J, Biel B, Garcia-Vidal FJ, Rubio a, et al. Tuning the conductance of single-walled carbon nanotubes by ion irradiation in the Anderson localization regime. Nat Mater 2005;4:534–9. doi:10.1038/nmat1414.

[181] Evaldsson M, Zozoulenko I, Xu H, Heinzel T. Edge-disorder-induced Anderson localization and conduction gap in graphene nanoribbons. Phys Rev B 2008;78:161407. doi:10.1103/PhysRevB.78.161407.

[182] Huard B, Stander N, Sulpizio J, Goldhaber-Gordon D. Evidence of the role of contacts on the observed electron-hole asymmetry in graphene. Phys Rev B 2008;78. doi:10.1103/PhysRevB.78.121402.

[183] Moktadir Z, Hang S, Mizuta H. Defect-induced Fermi level pinning and suppression of ambipolar behaviour in graphene. Carbon N Y 2015. doi:10.1016/j.carbon.2015.05.049.

[184] Jackson S. Determining hybridization differences for amorphous carbon from the XPS C 1s envelope. Appl Surf Sci 1995;90:195–203. doi:10.1016/0169-4332(95)00079-8.

[185] Susi T, Kaukonen M, Havu P, Ljungberg MP, Ayala P, Kauppinen EI. Core level binding energies of functionalized and defective graphene. Beilstein J Nanotechnol 2014;5:121–32. doi:10.3762/bjnano.5.12.

[186] Kouwenhoven LP, Markus C, McEuen PL, Tarucha S, Westervelt RM, Wingreen NS. Electron transport in quantum dots. NATO ASI Ser E Appl Sci Study Inst 1997;345:105–214.

[187] Elzerman JM, Hanson R, Willems Van Beveren LH, Witkamp B, Vandersypen LMK, Kouwenhoven LP, et al. Single-shot read-out of an individual electron spin in a quantum dot. Nature 2004;430:431–5. doi:10.1038/nature02747.1.

[188] Ihn T, Güttinger J, Molitor F, Schnez S, Schurtenberger E, Jacobsen a., et al. Graphene single-electron transistors. Mater Today 2010;13:44–50. doi:10.1016/S1369-7021(10)70033-X.

[189] Sun J, Iwasaki T, Muruganathan M, Mizuta H. Lateral plasma etching enhanced on/off ratio in graphene nanoribbon field-effect transistor. Appl Phys Lett 2015;106:033509. doi:10.1063/1.4906609.

[190] Moser J, Bachtold A. Fabrication of large addition energy quantum dots in graphene. Appl Phys Lett 2009;95:173506. doi:10.1063/1.3243690.

[191] Mott N. The mobility edge since 1967. J Phys C Solid State Phys 2000;20:3075–102. doi:10.1088/0022-3719/20/21/008.

[192] Nang TT, Okuda M, Matsushita T, Yokota S, Suzuki A. Electrical and Optical Properties of Ge x Se 1- x Amorphous Thin Films. Jpn J Appl Phys 1976;15:849–53. doi:10.1143/JJAP.15.849.

[193] Miyazaki H, Tsukagoshi K, Kanda A, Otani M, Okada S. Influence of disorder on conductance in bilayer graphene under perpendicular electric field. Nano Lett 2010;10:3888–92. doi:10.1021/nl1015365.

[194] Eda G, Mattevi C, Yamaguchi H, Kim H, Chhowalla M. Insulator to semimetal transition in graphene oxide. J Phys Chem C 2009;113:15768–71. doi:10.1021/jp9051402.

[195] Mott NF. Conduction in glasses containing transition metal ions. J Non Cryst Solids 1968;1:1–17. doi:10.1016/0022-3093(68)90002-1.

[196] Joung D, Khondaker SI. Efros-Shklovskii variable-range hopping in reduced graphene oxide sheets of varying carbon sp2 fraction. Phys Rev B - Condens Matter Mater Phys 2012;86:1–8. doi:10.1103/PhysRevB.86.235423.

[197] Cheah CY, Gómez-Navarro C, Jaurigue LC, Kaiser a B. Conductance of partially disordered graphene: crossover from temperature-dependent to field-dependent variable-range hopping. J Phys Condens Matter 2013;25:465303. doi:10.1088/0953-8984/25/46/465303.

[198] Lo S-T, Chuang C, Puddy RK, Chen T-M, Smith CG, Liang C-T. Non-ohmic behavior of carrier transport in highly disordered graphene. Nanotechnology 2013;24:165201. doi:10.1088/0957-4484/24/16/165201.

[199] Oostinga JB, Heersche HB, Liu X, Morpurgo AF, Vandersypen LMK. Gate-induced insulating state in bilayer graphene devices. Nat Mater 2008;7:151–7. doi:10.1038/nmat2082.

[200] Martins SE, Withers F, Dubois M, Craciun MF, Russo S. Tuning the transport gap of functionalized graphene via electron beam irradiation. New J Phys 2013;15:033024. doi:10.1088/1367-2630/15/3/033024.

[201] Efros a L, Shklovskii BI. Coulomb gap and low temperature conductivity of disordered systems. J Phys C Solid State Phys 2001;8:L49–51. doi:10.1088/0022-3719/8/4/003.

[202] Lemme M, Echtermeyer T. A graphene field-effect device. Electron Device Lett … 2007;28:282–4.

[203] Zhang Y, Dai O, Levy M, Sarachik MP. Probing the Coulomb Gap in Insulating n-Type CdSe. Phys Rev Lett 1990;64:2687–90. doi:10.1103/PhysRevLett.64.2687.

[204] Cheah CY. Electronic Conduction in Disordered Carbon Materials by 2015.

[205] Morozov S, Novoselov K, Katsnelson M, Schedin F, Elias D, Jaszczak J, et al. Giant Intrinsic Carrier Mobilities in Graphene and Its Bilayer. Phys Rev Lett 2008;100:016602. doi:10.1103/PhysRevLett.100.016602.

[206] Geim AK, Novoselov KS. The rise of graphene. Nat Mater 2007;6:183–91. doi:10.1038/nmat1849.

[207] Bonaccorso F, Sun Z, Hasan T, Ferrari AC. Graphene photonics and optoelectronics. Nat Photonics 2010;4:611–22. doi:10.1038/nphoton.2010.186.